CAMBERED AND NON-FLAT POLYETHYLENE WEBS INDUCED BY THICKNESS VARIATION

By

JO-ONG EDMOND POH

Bachelor of Science in Aerospace Engineering

Oklahoma State University

Stillwater, Oklahoma

2001

Submitted to the Faculty of the
Graduate College of the
Oklahoma State University
in partial fulfillment of
the requirements for
the Degree of
MASTER OF SCIENCE
May, 2007

CAMBERED AND NON-FLAT POLYETHYLENE

WEBS INDUCED BY THICKNESS VARIATION

Thesis Approved:

Dr. Hongbing Lu
Thesis Adviser

Dr. J. Keith Good

Dr. C. Eric Price

Dr. A. Gordon Emslie
Dean of the Graduate College

To Ah Kong, Ah Mah and Ah Jeng,
you will always be in my thoughts….

ACKNOWLEDGEMENTS

In our lifetime, rarely we will encounter significant people who are willing to go the distance with us; to assist, to nurture life's hard-earned lessons and most importantly to guide us through uncharted waters till we reached safe harbor. The important roles these people play, to whom we are always grateful.

First and foremost, I will like to extend my deepest gratitude to my mentor, advisor and thesis chair, Dr. Hongbing Lu, for his insightful guidance, encouraging confidence and immeasurable kindness. To whom which without generous financial assistance, this thesis will never materialize. As well, my heartfelt appreciation goes to my other committee members Dr. J. Keith Good and Dr. Eric Price; for the encouragement, experimental equipments and invaluable trust. I will also like to take the opportunity to thank two most esteem authority in the field of web handling: Prof. Bruce Feiertag; for taking me into his wing as an apprentice and teaching me everything there is to know about web handling, and Prof. John Shelton; for helpful suggestions and valuable discussion, especially when I was stuck.

This research work will not be possible without the support grant (No. 0200-3) from the National Science Foundation University/Industry Cooperative Research Center known as Web Handling Research Center at Oklahoma State

University (OSU). In addition, special thanks to the following people: Mr. Ron Markum, Dr. Joe Beisel and Dr. Balaji Kandadai; for web handling technical assistance, Mr. Ron Swanson from 3M Corporation; for discussion on creating baggy webs and interest in this work, Mr. Mike Davis and Dr. Ashish Sukhadia from Chevron Phillips Chemical Co. LLC; for arranging a private tour of the plastic blown film facility thus improving my understanding on polymeric web extrusion process, Mr. Jerry Dale at OSU; for machining and tooling assistance, and also guidance in practical ways of solving problems, Dr. Jean-Yves Bouguet; for providing the code and assistance on his camera calibration toolbox, Mr. Muthazhagu Palanisamy; for collaboration on digital image acquisition research work, Ms. Haowen Yu; for collaboration in web handling research work, Dr. Jin Ma, Mr. Gitogo Churu and my other colleagues from Polymer Mechanics Laboratory at OSU; for assistance and comments in my research.

To my parents; Mr. & Mrs. S. L. Poh, in-laws; Mr. & Mrs. W. H. Leong, families and friends back home, for their undying patience and indefatigable morale support during the pursuit of my studies. My loving and caring wife, W. F., for precious suggestions, her love, tolerance and encouragement at times of difficulty.

Finally, I dedicate this to my late grandpa; Mr. Poh Hooi Hong, my late granny; Madam Ang Gaik Gnoh and my late little brother; Kok Jeng, I'm truly sorry for not being there in your most desperate time of need. This burden and guilt in fact, I will always carry it in my heart forever.

TABLE OF CONTENTS

Chapter **Page**

LIST OF TABLES

LIST OF FIGURES

CHAPTER 1

INTRODUCTION

A *web* is a continuous thin strip of flexible material. Examples of webs, displayed in Figure 1.1, include plastic films (i.e. polyethylene and polyester), thin metallic sheets (i.e. aluminum and steel) and paper. Winding of a web, refers to the process of winding a web into a spiral form such as depicted in Figure 1.1 onto either a paper, plastic or metal core. The wound roll allows the ease in storage and shipping, while the core provides geometrical and structural support to the web.

Figure 1.1 : Examples of web wound into rolls.

When the web material is needed in processes such as printing, slitting, coating, etc., the web is unwound under tension and transported through a series of rollers for the processes to be carried out. After all these conversion

processes, the final outcome will be consumer products. Examples of such products include packaging tapes, toilet roll, aluminum foil, plastic wraps and paper towel.

In general, the engineering science behind the study of web is called *Web Handling*; where knowledge such as mathematics, mechanics and material science are applied, to understand and improve material behavior, productivity, process control and finally the quality of the roll. One of the main areas of interest by researchers is web defects, whether from winding, storage or transportation. Web defects can manifest in many forms; for instance wrinkles [28,71,76], wavy edges, starring [26,43,66], v-buckling [43], camber [75] etc., but one of the most common web defects is bagginess.

There have been some qualitative and quantitative publications on web defects in general [12,17,43,44,48,50,54,64-66,71,75] and some have referred *web bagginess* as probable cause [71,75] but none of the literature primarily focuses on categorizing web bagginess itself since it is such a broad topic.

Web bagginess can be defined as a web that does not lay flat or straight and has an inherent length difference across the width of the web in the cross-machine direction. It is a form of defect that appears in almost all web materials, and its physical appearances vary from situation to situation; to such degree that different people identify the defect with different names such as baggy lanes, non-flat web, pucker etc [78]. Thus, the motivation in this work is to understand web bagginess formation. To this end, we will look at factors that influence web bagginess, the possible sources and its different patterns.

1.1 Sources of Baggy Web

There are many sources for formation of web bagginess. Web bagginess can be induced by over-stretching, extrusion process, web thickness variation, irregular heat source, poor maintenance of web handling equipments, overlooked webline layout, long-term viscoelastic effect, hydroscopic effect, thermal effect, etc. In this section, we will review these factors and categorize them aptly.

1.1.1 Mechanical Influence

Web extrusion, web transportation, webline setup and other web handling processes can be categorized under mechanical influence on the formation of web bagginess induced by gauge variations across the width.

Examples of such influences include; uncontrolled polymeric stretching during extrusion (as demonstrated in Figure 1.2), defects and dirt on the extrusion dye [68], web dragging along the rollers with high coefficient of friction (i.e. nip and aggressively wrapped idle rollers) [68,75], winding at material yielding tension [68,75], air entrapment during winding, excessive application of coating on baggy areas [75], printing [75], laminating [75], slitting (i.e. dull blades or poor blade alignment) [68,75], misalignment of the rollers (as depicted in Figure 1.3) [75], imperfection in dye nip [70], poor maintenance [68], design oversight [75] and lapses during manufacturing of production components [68,75].

Shelton summarized these mechanical influences perfectly by stating, any process that control the mass per unit area across the web without control over

the actual web thickness, or processes which are nonuniform across the web with the intention to attain uniform thickness profile (i.e. crowned rollers), may generate web bagginess and should be flagged a suspect [75]. In addition, Shelton noted specifically in the case of cambered web that camber may be generated in a zone of high tension and high nonuniform temperature zone across the web such that yielding fluctuates across the web [75].

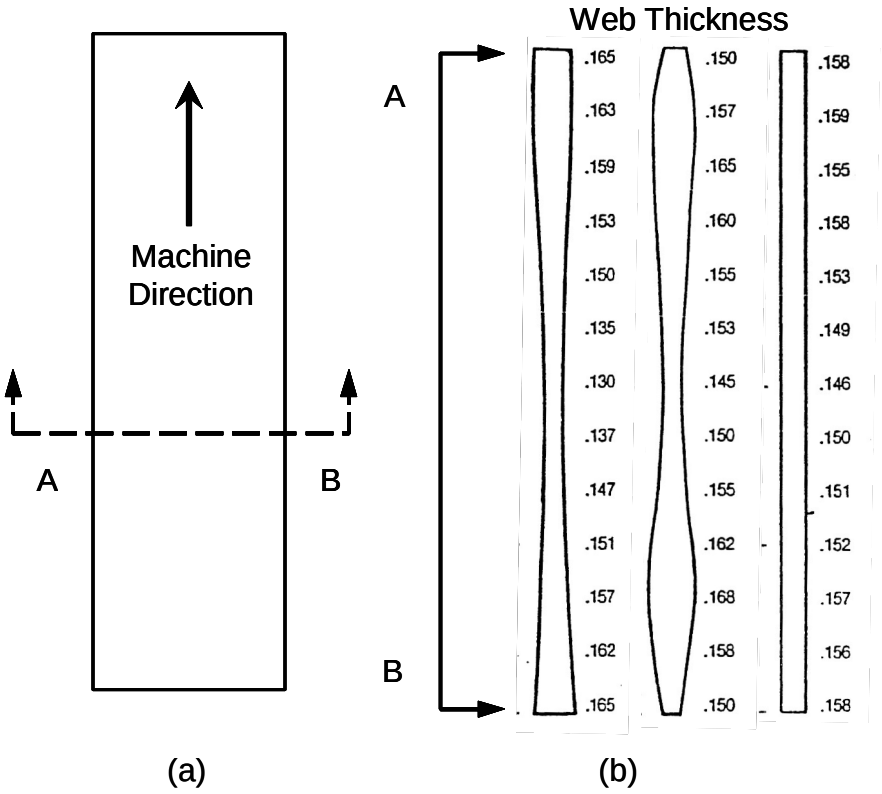

Figure 1.2 : Examples of gauge variations in a web: (a) A web with AB indicating the cross-section, (b) 3 different gauge variation examples of web cross-section [68]. The numbers at the side of each example indicates the web thickness.

Therefore, in terms of mechanical influence, it can be summarized that lapses on a small scale, do not reveal itself as a source for web bagginess at the

early stages of web handling. But when compounded, such as in winding of a large roll, the source becomes obvious leading to formation of baggy webs.

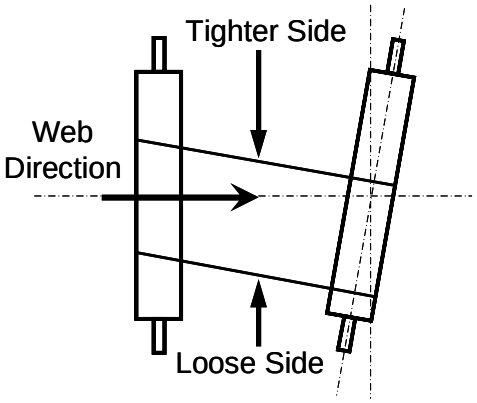

Figure 1.3 : An example of misaligned rollers.

1.1.2 Thermal Influence

Another source of web bagginess is thermal influence. Thermal influence can be categorized into three sources; for instance, web process, extrusion and environment.

During web transportation, localized heat may build-up in a web while being transported through different processes, from unwinding to winding. An example will be, a web with high coefficient of friction passing through rollers over a long period of time will generate heat on the rollers. These hot spots on the web coupled with high winding tension will generate localized stretching on the web across the width, thus forming baggy web.

Flow of heated air rising from the front end of the extruder against the web may also cause gauge variations on the web, thus leading to the formation of baggy web.

Environmental temperature within the facility will also affect the formation of web bagginess. On a hot day with temperature sensitive materials running at the facility or flow of air (hot or cold) within the facility can cause undesired localize heating or cooling of webs. As a result, baggy webs could form.

1.1.3 Hydroscopic Influence

Another source of web bagginess that has hardly been addressed in the literature is hydroscopic influence. In summary, hydroscopic effect can be instigated by either web process or environment. For example, web material such as paper may absorb excessive moisture during web processes such as coating and printing. In addition, high humidity environment may also influence the formation of web bagginess on paper.

1.1.4 Summary of Influences

The sources of baggy webs and the formation of web bagginess is summarized in Figure 1.4. The web material taken into consideration when constructing Figure 1.4, are paper and polymeric (i.e. polyethylene, polyester and polypropylene) webs. It should be recognized, however, that Figure 1.4 is incomplete since the subject of web bagginess is so extensive that there are still unknown sources.

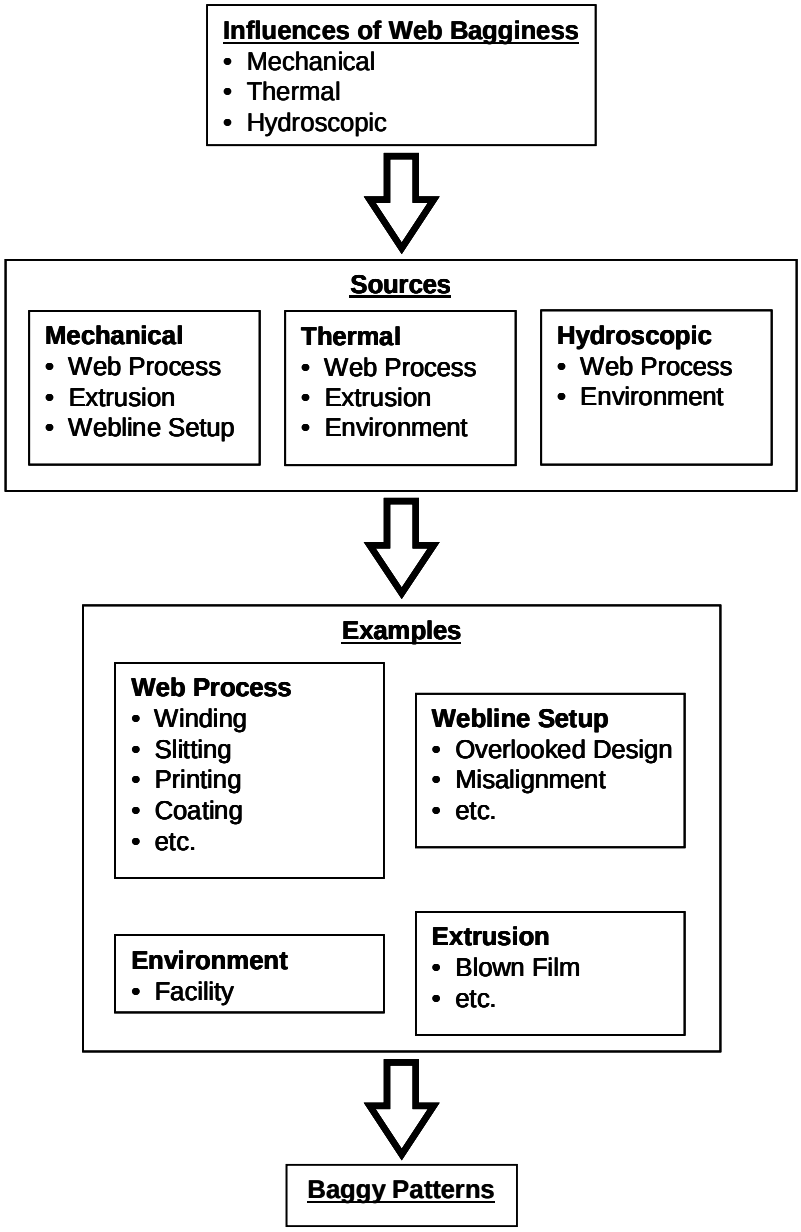

Figure 1.4 : Categorized guide on web bagginess formation.

Figure 1.5 embodies the continuation of Figure 1.4 and contains the commonly known web bagginess patterns such as camber, baggy edges, baggy center, baggy lane and localized baggy patches. For each case of web

bagginess, illustrations and example images are included for visualization and reference.

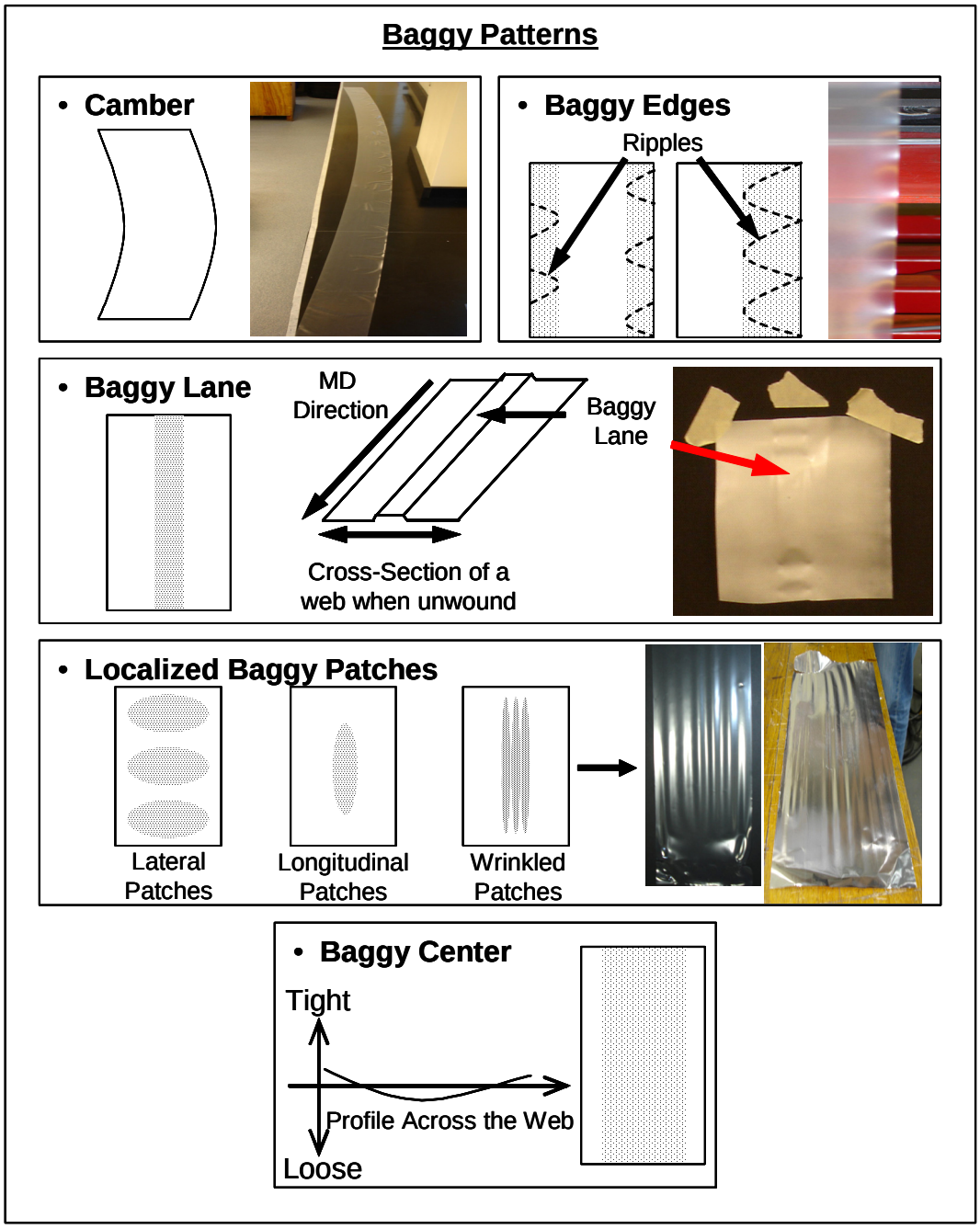

Figure 1.5 : Web bagginess patterns where the shaded area represents the baggy region.

1.2 Problems Caused by Baggy Web

In this section, the problems caused by web bagginess defects will be addressed. Other than an increase in total cost, due to material waste and cosmetic reasons [70]; web bagginess poses serious problems to a production line.

For the case of camber web, Shelton explained that the triangular or trapezoidal tension distribution of uniformly cambered web will cause the rollers to be insufficiently constrained while maintaining parallelism with other adjacent rollers, thus steering the web towards the tighter side [75] as depicted in Figure 1.6. Since web span tends to align perpendicular to the rollers before coming in contact, hence the baggy side will begin to form diagonal wrinkles as a result. Also on spreaders, where the bowed or concaved rollers rely on web tension for grip; spreaders will in fact create wrinkles instead of eliminating them as was originally designed to function, by steering the cambered web towards the tighter side [75].

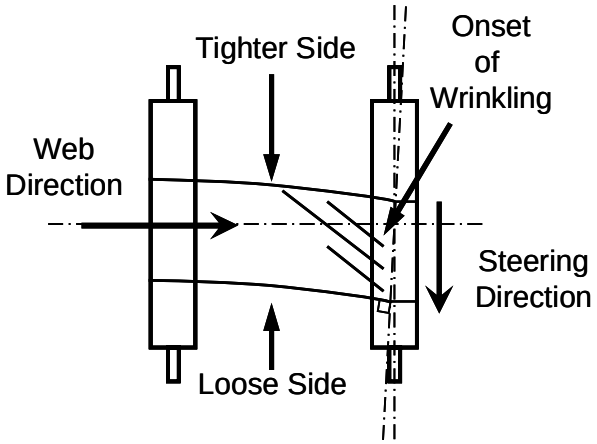

Figure 1.6 : A cambered web steers towards the loose side with onset of wrinkling.

At high tension, if the degree of camber on a cambered web is not severe, instead of forming wrinkles as the web feeds onto the roll, the wound roll will have a tapered roll characteristic instead. In fact, a tapered roll can easily be determined by measuring the circumference of the roll from end to end.

For processes that require the web to be nipped, such as printing, coating or laminating, baggy webs could have difficulty going through these processes since baggy webs do not lay flat [75]. In printing, web will not lie flat for the printing cylinder, resulting in either a wrinkle or misprint as demonstrated in Figure 1.7. Also, baggy webs do not coat very well in a coating process due to the same reason. Similarly, a baggy web cannot bond flat with another web in lamination, creating voids and wrinkles.

In some processes, baggy webs tend to float over rollers instead of wrapping on the roller, making the process difficult such as corona treatment. This will generate problems in web guiding, tracking and web-path control [70].

Furthermore, baggy webs can lead to air or fluid entrainment issues, especially in a printing process since it depends on local tension. The reason is the inability for the baggy web to transfer heat back and forth between rollers and other processes that require uniform entrainment of fluid [75]. On the contrary, baggy webs will cause air entrapment when winding onto a roll without a rider roller, thus propagating the bagginess onto subsequent layers making the problem worse.

It may be noted that it is difficult to detect and quantify baggy web without physical visualization (human eye) [70]. In fact, results from common measuring

devices do not correlate well with web bagginess due to its diverse manifestations and most direct measurement method of web bagginess are either tedious or laden with uncertainties.

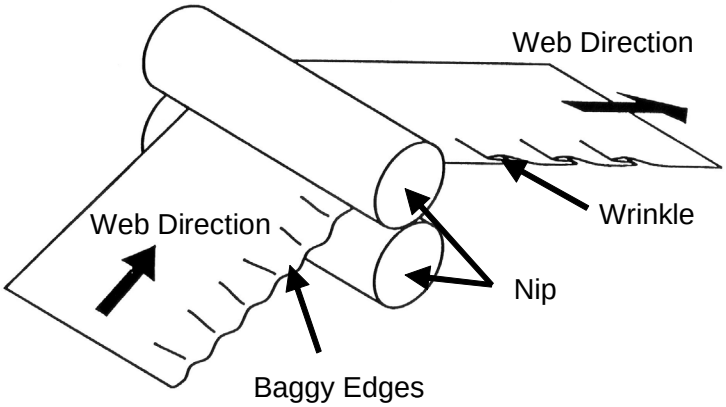

Figure 1.7 : An example of a baggy web going through a pair of nips [17]. Notice the wrinkles on the web when exiting the nips, where the nips fold the baggy edges as the baggy web enters the nips.

1.3 Scope of Study and Outline

The purpose of this study is to focus on the viscoelastic effect of the bagginess defect in web handling, especially on post-winding a wound roll. The web material selected for this study is polyethylene since viscoelastic effects for this material is significant at room temperature, and it is also easier to detect, observe, measure and analyze baggy lanes at these conditions. To accomplish the task, there are several main objectives that will need to be met:

(1) To determine how baggy webs are formed.

(2) To find the viscoelastic behavior of the web for purpose of modeling.

(3) To investigate the possibility of using digital image analysis to determine the surface profile of a baggy web.

To accomplish objective (1), the first step is to measure the fundamental mechanical properties of polyethylene web. The measured results are presented in Chapter 2. The second step is to create, measure, observe and analyze several cases of web bagginess. The results will be given in Chapter 3. Then, objective (2) can be reached by looking at both in-plane and out-of-plane long-term viscoelastic material properties of wound polyethylene roll in Chapter 4.

For objective (3), a method to detect certain web bagginess using digital image analysis will be explored. A Camera Calibration Toolbox in MatLab and WinDIC software will be used for this purpose. The results will be discussed in Chapter 5.

The expected contribution in this study will enable the verification of a viscoelastic winding model that is currently under development at the Web Handling Research Center. This model should be able to predict long-term viscoelastic characteristics of wound roll stress distribution, for a wide range of winding and storage conditions. Furthermore, the model will also be able to predict and examine web bagginess; especially baggy lanes, using the results from this study. It is hoped that the final outcome will improve the understanding of web bagginess; since presently no quantitative work has been conducted on web bagginess.

CHAPTER 2

MATERIAL SELECTION

Polyethylene web of 0.0025 inch thick, the same material used by Qualls [69], will be the primary material used for this study (Chapter 2 and 4). It should be noted that these polyethylene rolls had been stored in the storage area for 12 years. Therefore, due to aging effect, crystalline phase might have been developed due to pressure and the material properties may have changed.

Furthermore, polyethylene has a glass transition temperature, T_g, between -90^{o}C to -125^{o}C, and a melt temperature, T_m, between 105^{o}C to 130^{o}C, depending on its density. Therefore, its viscoelastic effect (recovery rate) could occur rapidly at room temperature (22^{o}C) at which winding will be conducted.

2.1 Measurements of Web Thickness and Young's Modulus

Before conducting any web handling study, two key parameters that should be known are web thickness and *Young's Modulus*. The first sub-section will cover the measurement of thickness variations on the web and the results will be compared to data provided by the manufacturer. The second sub-section will address the *Young's Modulus* in the machine direction for the polyethylene web. The results of this measurement will be used throughout this study.

2.1.1 Web Thickness Measurement

Polyethylene webs are commonly produced through an extrusion process followed by biaxial stretching or blow molding process associated with extensive stretching. It is this stretching process that converts the webs to a specified thickness. Unfortunately, often the stretching process is not consistent throughout the entire surface of the web, thus there is some variation in the thickness of the web.

Three sections of polyethylene web were taken from available wound rolls at random locations to verify the manufacturer's thickness specification. A line was drawn across the machine direction for each web section and reference points with 0.5 inch spacing, were marked using a marker pen. To perform the thickness measurement, a pneumatic powered *Schaevitz PPA-050 Precision Gage Head* connected to a *Schaevitz DTR-451 Digital Transducer Readout* was utilized and Figure 2.1 shows the device used in the experiment.

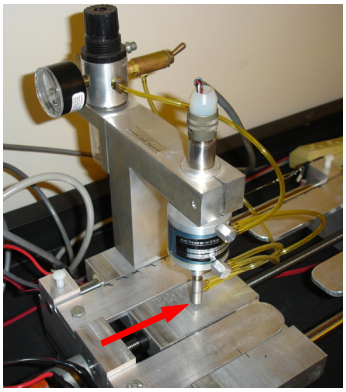

Figure 2.1 : The pneumatic device used to measure web thickness. Note the arrow pointing to the location where the samples were placed for measurement.

Prior to any actual measurement, calibration on the device was conducted using a thin aluminum plate of known thickness. The thickness of the plate was confirmed with a micrometer and the error was 0.2%; thus the device shows high accuracy. Then, the prepared web sections were placed under the gage head and measurements were taken for each reference point across the machine direction of the web. Data collected from all three readings are plotted in Figure 2.2.

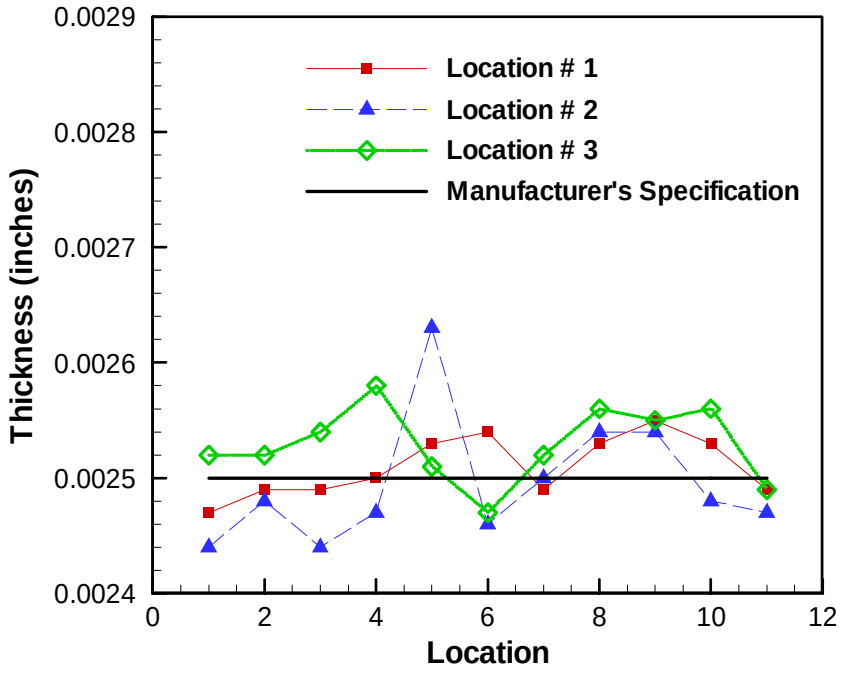

Figure 2.2 : Measured web thickness at same location for each web section.

Experimental results from Figure 2.2 show the actual thickness variations across the polyethylene web in the machine direction. The calculated average thickness for all three sections was approximately 0.0025±0.00002 inches; thus the polyethylene web thickness is quoted as 0.0025 inches for all future experiments and modeling.

2.1.2 Tangential Modulus of Elasticity

There are several ways to measure the tangential modulus of elasticity of the web in the machine direction. One way is to use a material testing machine but this method can only use short samples, thus does not necessarily characterize the tangential modulus of the entire wound roll. Another approach is to apply tension to a long strip of web, which allows better characterization of the tangential modulus of the entire wound roll. The latter method was used.

Three sections of 0.0025 inch thick polyethylene web; each at least 54 feet long, were slit at random locations of the wound rolls. In each experiment, a section was laid flat on a long smooth surface; in this case, the corridor of the web handling laboratory. At one end of the sample, the edge was taped down to the floor with *Scotch Storage Tape*. Then cubic steel weights were placed on the same edge to hold the web down.

At the other end, an aluminum plate of approximately 7 × 3/4 × 3/16 inches (length × width × height) was attached perpendicular to the web. This plate ensures that an evenly distributed force will be applied onto the web and a hand-held digital force gauge was hooked onto the plate to measure force.

Before placing this end back onto the floor, the web was aligned as straight as possible; as demonstrated in Figure 2.3(a), without applying excessive tension. Also, a piece of paper was taped onto the floor under the aluminum plate. This paper will allow the computation of strain from the marked displacement of the aluminum plate when the axial force is applied. When the web was laid flat on top of the paper untensioned, a marker was used to mark

the position of the web using the base of the aluminum plate as the initial starting point.

When the entire setup was ready, as illustrated in Figure 2.3(b), an incremental tension of 1 lb was applied onto the sample by sliding the force gauge on the floor. Each time the tension was applied, the position of the aluminum plate was marked. Once the applied force reaches 10 lbs, the last position was marked on the paper before ending the experiment. The entire process was repeated for other samples to obtain additional measurement data.

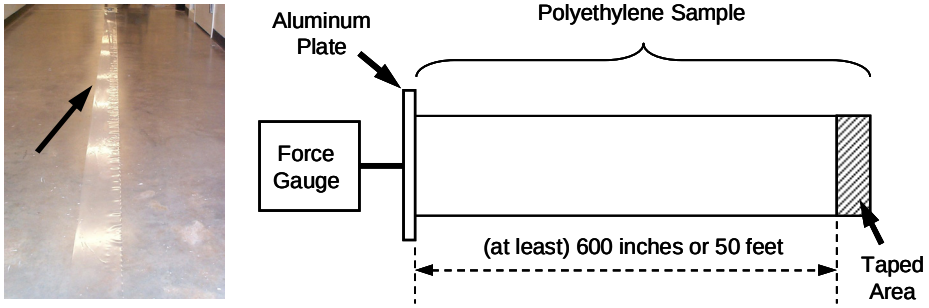

Figure 2.3 : Experimental setup used to measure the tangential modulus of elasticity for polyethylene webs. (a) Polyethylene web that was aligned straight prior to the experiment. The arrow indicates the free edge where tension was applied. (b) A schematic of the experimental setup.

The measured tangential modulus of elasticity data for each sample is displayed in Figure 2.4. The average tangential modulus of elasticity is calculated to be approximately 23 ksi. It should be noted however, that generic polyethylene webs are listed to have tangential modulus of elasticity of at least 24 ksi. Thus,

the difference between the average value and the generic value may be due to the material property changes of the wound rolls.

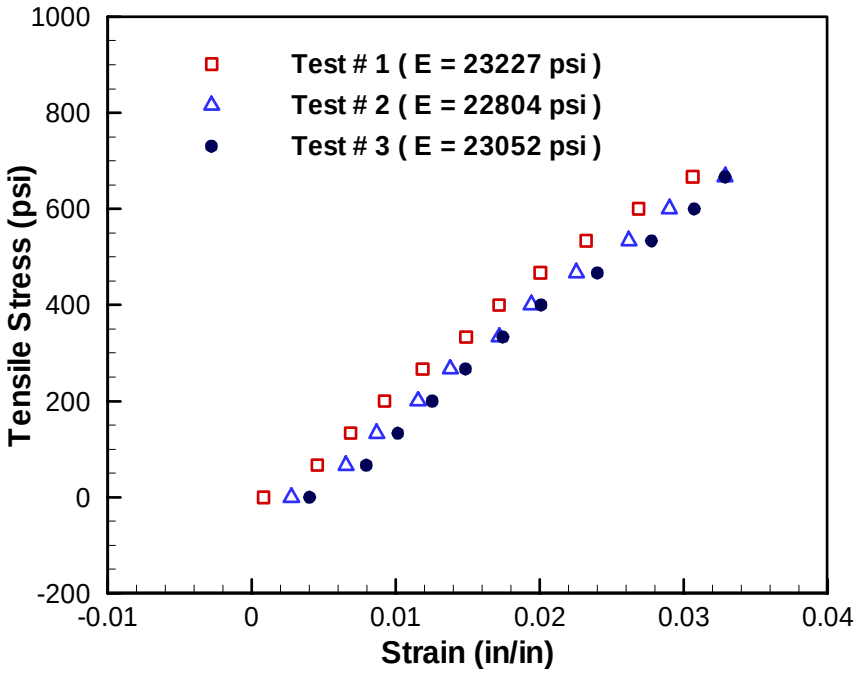

Figure 2.4 : Tangential modulus of elasticity for each sample collected from the experiment.

2.2 Pfeiffer's Coefficient

In this section, a simple compression test, or *stack test*, was conducted to determine the mechanical behavior in the radial direction. In the *stack test*, a stack of web material is compressed, and the load and displacement data are recorded. This information will be used to determine the radial modulus of the polyethylene web. In addition, such tests will determine the typical range of radial strain for polyethylene web in a wound roll. The strain range will later be used to design out-of-plane relaxation test.

2.2.1 A Brief Review on Pfeiffer's Coefficient

Pfeiffer's Coefficients [64-66] can be determined from the stress-strain curve, acquired from stack compression tests. Once these coefficients are known, a winding model based on Hakiel's work [29] can be used to establish the range of radial strains.

Authors from earlier works did realize the existence of nonlinear compressive behavior of wound rolls in the radial direction; particularly paper and plastics [1,85,86], but was largely ignored. It was Pfeiffer [64-66], who attempted to describe this behavior by proposing the following relationship,

$$P = K_1\left(\exp\left(K_2\,\varepsilon_r\right)-1\right) \tag{2.1}$$

where P and ε_r represent the radial stress and strain, respectively; K_1 and K_2 are constants. Pfeiffer identifies K_1 as an overall multiplier in terms of pressure, and K_2 as a dimensionless number, also known as *springiness factor*. In fact, later studies conducted by Hakiel [29] drew the same conclusion, when Hakiel compare his modeling results with Pfeiffer's, both results were in good agreement.

The radial modulus of elasticity, E_r for a nonlinear elastic material is defined as

$$E_r = \frac{dP}{d\varepsilon_r} \tag{2.2}$$

Applying equation (2.2) on equation (2.1) leads to

$$E_r = K_1 K_2 \exp\left(K_2\,\varepsilon_r\right) \tag{2.3}$$

Now considering equation (2.1), equation (2.3) can be rewritten as,

$$E_r = K_2 \left(P + K_1 \right) \tag{2.4}$$

which gives the radial modulus of elasticity as a function of stress. This equation will enable experimental data to be compared with Qualls' data [69].

2.2.2 Experimental Method and Measurement

Polyethylene webs of 0.0025 inch thick were used to conduct this experiment. Three stacks of 6.5 × 6 × 1 inches (length × width × height) polyethylene webs were prepared from a wound roll to determine the repeatability of the experiment.

In each experiment, a stack of polyethylene web was placed as shown in Figure 2.5; on a 6 inch diameter compression platen. Notice that the edges were extended slightly beyond the boundary of the platen. This was to avoid any edge-effect; either from imperfect stacking of webs or excessive burr edges on stack due to slitting, which will cause inaccuracies in the experimental data when the compression load is applied directly on the edge.

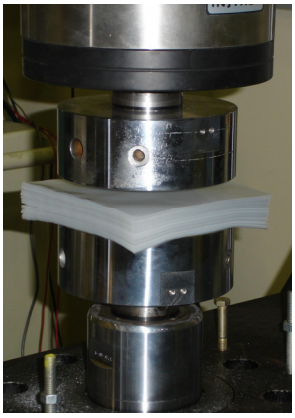

Figure 2.5 : A stack of polyethylene web placed on top of the compression platen ready to begin the experiment.

The compression platens was mounted on a hydraulic powered *Instron 8502 Material Test Frame* as shown in Figure 2.6; with a 55,000 lb load cell fastened at the top and connected to a computer for controls and data acquisition via an Instron GPIB interface (*FastTrack 8800 Desktop Controller*). Displacement control was used to apply the compression load on each polyethylene stack at a rate of 0.002 in/s until the load reached approximately 12,000 lbs; both the displacement and load data were recorded.

Figure 2.6 : A view of the entire experimental setup.

2.2.3 Results, Analysis and Discussion

The stress-strain curves are plotted in Figure 2.7. The K_1 and K_2 material constants were determined for each curve using *Microsoft Excel Solver*. The average results were found to be $K_1 = 1.631$ and $K_2 = 134.902$. These results agree with Pfeiffer's prediction [64] where he states that K_2 is within 100 – 200 for homogenous plastic films. In addition, the experimental results in terms of radial modulus, E_r versus compressive stress, P were plotted versus Qualls' results [69] in Figure 2.8; both results show good agreement.

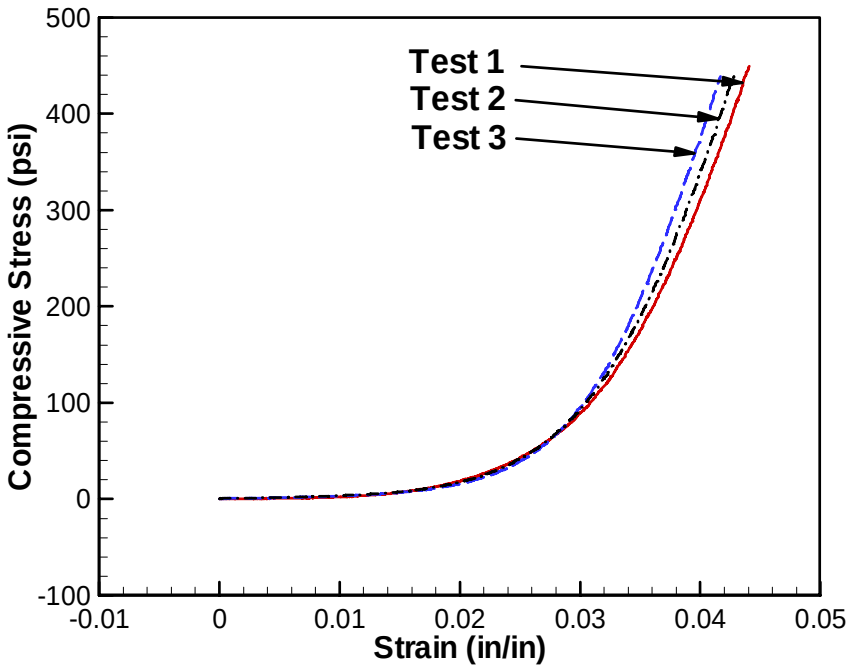

Figure 2.7 : Experimental data of the stack test plotted in terms of stress-strain curve.

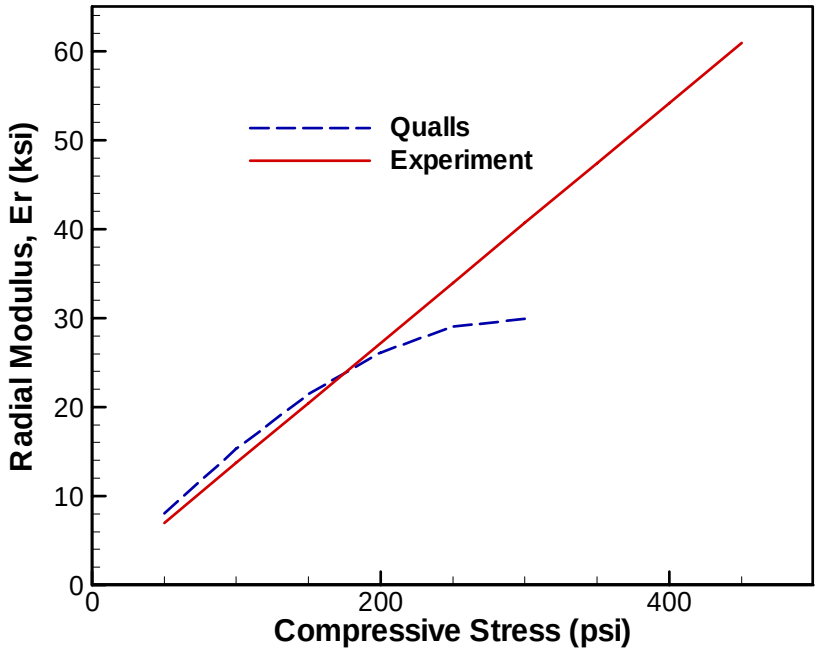

Figure 2.8 : Radial modulus, E_r versus compressive stress, P plotted versus Qualls' results [69] for comparison.

With the material constants solved, the typical range of radial strain that exist on a wound polyethylene roll can now be approximated using a proprietary numerical simulation software called *Winder 6.3* developed in the Web Handling Research Center at Oklahoma State University.

Two cases were considered, and both were simple nonlinear elastic conditioned. In Case 1, the minimal winding tension (0.5 pli or 0.5 lbs per linear inch) was used on 2.5 mil thick polyethylene roll. In Case 2, the maximum winding tension was 2 pli. The input parameters used for both cases in Winder 6.3 are listed in Table 2.1. The approximate results for both cases are plotted in Figure 2.9, thus we have determined the typical range of radial strain that exist on a polyethylene web when it is wound into a roll.

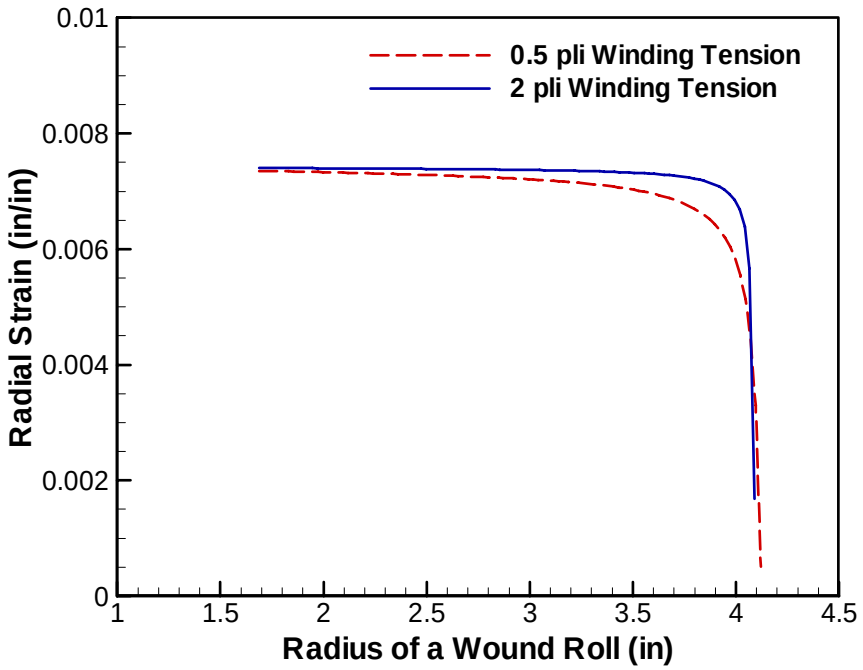

Figure 2.9 : Numerical results of radial strain typically seen on a wound polyethylene roll.

Winder 6.3	*Case 1 (Lower)*	*Case 2 (Upper)*
Input Parameters		
Model Type	Hakiels	Hakiels
Winder Type	Center	Center
Material Properties		
Caliper/Web Thickness (in)	0.0025	0.0025
Web Width (in)	6	6
Poisson's Ratio of Web, $v_{r\theta}$	0.01	0.01
v_{zr}	0	0
$v_{\theta z}$	0	0
CMD Modulus (psi)	910000	910000
Winding Parameters		
Core OD (in)	3.375	3.375
Wound Roll OD (in)	8.375	8.375
Acoustic Properties		
Core Wall Thickness (in)	0.1875	0.1875
Layers for Model Run	1000	1000
Web Failure Parameters		
Web Yield Stress (psi)	1500	1500
Web Blocking Pressure (psi)	100	100
Winding Tension		
T0	200	800
Radial Modulus		
K1	1.631	1.631
K2	134.902	134.902
MD Modulus		
MO	24000	24000
Core Stiffness		
CSO	2755060	2755060

Table 2.1 : Input parameters used in Winder 6.3 to approximate typical range of radial strain on a wound polyethylene roll.

2.3 Chapter Summary

We have measured the thickness of polyethylene web in the cross-machine direction (CMD). The average thickness was approximately 0.0025 ±0.00002 inches. The tangential modulus of elasticity was found to be 23 ksi, which is close to the nominal tangential modulus of elasticity of 24 ksi. Although, the available polyethylene rolls have been kept in storage for at least 10 years now; the radial modulus stays almost unchanged.

CHAPTER 3

MEASUREMENTS AND FORMATIONS OF WEB BAGGINESS UNDER CONTROLLED CONDITIONS

In this chapter we will investigate and generate (under controlled conditions) some of the common cases of web bagginess, which include cambered web, baggy edges and baggy lanes. We will also investigate the possibility of using *ABAQUS* to evaluate behavior of web on rollers under tension and the formation of troughs under tension.

3.1 Cambered Web

In this section, we will determine the viscoelastic recovery rate of cambered web. A measurement method similar to Shelton's [75] will be used to measure the extent of camber and the viscoelastic recovery, when the web is placed on a flat surface.

3.1.1 A Brief Review on Cambered Web

A cambered web is a web that is unable to lay in a straight line on a plane under stress free condition, thus can be considered a baggy web [75]. Due to the arc characteristic of a cambered web, Shelton [75] gave the following equation for the radius of curvature, ρ

$$\rho = \frac{L^2}{8D} \tag{3.1}$$

where L is the length of the test section of the web and D is the distance between the arc and the chord. Shelton [75] indicated that equation (3.1) is only an approximation; valid when D/L is small, under the case when the arc of a circle is approximately a parabola.

3.1.2 Formation and Measurement of Cambered Web

Equilateral-triangular web inserts of approximately 7 inches on each side were prepared for this experiment using 0.0025 inch thick polyethylene sheets. These inserts will be used to create a cambered web.

At the same time, sections of polyethylene web; approximately 200 inches long, were slit from 0.0025 inch thick wound rolls. These sections were laid flat untensioned with all creases removed on a long table as indicated in Figure 3.1 to check for signs of camber. Once the sample for a particular roll has been confirmed to be straight, additional samples were taken from the same roll at different locations.

The purpose was to make certain that the roll of polyethylene web being used for this experiment was initially straight and does not contain any traces of cambered web characteristics. When a roll that does not exhibit any camber characteristics has been thoroughly checked, the roll was then mounted on the winder shown in Figure 3.2 for experiment.

The winding parameters used during the experiment are listed in Table 3.1. A Fife web guide Model CSP-01-06 was used to control the web lateral

motion, while a pair of 100 lb load cells was employed to measure the web tension. The load cells were controlled by *Tidland Pneumatic Tension Controller Model 2500* via *Montalvo Torque Brakes Model BJ2-CD-100* mounted on the unwinding roller.

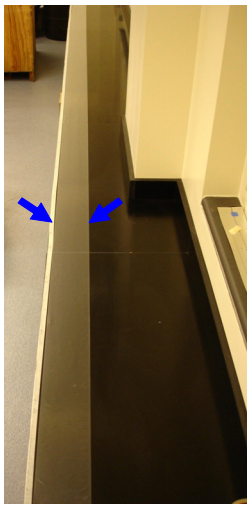

Figure 3.1 : A section of polyethylene web laid flat untensioned with all creases removed on a long table to check for signs of camber. The arrows indicate the position and alignment of the web.

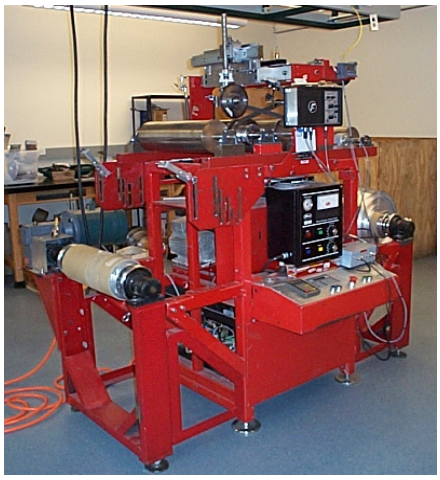

Figure 3.2 : The winder used to conduct web winding experiment.

Material	Polyethylene
Web Thickness:	2.5 mil
Web Width:	6 in
Total Wound Roll Length:	~ 72 ft 10 in
Number of Laps:	~ 110 layers
Winding Tension:	6.5 lb
Winding Speed:	4.3 ft/min
Insert Geometry:	Equilateral Triangle
Insert Period:	Every 4 Revolution
Insert Thickness (A Stack of 3 Inserts):	7.5 mil

Table 3.1 : Experimental parameters used in the study of cambered web.

While the roll was being unwound and transported to the other side, the triangular inserts were inserted into the wound roll at a periodic rate on a specific location. After winding every four layers of web on the wound roll, a stack consisting of three triangular inserts was inserted. Each triangular insert had thickness of 0.0025 inches; hence a total of 0.0075 inch gauge variation in thickness was created on the wound roll at every 4 revolutions.

This unequal web thickness (one edge is thicker than the other) forces subsequent layers to conform to the surface of the layer with inserts as the roll was being wound. Hence, each layer begins to stretch more on one side creating an uneven tension distribution. It was this stretching that causes the web to become cambered on one side when laid flat on a surface.

The roll that has been wound with equilateral-triangular inserts is revealed in Figure 3.3. Due to the predominant viscoelastic effects of polyethylene, the

changes of the web from straight web to cambered web will occur. Therefore, the roll was left on the winder at room temperature overnight after winding.

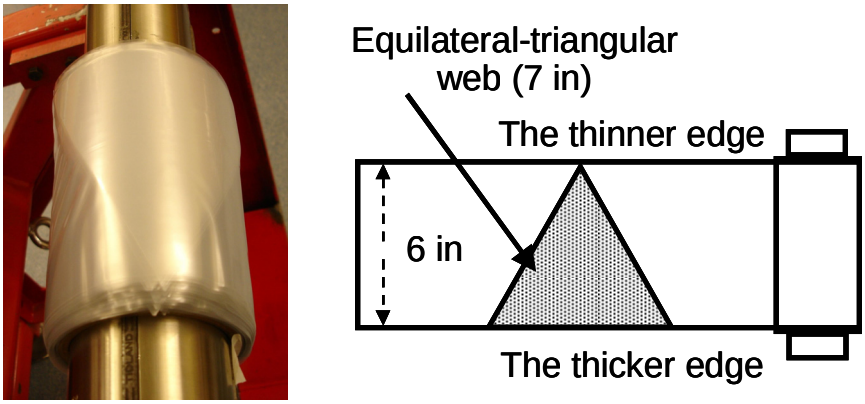

(a) (b)

Figure 3.3 : (a) The roll that has been wound with equilateral-triangular inserts; (b) An illustration of the insert with respect to the wound roll.

After 24 hours, the roll was removed from the winder and a section of the web, approximately 215 inches, was slit from the roll. The section was then laid flat untensioned with all creases removed on the long table with its arc facing the edge of the table, as shown in Figure 3.4(a), while Figure 3.4(b) gives an idea of the insert position relative to the web when the entire roll was being wound.

Two parameters defined in Figure 3.5; length of the chord, c, and the perpendicular height of the bow at pre-determined positions, D_i, were measured using a measuring tape while time and date of measurement taking place were noted. After that, the cambered web was left unattended for recovery before the measurements were repeated until the cambered web has recovered to almost a straight web.

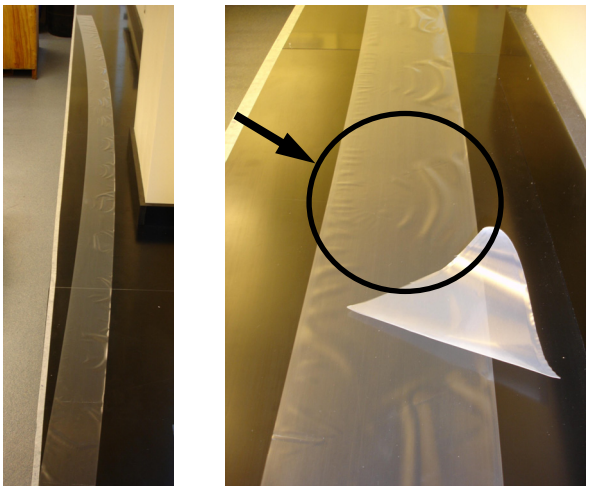

(a) (b)

Figure 3.4 : (a) A section of cambered web was removed from the wound roll and was laid flat on the long table with its arc facing the tables edge (left side) in preparation for measurement. (b) Inserts used in the experiment, placed next to the cambered web to demonstrate the positioning of the inserts in the wound roll. The circled area indicates the area of the inserts relative to the web, notice the traces of localized stretching of the web that create the bagginess.

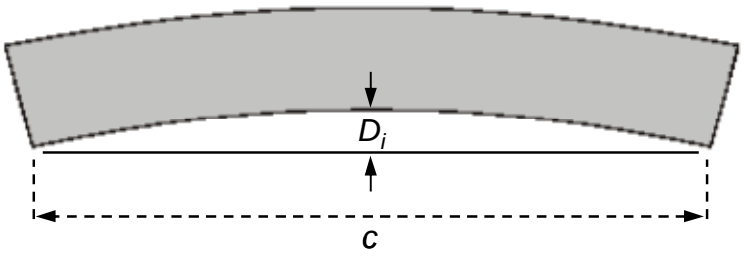

Figure 3.5 : An illustration of the two parameters used to calculate the radius of curvature for a cambered web.

3.1.3 Results and Discussion

Due to the experimental setup and method of data collection used in the experiment, Shelton's definition of a cambered web based on the radius of curvature; equation (3.1) was not used. Instead, a new equation was derived based on Shelton's idea of using the radius of curvature of an arc.

The following derivation is based on an arc of a circle, with the assumption that the arc will not be larger than a semi-circle. From Figure 3.6 consider the Pythagoras Theorem expression of

$$\rho^2 = \left(\frac{c}{2}\right)^2 + d^2 \tag{3.2}$$

Also note that $d = \rho - D$ from Figure 3.6, thus by combining both equations and rewriting it in terms of radius; we have,

$$\rho = \frac{c^2 + 4D^2}{8D} \tag{3.3}$$

where ρ corresponds to the radius of curvature of the cambered web, D is the maximum bow length of the cambered web and c is the length of the chord as shown in Figure 3.6.

Finally, the experimental results are plotted in Figure 3.7 together with the respective theoretical circular arcs. The plotted results might look like parabolas instead of circular arcs due to the scaling factor between the bow length and chord length.

The theoretical arc of the circle used in Figure 3.7 is based on the following derivation. From Figure 3.6,

$$(x-i)^2+(y+j)^2=\rho^2 \tag{3.4}$$

Rewriting equation (3.4) as a function of x and ρ, then substituting the known parameters such as $d=\rho-D$ and $c/2$; we have

$$y=\sqrt{\rho^2-\left(x-\frac{c}{2}\right)^2}-(\rho-D) \tag{3.5}$$

Equation (3.5) represents the theoretical arc equation used as comparison in Figure 3.7 with the assumption that the radius of curvature, maximum bow length and length of the chord for the cambered web are known. Then the y coordinate can be solved numerically by varying the x coordinate along the chord of the cambered web.

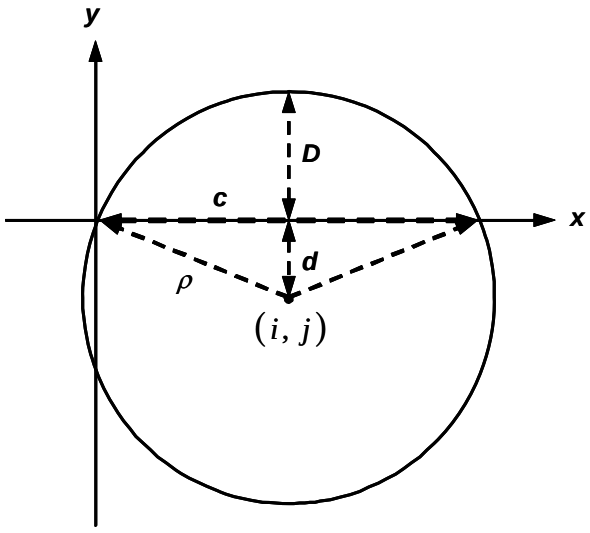

Figure 3.6 : The diagram illustrates all the variables used in the derivation of the equation for the cambered web.

In general, the error is small with maximum error of 4% and the error increases as the cambered web becomes straighter. This was due to less

precision in measurement when the bow length becomes smaller. Since the polyethylene web was left in a cambered state within the wound roll at room temperature for approximately a day before measurement starts, it is no surprise that the time frame of the collected data was less than 3 days. This can be attributed to the predominant viscoelastic effect of polyethylene web.

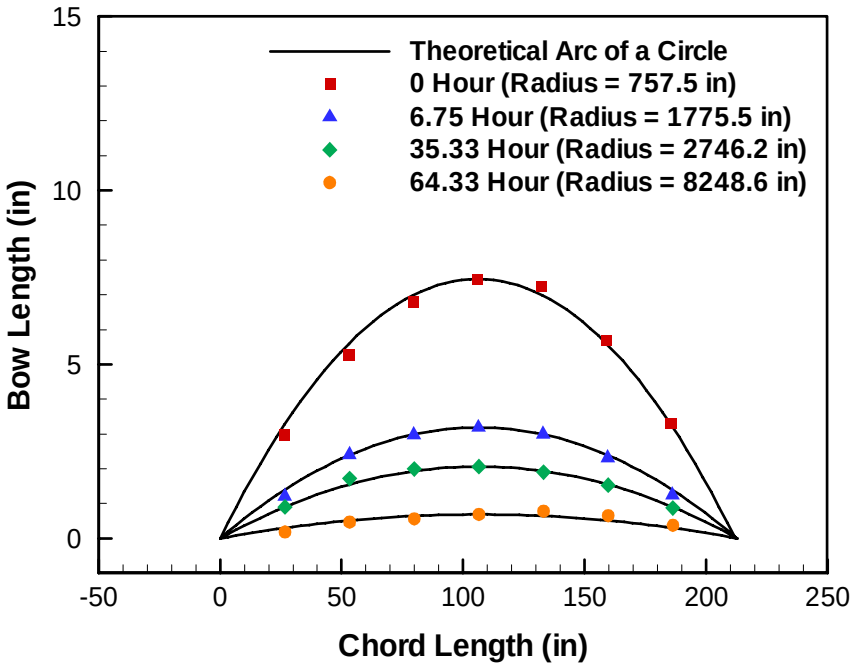

Figure 3.7 : The experimental results of the cambered web of the roll in comparison with the theoretical curve.

The results also indicate good repeatability in the experiment. However, depending on the location of cambered web taken for measurement (i.e. web section near the outer radius of the roll versus web section near the core), the extent of camber may be different. This can be explained by thinking in terms of deformation as a function of radius of the roll, where each subsequent layer may experience higher degrees of deformation than the previous layer. In conclusion,

the experimental results demonstrate that viscoelastic effect plays a role in the bagginess of plastic webs.

3.2 Baggy Edges from Slitting

The formation of baggy edges can originate from different sources, such as the result of winding a web with excessively high edge burrs following slitting process, unwinding of wound roll with starring defects and unsupported edge of a layer in the wound roll. Thus, in this study, edge burr of polyethylene web is measured with the assumption that the formation of baggy edges are caused by winding a web with excessive edge burr following slitting. This assumption was made when some of the polyethylene wound rolls received from the manufacturer was found to already contain baggy edges.

3.2.1 A Brief Review on Web Slitting

Slitting is a web handling process where a wide web is converted into a narrower form. As a result, edge burrs are generated. These edge burrs generally have out-of-plane deformation, as revealed in Figure 3.8; in the form of burr height, continuously distributed along the slit edge of the web. Studies [3,44,48,50,54,57,58] have proven that burr height typically depends on the slitting parameters. In addition, it is this distribution of edge burrs that may cause periodic baggy edges, thus creating baggy edge webs.

There are only a handful of publications on shear slitting [54]. Arocona et al. [3] investigated the relationship between cutting force and cutting speed for

plastic films. While Meehan et al. [57,58] discovered that the slitting force decreases when the cutting speed of dull knives increases, whereas it becomes independent of cutting speed for razor sharp blades. Likewise, they established that the angle of cut has an effect on the in-plane cutting force and thus stability of the slitting process.

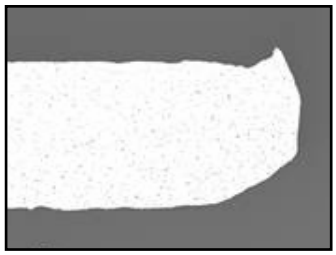

Figure 3.8 : An example of slit edge burr (aluminum) with out-of-plane deformation as observed from an SEM micrograph [54].

Lu et al. have also conducted studies on tangential shear slitting of webs for both plastic [50] and aluminum webs [54]. Lu et al. derived a solution for stress field distribution during razor slitting and demonstrated that web speed and tension influences the extent of the yield zone at the slit edges [44,48].

Lu et al. have also established the three stages of shear slitting [50], which are the *indentation stage* (initial), the *shearing stage* and the *tearing stage*. Lu et al. concluded that it is through these stages that the edge burrs are generated and the burr height dictates the quality of slitting hence indirectly the quality of the entire wound roll [50]. Lu et al. also concluded that a higher web speed is favorable when it comes to reducing the burr height, for rate-dependent viscoelastic materials such as polymeric webs.

3.2.2 Observation

Some of the 0.0025 inch thick polyethylene wound rolls received from the manufacturer already contain baggy edges generated during the slitting process. Therefore, the sample (web section) gathered to observe baggy edges was from one of these polyethylene wound rolls.

With the assumption of a new roll in mind, the ideal location to obtain web samples with baggy edges due to slitting process should be somewhere in the middle of the non-starring region as depicted in Figure 3.9. This was to avoid any potential confusion with other types of web defects, such as *starring patterns* or *v-buckling* defects [43] near the core and external damage from improper handling of the roll during storage near the outer radius of the roll.

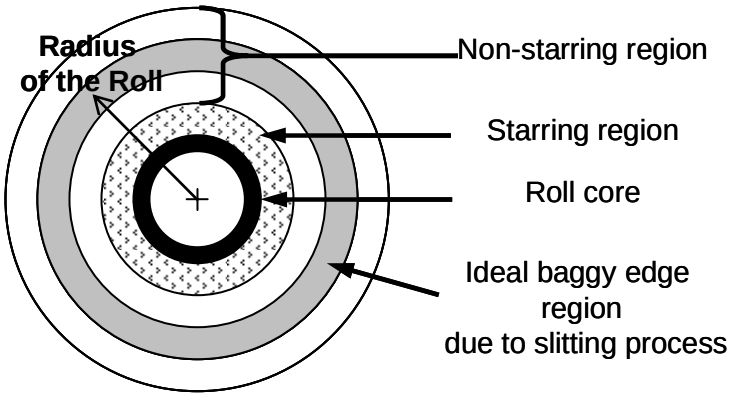

Figure 3.9 : Schematic of a wound roll depicting the location of selected baggy edge region due to web slitting, where web samples were obtained for the experiment to avoid any confusion with other types of web defects.

Newly untouched polyethylene wound rolls that have been removed from storage and have been partially used (several hundred layers unwounded) for

other experiments were identified; and checked for baggy edges generated from the slitting process. Once the roll has been identified, as depicted in Figure 3.10, it was then mounted on the winder. Additional layers were then unwound from the roll by hand to verify the existence of baggy edges generated from the slitting process, as shown in Figure 3.11.

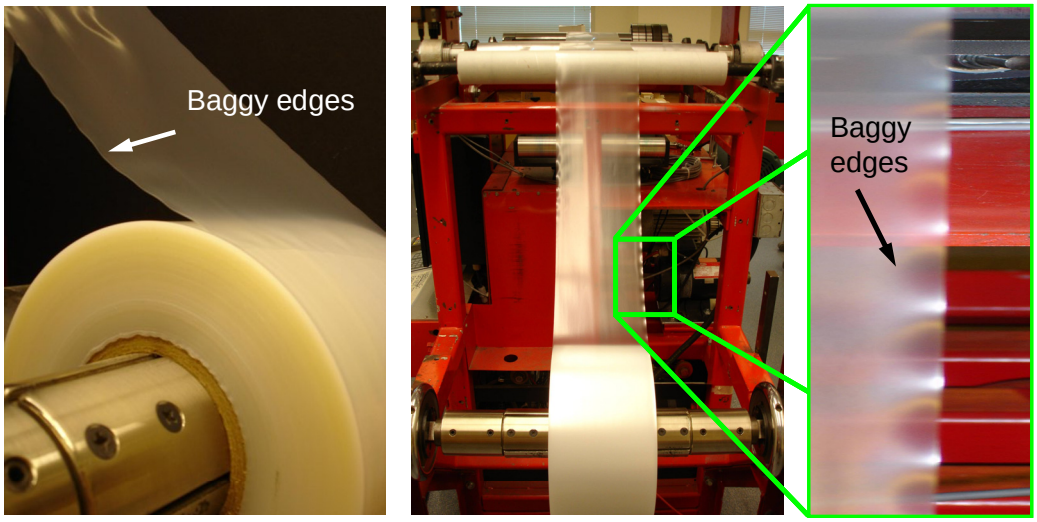

(a) (b) (c)

Figure 3.10 : Partially used polyethylene wound rolls that contain baggy edges generated from the slitting process: (a) side view, (b) frontal view, (c) magnified front view. Note the wavy edges indicated by the arrows.

A section of the web with baggy edges was removed for burr height measurement using a profilometer. The web section was placed on a flat transparent glass while a stylus needle from the *Mitutoyo Surftest 402* profilometer moved across the web section. The measurements obtained were meaningless, so several additional attempts were made and all gave a similar outcome. Subsequently, close observation revealed streak marks on the web

surface where the stylus needle had made the measurement. It was concluded that the stylus needle was actually “plowing” through the web, thus generating inaccurate data.

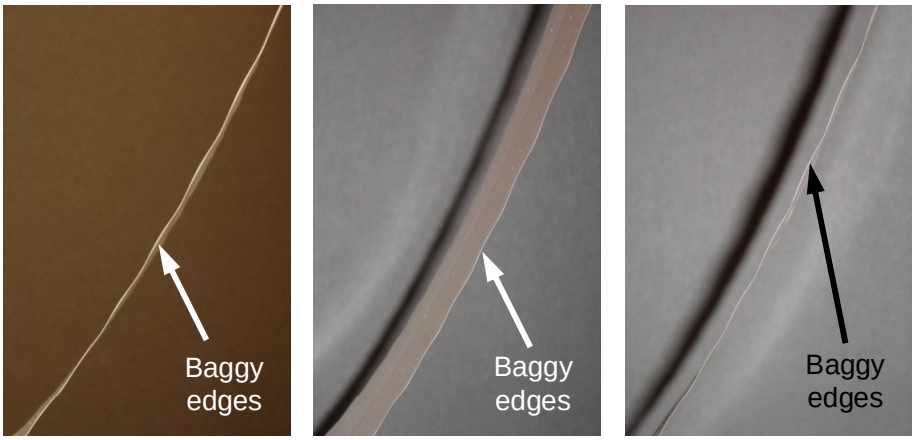

Figure 3.11 : Close examination on different sections of polyethylene web with baggy edges generated from the slitting process. Observe closely the wavy edges depicted by the arrows.

The investigation conducted by Lu et al. on burr height of aluminum web [54] pointed out the agreement between profilometer burr height measurements with wrapped-epoxy burr height measurement method under microscope. So, a slit edge polyethylene sample of 3/4 x 3/4 inch (length x width) was removed from the web using a pair of scissors. An aluminum clip was then used to act as a pedestal and hold the sample upright as illustrated in Figure 3.12(b) & (c). Both the clip and the sample were then cautiously placed into a cylindrical mold that was pre-coated with mold release.

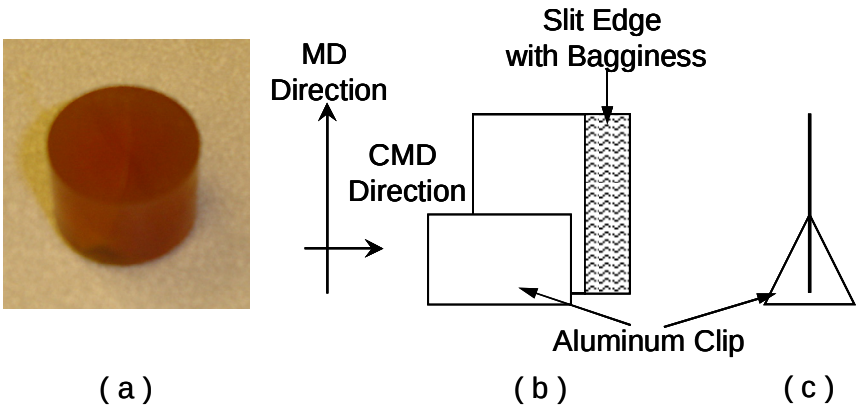

Figure 3.12 : (a) Sample used for observation encased in epoxy. (b) Illustration of the front and, (c) side view of polyethylene slit edge burr sample held by an aluminum clip for support.

Epoxy was then poured into the surrounding area of mold using a glass rod as a guide to prevent the polyethylene sample from bending out of shape. The purpose was to maintain the geometry of the burr; the epoxy acted as a stiffener to encase the thin delicate polyethylene web.

Once the epoxy had cured, the sample was removed from the mold as displayed in Figure 3.12(a). Then, the sample top surface was sanded down, to half-way near the aluminum clip in a sequence of sanding; from 240 grit (coarse) sandpaper to 600 grit (fine) sandpaper, followed by polishing on a polishing wheel. After polishing and drying, the cross-section of the sample was viewed using an optical microscope. Figure 3.13 shows the micrograph image of the web slit edge including the burr height at 200 times magnification.

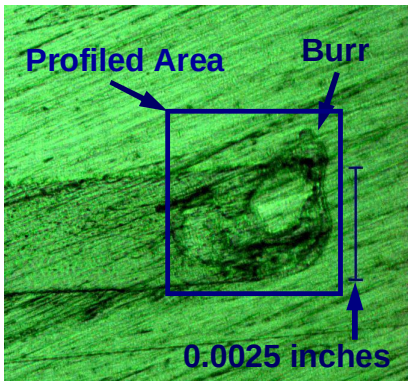

Figure 3.13 : Optical image of polyethylene slit edge burr.

3.2.3 Measurement, Results and Discussion

From the digital image, consisting of the entire cross-section slit edge including the burr height, the pixel coordinates were read and converted into actual web thickness. To accomplish this, vertical lines of 10 pixels spacing were drawn on the digital image to cover the entire area as indicated in Figure 3.13. Using the vertical lines as reference, the pixel coordinates that intersect the cross-section slit edge for each vertical grids were read and the length between the pixels was calculated. Thus, we have the thickness of the slit edge all the way to the burr edge in terms of pixels. Now we define pixel size as,

$$pixel\ size = \frac{(\ measured\ web\ thickness\ )}{(\ number\ of\ pixels\ )} \tag{3.6}$$

Through this conversion ratio (1 pixel = 13.81 μinches for this case), all the data collected from Figure 3.13 were converted to the actual slit edge burr height thickness profile in inches. The results from this conversion are plotted in Figure 3.14. The measured height of the edge burr from Figure 3.14 was 0.00075 inches (0.75 mil). Compared with the web thickness of 2.5 mil, it was determined

that an approximate increase of 30% in web gauge at the edge of the web was achieved.

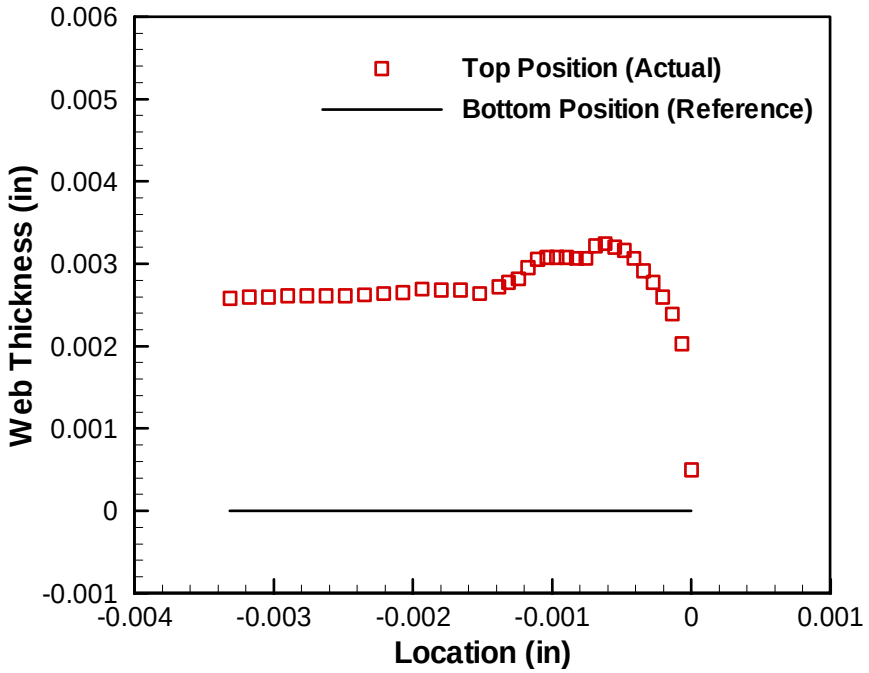

Figure 3.14 : Slit edge burr height thickness profile results of polyethylene webs with baggy edges generated from web slitting process.

This finding validates the existence of large edge burr that could possibly influence the formation of periodic baggy edges. In addition, with this profiling data, it is now possible to model the baggy edges caused by the slitting process, in finite element analysis.

3.3 Baggy Lane

In order to model *'baggy lanes'* realistically in finite element software, such as ABAQUS, or perform numerical analysis using in-house winding software, we need to know the winding parameters that cause *'baggy lanes'*. Therefore, in this

section we will focus on creating *'baggy lanes'* in the laboratory using a polyethylene web.

Furthermore, in the previous section viscoelastic recovery has been discussed for a cambered web. We will now investigate viscoelastic recovery of polyethylene web with *'baggy lanes'* in terms of recovery time through out-of-plane viscoelastic recovery behavior.

3.3.1 Creating Baggy Lane on Web

To create *'baggy lanes'* on webs, two different widths and thickness of wound rolls should be used. For example, a 6 inch wide, 0.005 inch thick wound roll will function as the main web while 1 inch wide, 0.0005 inch thick wound roll will act as the insert to create *'baggy lanes'*. In addition, both webs should be wound together as illustrated in Figure 3.15. This will steadily build up the simulated *'baggy lane'* with respect to the insert within the wound roll, while the entire wound roll builds up its diameter; thus producing a baggy web.

Unfortunately, due to the winder setup available in the laboratory, this option was not possible, thus, an alternative solution was used. Rectangular polyethylene strips of 1 inch wide and approximately 12 inches long were slit from the 0.0025 inch thick polyethylene wound roll. These strip inserts were used to create *'baggy lanes'*, with known winding parameters.

Then a wound roll of polyethylene web was unwound and rewound on the winder, shown in Figure 3.2, at low tension to check for traces of bagginess especially at the center of the web. This was to ensure that the original roll does

not contain *'baggy lanes'* before the experiment, and once the wound roll has been identified; the wound roll was unwound again on the same winder with the predetermined winding parameters listed in Table 3.2. The web guide, load cell, tension controller and torque brakes used in this experiment were identical to the ones described in Section 3.1.2.

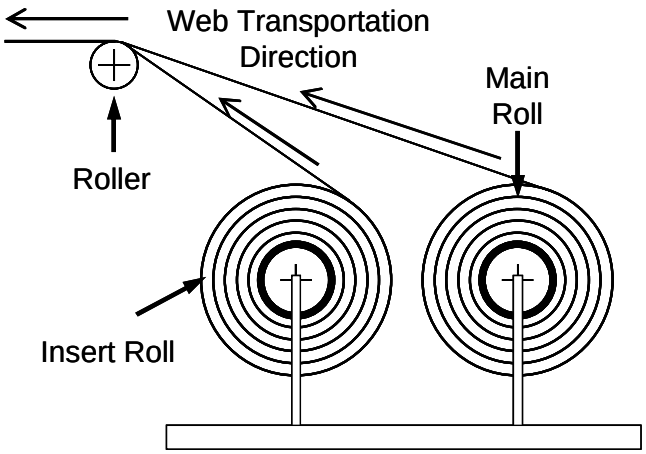

Figure 3.15 : Ideal configuration at the unwind section of web line to create *'baggy lanes'* on webs.

Material	Polyethylene
Web Thickness:	2.5 mil
Web Width:	6 in
Total Wound Roll Length:	- Unknown -
Number of Laps:	~ 60 layers
Winding Tension:	5 lb
Winding Speed:	4.3 ft/min
Insert Geometry:	Rectangular Strip
Insert Period:	Every 6 Revolution
Insert Thickness (A Stack of 6 Inserts):	0.015 in

Table 3.2 : Winding parameters used to create actual *'baggy lanes'* on webs.

As the web travels from unwound roll to the opposite side of the winder, the rectangular inserts were added into the rewound roll at periodic rate by attaching it to the middle of the web, as illustrated in Figure 3.16(a). The ratio of web layers to the number of inserts were, every 6 laps of polyethylene web to a stack of 6 inserts, thus causing a gradually build-up of 0.015 inches of displacement at the center of the wound roll. To control the progression of deformation caused by the inserts, the inserts were only allowed to wrap the circumference of the entire wound roll before having its excess trimmed off.

The winding was halted when the wound polyethylene roll reached approximately the 60th layer, as suggested in Figure 3.16(b). Through several failed trials, it was noted that if additional layers were wound onto the roll, wrinkling would occur due to large gauge difference between the center of the wound roll and the sides. Although the addition of a spreader or a rider roller should prevent this from happening somewhat; but due to the existing winder setup, it was not feasible.

Capitalizing on the viscoelastic effects of polyethylene, the entire wound roll was heat treated to soften the web in an environmental chamber at approximately 50^{o}C for more than a day then cooled down to room temperature over a time frame of 6 hours. This was to ensure that the web maintains its intended shape with *'baggy lanes'*, as demonstrated in Figure 3.16(c), for a longer period of time before recovering to almost a flat web.

Once the wound roll has been cooled to room temperature, the wound roll was then removed from the environmental chamber. At that point, the wound roll

of polyethylene with *'baggy lanes'* is ready to be used for other experiments and observations.

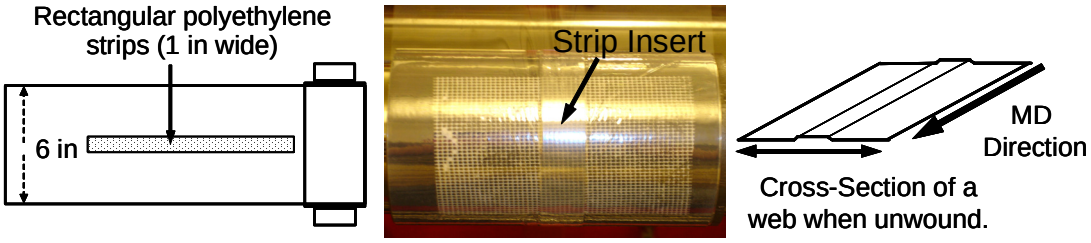

Figure 3.16 : Diagrams demonstrating the creation of actual *'baggy lanes'* on webs. (a) An illustration showing how rectangular inserts were added into the wound roll at periodic rate by attaching it to the middle of the web to create *'baggy lanes'*. (b) An example of a wound roll (polyester) with strips inserted into the roll to create *'baggy lanes'* on the web (dummy test). (c) An illustration of a web section with *'baggy lanes'* after it has been removed from the environmental chamber for heat treatment.

3.3.2 Baggy Lane Observation

In preparation for experimental observation of out-of-plane viscoelastic recovery behavior, a sample of the baggy web was slit from the wound roll as revealed in Figure 3.17(a). The sample was then placed on a flat and smooth polycarbonate block as demonstrated in Figure 3.17(b). Since the displacement of web center with *'baggy lanes'* was very small relative to the sides of the web, conventional measurements will not yield accurate data. Therefore, digital image processing method was used to observe the cross-section of the web across the width.

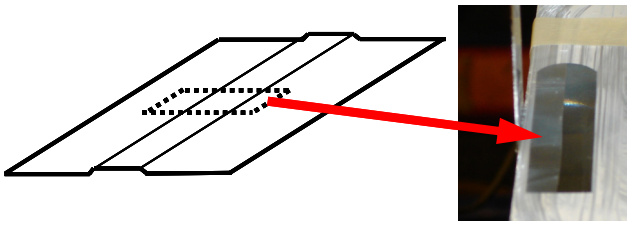

(a) (b)

Figure 3.17 : (a) An illustration indicating the location where the polyethylene section from (b) was removed with respect to the *'baggy lanes'* web. (b) A polyethylene section of baggy web removed from the *'baggy lanes'* wound roll placed on a polycarbonate block for observation of the out-of-plane viscoelastic recovery.

Equipment used in the observations consisted of a digital single-lens reflex (DSLR) camera (Nikon Model: D70s; 6 Mega-pixels) with a 10 times magnification lens, a camera tripod, a portable lamp and a short ruler. The equipment was set up as demonstrated in Figure 3.18.

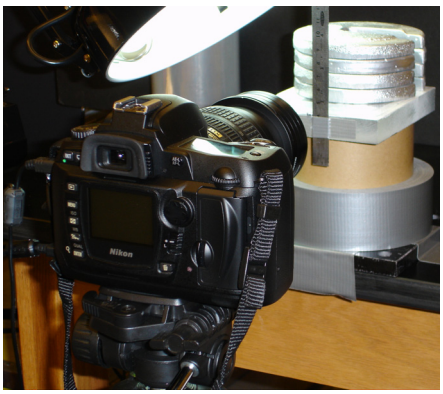

Figure 3.18 : Experimental setup used for observation of out-of-plane viscoelastic recovery.

The short ruler taped to the side of the polycarbonate block with duct tape in Figure 3.18 acts as a reference to length in terms of pixels for each image acquired by the camera, and will be used to calculate the displacement of the web. Since the observation was conducted over a short period of time, the creep of duct tape adhesive at room temperature was neglected.

Prior to attaching the camera onto the tripod, a beam leveler was used to ensure the camera was on the same leveled plane and elevation relative to the table. The polycarbonate block used to support the sample was elevated to meet the targeting reticule of the camera and additional weights were placed on the block to stabilize it. A portable lamp was attached to the table to provide additional lightning when capturing images, and was only turned on for no more than 3 minutes each time to prevent unwanted heating of the sample.

When acquiring images, the camera was controlled remotely and a timer was used to clock the time. Images acquired over time can be observed in Figure 3.19, whereas the actual displacement of the web were calculated and plotted in Figure 3.20. Overall, the entire observation lasted for approximately 6 days; and in terms of accuracy, the maximum time error was 3 minutes.

The reference length of the ruler used to determine displacement throughout all images acquired with 3008 x 2000 resolutions appeared to be consistently yielding 72 pixels to 1 mm, and the sequence of image positioning indicates no unwanted disturbance on both the camera and the table. Furthermore, by observing Figure 3.19 in sequence and reviewing the results

plotted in Figure 3.20, location # 1 seems to recover faster than location # 2 to a point where location # 1 will start to buckle when compared to location # 2.

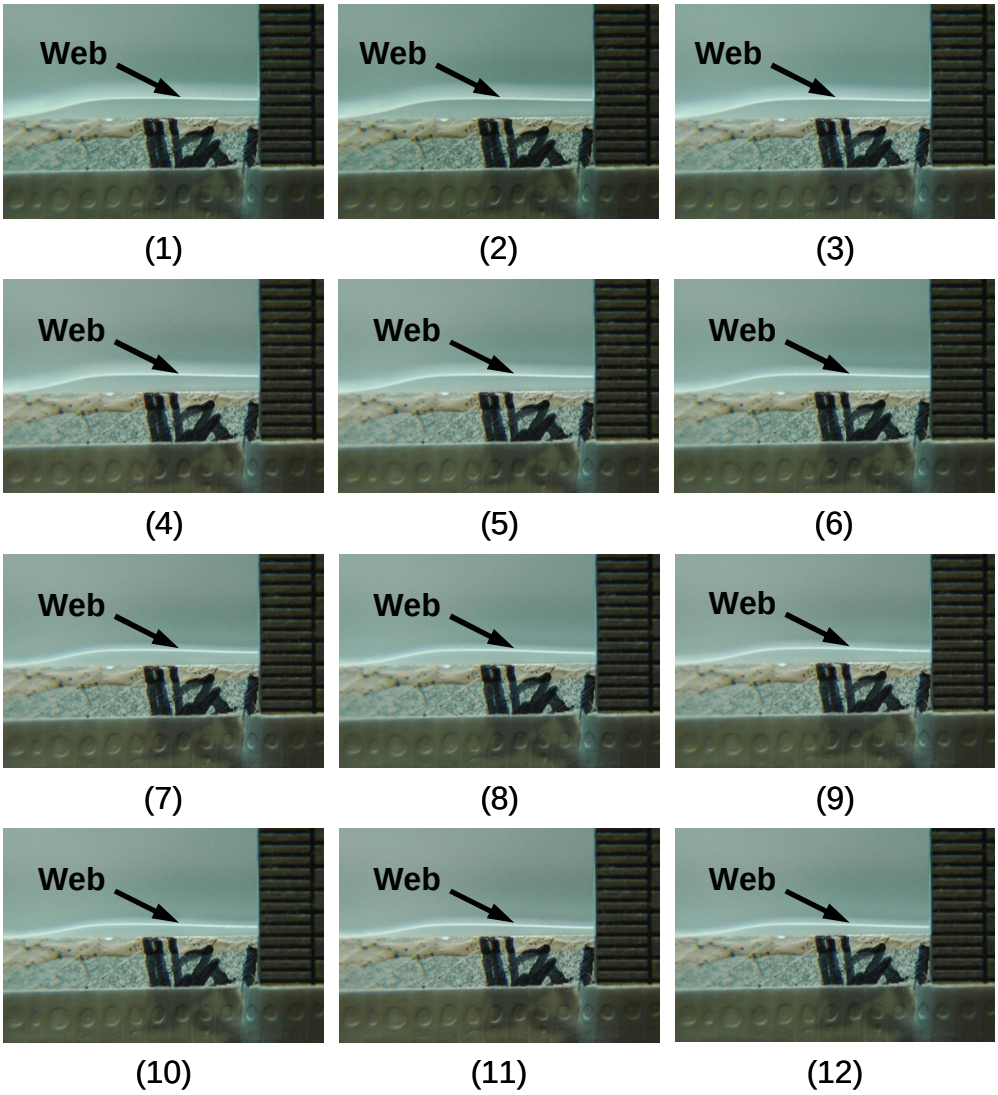

Figure 3.19 : Cross-section images of polyethylene web acquired in sequence from out-of-plane viscoelastic recovery behavior observation. The arrows point to the web and note the gradual change in position as the web recovers over time.

There are two possible explanations for this behavior: one is by thinking in terms of localized material yielding. Since location # 2 experiences higher

localized strain than location # 1 due to the stretching effect of the inserts, it is possible that location # 2 might require longer time to recover if it has not passed the localized yielding point of polyethylene.

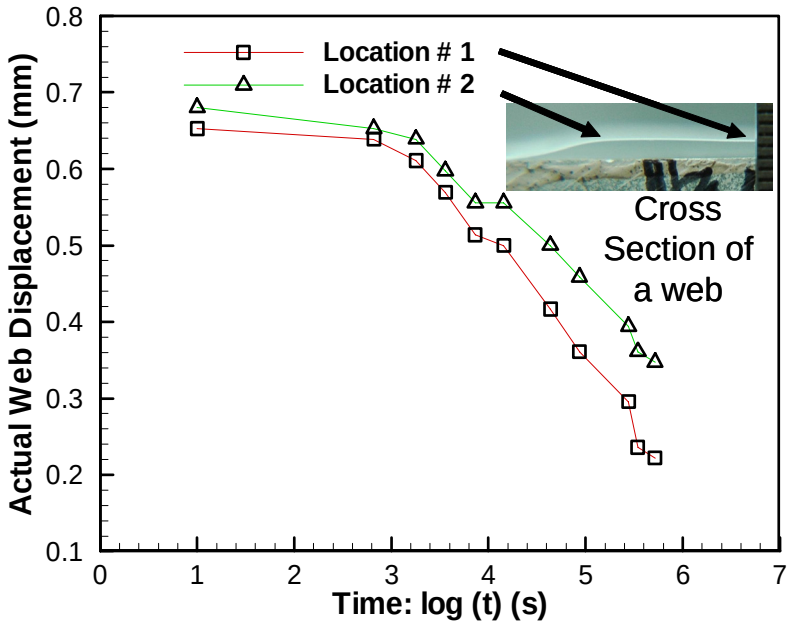

Figure 3.20 : Calculated actual displacement of the web with *'baggy lanes'* at different location.

Another possibility is during localized stretching of location # 2, some of the material at that point has been pushed to the side, making location # 1 become heavier and cause location # 1 to buckle due to the weight.

It may be noted that if we slit a web section of at least 12 inches in length from the wound *'baggy lanes'* roll and slice the web section into 3 parts, as demonstrated in Figure 3.21; the middle part will definitely be longer than the other two when laid on a flat table and measured with a ruler, thus proving that the web is baggy.

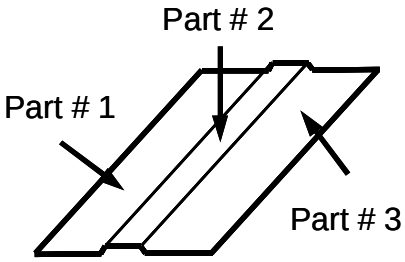

Figure 3.21 : An illustration describing how the web section should be sliced into 3 parts, then measure the length difference between each part to investigate the web bagginess.

3.4 Buckled or Wrinkled Web

Through the course of determining baggy webs, it was found that wrinkling formation was partly induced by baggy webs; especially when applied tension passes the critical point that cause the onset of troughs on a web. This consequently causes the web to buckle (out-of-plane) as shown in Figure 3.22.

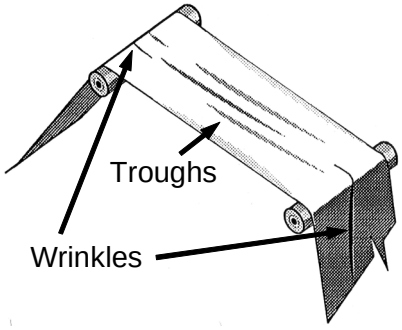

Figure 3.22 : The difference between troughs and wrinkles as indicated by the arrows in the diagram [17].

Therefore, a study was conducted to investigate the possibility of using *ABAQUS* (FEM software) to evaluate web behavior around rollers and the

formation of troughs at the onset of wrinkling under tension [96]. In this section, experimental measurement will be presented; specifically, using polyethylene web clamped at both ends to investigate the onset of wrinkling or critical buckling load from the effects of material properties and the influence of web geometric parameters.

3.4.1 A Brief Review on the Theoretical Development

Yu [95] derived the following expression to describe the critical stress at the onset of buckling,

$$\sigma_{cr} = \frac{\left(N_x \right)_{cr}}{t} = k \frac{\pi^2 E}{12\left(1-\nu^2 \right)} \left(\frac{t}{W} \right)^2 \qquad (3.7)$$

where L, W, t, E and υ corresponds to length, width, thickness of the plate, Young's modulus and Poisson's ratio. Also, note that k is a numerical factor, which depends on the magnitude of L/W ratio and some predefined boundary condition. This equation is based on the surface deflection, w, of buckled plate for simply supported edges, the strain energy, ΔU, for bending and the work done by compressive forces during the buckling of the plate in Timoshenko's book [84].

Equation (3.7) was assumed expandable to cover tensile loading with different constraints. Yu solved the k values by means of numerical analysis using *ABAQUS* software. Results for polyethylene web, clamped at both ends, can be referred to in Figure 3.23 based on the material properties listed in Table 3.3; and was compared to results obtained by Friedl et al. [21] on aluminum

plate. Overall, the results proved that the critical stress depends on the material properties and K_c, coefficient found from *ABAQUS* numerical analysis only depends on length to width (L/W) ratio.

Young's modulus, *E* (psi)	24010
Poissons' ratio, *v*	0.3
Web width, *W* (in)	2 or 6
Web thickness, *t* (in)	0.0025
Ratio of length to width, *L/W*	1.5 ~ 15

Table 3.3 : Polyethylene material properties used by Yu to solve for k value by means of numerical analysis [95].

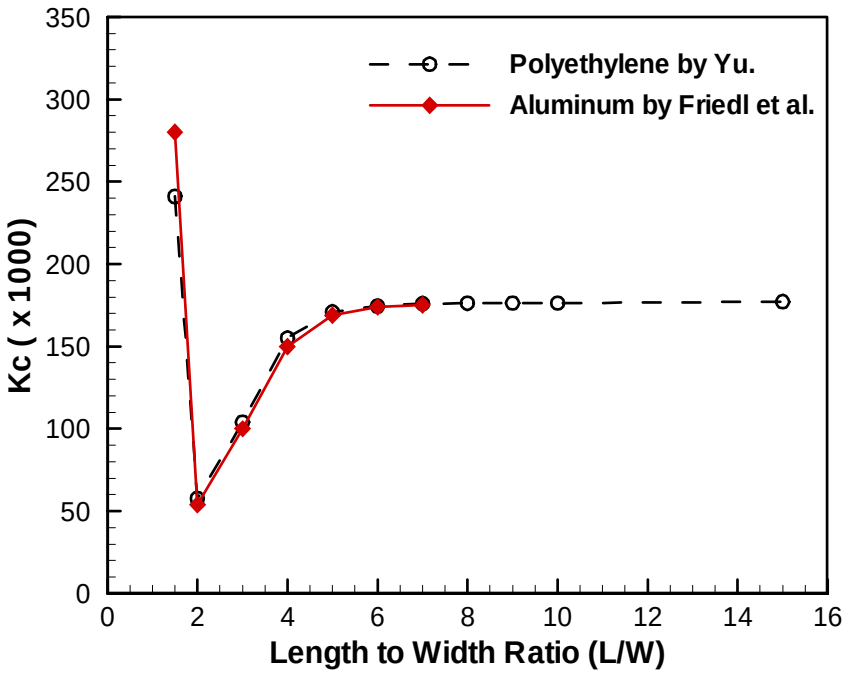

Figure 3.23 : Results from Yu's numerical analysis for polyethylene clamped at both ends [95] compared with Friedl et al. [21] buckling analysis on aluminum plate.

Yu did consider other cases of constraints in the numerical analysis and found that the other K_c factors changes in accordance to the defined boundary conditions; thus, there exists a threshold for the length to width (L/W) ratio that was approximated close to 2. Analysis also indicates that when critical buckling load increases, the stiffening of the boundary conditions will increase as well; thus, the coefficient K_c also depends on the boundary conditions.

3.4.2 Experimental Procedure

In this section, the experimental measurement and validation will be performed for the case where polyethylene was clamped at both ends. The experiments were conducted using 0.0025 in or 2.5 mil polyethylene web with known baggy characteristics. Strips of specimen were prepared accordingly, based on different length over width (L/W) ratios in the machine direction.

The tensile test were carried out using a dual column *Instron 4202 Material Testing Machine* with a 100 lb load cell attached at the top; connected to a *digital data acquisition system* for load and displacement data collection by the computer. Before conducting the experiments, the load cell was calibrated using dead weights to obtain the relationship between load and output voltage from the load cell; thus ensuring accurate readings by the data acquisition system.

During experiment, each sample was attached to the machine using steel clamps as demonstrated in Figure 3.24. Alignment was checked to ensure the webs were perpendicular to the clamps before applying the tension; since misalignment will cause the sample to tear in the lateral direction prematurely.

Figure 3.24 : Experimental setup used to determine the critical buckling load during the onset of wrinkling.

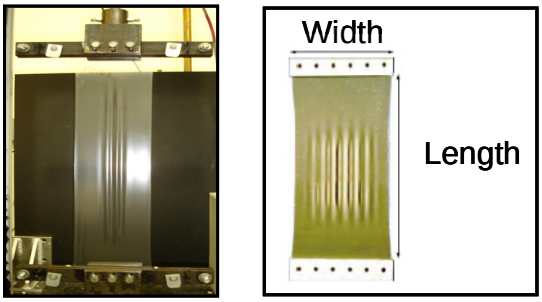

(a) (b)

Figure 3.25 : A comparison of wrinkled web: (a) observed during experiment at the onset of wrinkling and; (b) Cerda et al. observation [12]. Both observations look similar.

Then tensile load was applied via displacement control at 0.5 in/min until the onset of wrinkling; as demonstrated in Figure 3.25(a). When the onset of wrinkling occurs, the load applied was noted. Experimental observation appears to be similar to Cerda et al. observation [12] in Figure 3.25(b), where their primary interest was to determine the relationship between wavelength and

tensile strain. In addition, multiple experiments were conducted for the same length over width (L/W) ratio to check for repeatability.

3.4.3 Results and Discussion

Since theoretical buckling analysis gives the critical stress at onset of buckling, equation (3.7) was modified to match the collected experimental data. Load applied during experiment was on the longitudinal direction of the web or in-plane, so we have

$$\sigma_{cr} = \frac{F_{cr}}{Wt} \tag{3.8}$$

Combining both equation (3.7) and (3.8), leads to the following equation

$$F_{cr} = K_c \frac{\pi^2 E}{12\left(1-\nu^2\right)}\left(\frac{t^3}{W}\right) \tag{3.9}$$

where K_c is the coefficient found from *ABAQUS* numerical analysis, discussed earlier.

The theoretical buckling loads and experimental buckling loads during the onset of wrinkling were plotted in Figure 3.26. Since multiple experimental data were available for each specific L/W ratio, the average critical buckling load was used to represent the experimental characteristics. In general, the experimental observation agrees well with the numerical results obtained by Yu.

From this result, several features should be noted. The highest critical buckling load occurs when length to width ratio is approximately 1.5 while the lowest critical buckling load occurs when the length to width ratio is equal to 2

then gradually increases till length to width ratio becomes 5 where the K_c curve reaches a constant value.

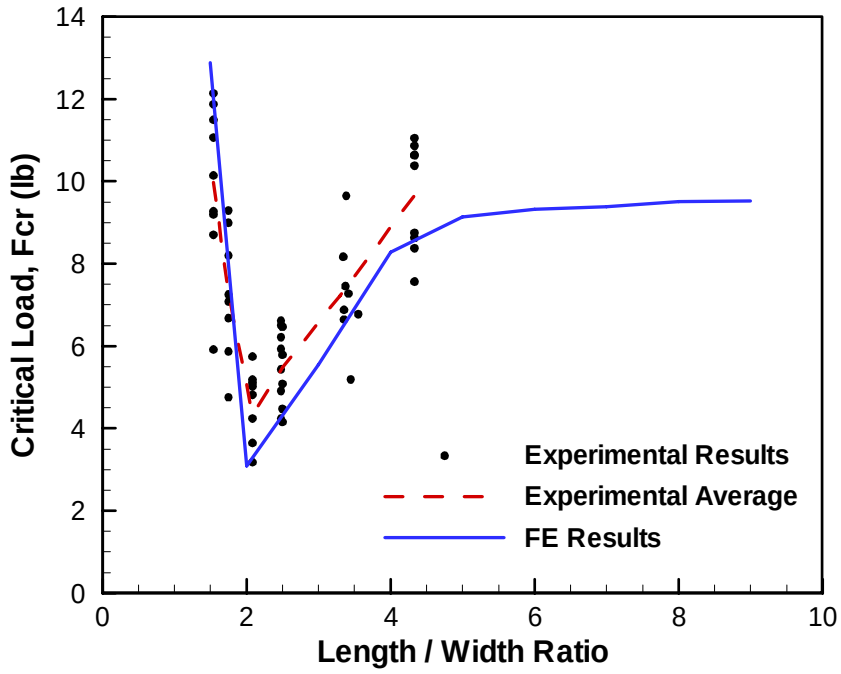

Figure 3.26 : Comparison between theoretical critical buckling loads obtained through numerical analysis and experimental critical buckling loads during the onset of wrinkling.

Also, experimental data collected for L/W ratio of approximately 3.33 were compared to the theoretical prediction in Figure 3.27 for repeatability verification. In general, the results were close; thus, it can be concluded that the observed experimental data during the onset of wrinkling were acceptable.

Experimental errors can be attributed to misalignment of the samples. Another possibility can be attributed to poor preparation of the samples, resulting in premature tear of the sample and may, also be due to excessive clamping of the samples.

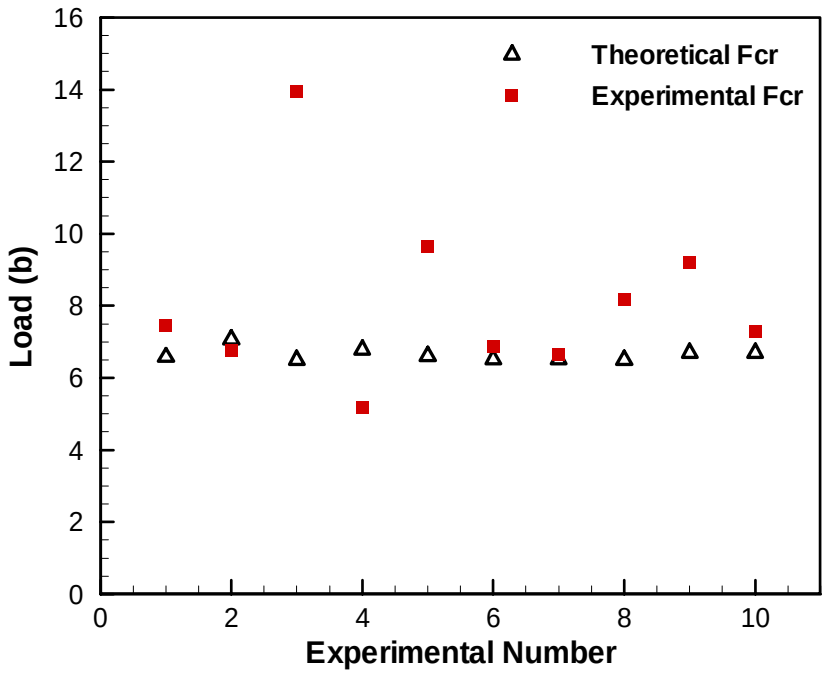

Figure 3.27 : Repeatability validation; load value where wrinkling initially occurs versus number of experiments conducted for length to width ratio of approximately 3.33.

3.5 Chapter Summary

At this point, cambered web, baggy edges and baggy lanes in terms of web bagginess have been covered. However, it will not be possible to model these cases accurately since there is still lacking in additional material properties; specifically viscoelastic material properties. Therefore, the following chapter will address the viscoelastic material properties.

Finally, investigation into buckled or wrinkled web reveals that *ABAQUS* cannot handle the boundary conditions properly at this time. Hence, it does not apply to actual web handling situation and is only presented for future references.

CHAPTER 4

ACCELERATED MATERIAL PROPERTY TESTING ON POLYETHYLENE WEB

In this chapter, viscoelastic properties will be characterized in both in-plane and out-of-plane directions for polyethylene web. Time-temperature superposition principle will be used to determine the master curves to predict the long-term viscoelastic behavior of webs and the formation of web bagginess through modeling.

4.1 Background on Viscoelasticity

A brief review on viscoelasticity and accelerated time testing methodology will be discussed. It will be divided into several short sub-sections; consisting of viscoelastic models, the difference between relaxation and creep including the justification on the experimental aspects of this chapter, and finally, a description of accelerated time-testing methodology; focusing specifically on time-temperature superposition principle.

4.1.1 Viscoelasticity, A Brief Review

Unlike typical elastic-plastic materials (i.e. steels, aluminum at room temperature) that follow Hooke's Law within the limit of linearity, most polymeric

materials have different mechanical behavior. Polymeric material loses energy when load is applied onto it [59] and will rearrange itself in the molecular level to accommodate for the stresses [56], hence independent from strain level [36]. When load is removed, the material will attempt to recover back to its original state.

This behavior is identified as viscoelastic behavior. Concurrently, this area of study is commonly known as viscoelasticity and is associated with analysis of stress and deformation of materials exhibiting time dependent behavior. There are various approaches in modeling viscoelastic behavior and the chart in Figure 4.1 gives an overview of this; however, this chart is not absolute since there are still researches being carried out in this area.

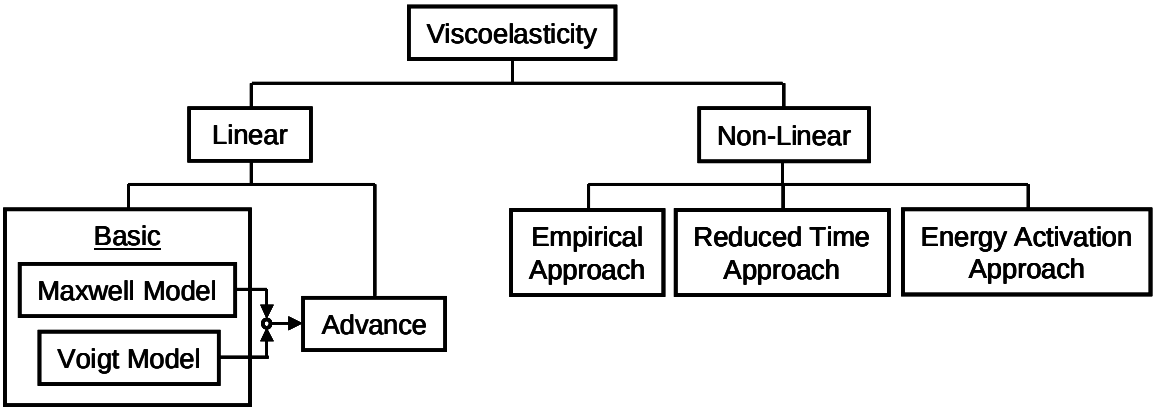

Figure 4.1 : An overview of various approaches in modeling viscoelastic behavior [36].

Briefly, most polymeric materials undergoing small deformation can be explained using linear viscoelasticity; however, some materials do exhibit nonlinear behavior at small deformations. The simplest way to mechanically

describe linear viscoelastic behavior is by using an elastic spring, a viscous damper or a combination of both. Common models in this category are the *Maxwell Model*, *Voigt Model*, *Standard Linear Solid Model*, *Generalized Maxwell Model* and *Generalized Voigt Model*. Unfortunately, these analog models have no physical demeanor in terms of the molecular mechanisms of polymeric material [36]. In addition, linear viscoelasticity can be summarized by using Boltzmann Superposition Principle [19].

In most realistic cases of viscoelastic materials, where large deformations (i.e. above 5% strain levels) are observed, or when the materials itself changes properties under deformation; linear viscoelastic models can no longer provide dependable analysis of mechanical behavior. This has been proven from works on polycrystalline ice [72], biological materials [23], and plastics [27,39]. Although there are numerous possibilities that cause nonlinearities in polymeric materials, but it will not be discussed in this study; further reading can be obtained elsewhere [19,36,41,92].

For completeness, nonlinear viscoelastic constitutive models are generally used to analyze the mechanical behavior of realistic viscoelastic materials and are classified into several approaches, mainly empirical approach [20,40], energy activation approach [2,6,16,31] and reduced time approach [34,37,74].

4.1.2 A Justification between Relaxation versus Creep

In any polymeric material, there are two inter-related viscoelastic aspects; *relaxation* and *creep*. Relaxation is associated to stress reduction as time

progresses when the material is held at a constant strain, whereas creep is related to strain increase with time when the material is held at a constant stress; under isothermal conditions. Therefore, *relaxation modulus* defines the ratio of stress at different time relative to the applied constant strain, while *creep compliance* describes the ratio of strain at different time corresponding to the applied constant stress. Due to these inter-relations, both relaxation modulus and creep compliance can be inter-converted from one to the other based on their inter-relation.

Based on the understanding of relaxation and creep, all the experimental data collected in this chapter will be initiated from the relaxation test approach; where relaxation measurements will be conducted on polyethylene webs. At the same time, the term *in-plane* is defined to be the tangential direction of the polyethylene web, commonly known as machine direction (MD), while *out-of-plane* represents the radial direction of the web or cross-machine direction (CMD); for clarity. Both in-plane and out-of-plane data will be analyzed respectively, to obtain the relaxation modulus and are then converted to obtain the creep compliance.

The purpose for this approach is to thwart any possibility of non-uniform strain distribution from the polyethylene web during experiment that can cause nonlinear viscoelastic behavior. This approach is justified from a study presented by Lu and Knauss indicating the extent of nonlinearity was determined by strain, rather than stress of the polymeric material [47].

4.1.3 A Brief Review on Accelerated Life Time Testing

There are a number of methods that can be used to measure viscoelastic behavior and they are not limited to the following methods; standard creep test (ASTM-D2990), stress relaxation test (ASTM-D2991) and DMA (Dynamic Mechanical Analysis) frequency scan. The selection for the measuring method is pre-determined by experimental objectives and application, such as test duration, type of specimen and water immersion requirement.

Justification is made in Section 4.1.2 to use the relaxation approach to conduct the measurement in this chapter. However, relaxation test approach to characterize long-term viscoelastic material properties at room temperature would be impractical; especially when the intended long-term duration is expected to cover at least 1 year.

Since long-term viscoelastic material properties relies on an array of attributes including time, temperature, physical aging time, moisture content level and material degradation [46]; in addition, it has long been documented that long-term viscoelastic material properties can be performed at short time period under modified environmental settings so as to accelerate the time scale. Therefore, an accelerated life-time testing technique will be utilized for this study.

Accelerated life-time test is defined as a short-term test that produces measurement data, which can later be processed to predict actual long-term viscoelastic behavior [36]. There is a wide range of accelerated life-time testing techniques available, which include time-temperature superposition [51,94], time-aging time superposition [79], time-stress superposition [73], time-frequency

superposition [60] and Arrhenius type accelerated chemical degradation approach [15].

In this study, the accelerated life-time test based on time-temperature superposition will be used. The long-term thermo-mechanical viscoelastic material behavior (relaxation and creep) can be established from a series of short-term tests at elevated temperatures. The technique was originally proposed by Williams, Landel and Ferry in 1955, in the form of

$$\log a_T \cong -\frac{C_1\left(T - T_s\right)}{C_2 + \left(T - T_s\right)} \tag{4.1}$$

where $\log a_T$, T_s, C_1, C_2 denote the shift factor, reference temperature and constant coefficients respectively. This equation is referred to as the *WLF Equation*.

The shift factor, a_T, is defined to be a numerical value whereby a curve must be moved. And depending on the selected reference curve/temperature, the other experimental curves will either move to left or right along the horizontal axis (time scale) to overlap with the neighboring curves. Moving a curve to the left only happens when the experimental curve temperature is lower than the reference curve temperature. Similarly, moving to the right only occurs when the experimental curve temperature is higher than the reference curve temperature.

The constant coefficients (C_1 and C_2) can be obtained by fitting a curve on the plotted shift factor used to produce the long-term viscoelastic function. From literature presented by Williams et al. [94] C_1 and C_2 were estimated to be 8.86 and 101.6 respectively, according to the averaged value obtained from a

large number of polymers with the condition that T_s = ±50°C from the glass transition temperature T_g. Also, if $T_s = T_g$, then C_1 and C_2 will become 17.44 and 51.6 respectively.

In summary, this technique allows the gathering of all short-term viscoelastic behavior at their respective elevated temperatures, from experiments at same strain level, to construct a corresponding viscoelastic function; also commonly known as a master curve, over a specific time period, that describes the long-term viscoelastic behavior at some pre-define reference temperature.

4.2 In-Plane Viscoelastic Material Properties

Typical winding conditions [18] for polyethylene webs are listed in Table 4.1. In-plane relaxation experiments were then conducted, to construct the master curves for polyethylene webs at 1% and 3% strain levels; to cover both extreme ends of the listed winding conditions.

Modulus of Elasticity, E :	~ 24000 psi
Winding Tension, P :	0.5 – 2 pli
Estimated Strain on Web :	~ 0.8 – 3.3 %

Table 4.1 : Parameters for typical winding conditions of 2.5 mil polyethylene web.

For the case of 1% strain level, short-term relaxation experiments were conducted at temperatures such as 24°C, 28°C, 30°C and 32°C; whereas 3% strain levels, experiments were performed at 22°C, 31°C, 33°C, 35°C and 40°C. The temperatures for each strain level were selected to ensure that each short-

term relaxation curve would overlap properly with its neighboring curves when it was shifted horizontally to form the relaxation master curves.

Each test was performed over a time period of 1600 seconds to make certain that the relaxation master curve would be able to cover a time frame of one year. Time-temperature superposition [51,94] was used to analyze the data and to predict the long-term relaxation behavior. The creep compliance was also obtained by converting the relaxation data into creep compliance data, hence allowing the possibility of in-plane viscoelastic material property characterization.

4.2.1 Experimental Procedure

Strips of polyethylene web (0.0025 inches thick) were used as the test samples, for the in-plane accelerated life-time testing. Since 1% and 3% strain levels were planned for the in-plane relaxation experiments, the strips were prepared accordingly, the different fixtures and load cells used for each individual test sets, are listed in Table 4.2. Initial gage length boundaries (perpendicular to the strip) were marked on the prepared strips, according to Table 4.2, as illustrated in Figure 4.2; with an extra fine point *Sharpie Permanent Marker* for reference. The glass transition temperature, T_g of polyethylene webs is below room temperature (between -90^{o}C to -125^{o}C); hence no annealing process was carried out.

Equipment used to conduct the short-term relaxation experiments consist of Instron 4202 screw-driven material testing machine, a temperature chamber, a digital data acquisition system, two pairs of fixtures (for 1% and 3% strain levels),

a type-K thermocouple with thermocouple reader, a 100 lb load cell and a 5 lb load cell. The schematic of the experimental setup is depicted in Figure 4.3(a), whereas the actual setup can be seen in Figure 4.3(b); together with the test machine and control console. The console displays crosshead displacement, load and crosshead speed; while the output was conditioned for compatibility with the data acquisition system, which was connected to the computer for data recording.

Strain Level (%)	Size of PE Strips (in)		Initial Size of Test Area (in)		Machine Settings	
	Length	Width	Length	Width	Extension (in)	Speed (in/min)
1	12	1	6	1	0.06	3.6
3	12	3	8	3	0.24	14.4

Table 4.2 : Experimental conditions for in-plane relaxation test, dimensions for polyethylene strip specimen, gage length specifications and material test frame settings.

LabView was used to capture the load and time data when the experiment commences and to ensure accurate readings of the data by LabView, the load cells (both 100 lb and 5 lb) were calibrated by loading it with dead weights to obtain a linear relationship between load and output voltage from the load cell. This procedure was executed prior to initiation of the relaxation experiments for its respective strain levels. For 1% strain level condition, the 5 lb load cell was used for the relaxation test, while the 100 lb load cell was used for 3% strain level condition.

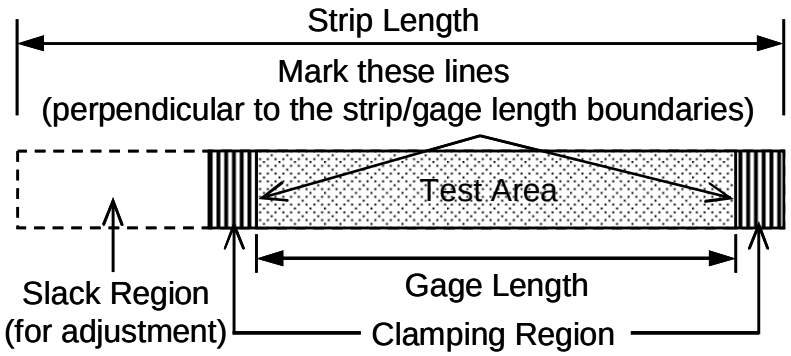

Figure 4.2 : An illustration of the prepared polyethylene strip specimens.

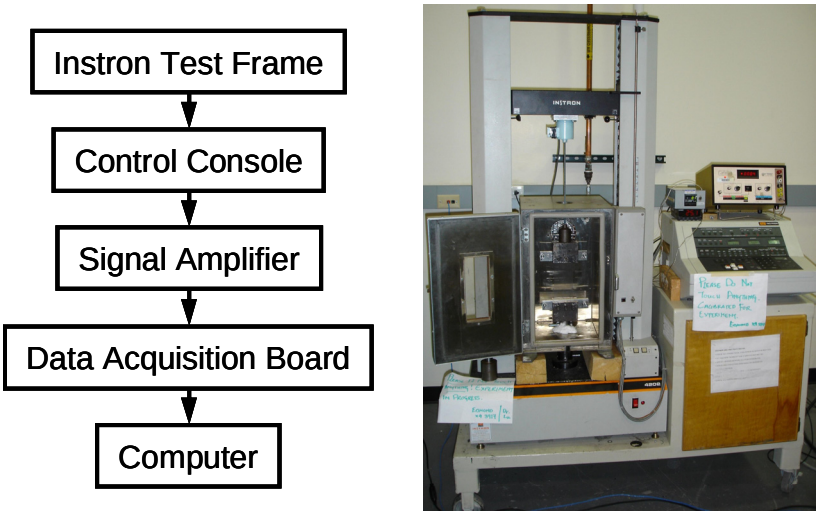

(a) (b)

Figure 4.3 : Experimental setup for in-plane relaxation test; (a) schematic of the setup, (b) actual setup of the test machine and control console.

When preparing for each relaxation test, a strip sample was pre-clamped at the clamping region while maintaining the correct pre-determined gage length; using the gage length boundaries as a reference, indicated in Figure 4.2, with aluminum clamps before attaching to the machine. In addition, this allows preliminary adjustment of the test sample alignment with respect to the clamps

using the slack region before tightening the grips. Prepared samples were then attached to the testing machine. Figure 4.4 provides a demonstration, for the case of 3% strain level. The test area indicated in Figure 4.4(b), represents the region to be uniformly deformed when the pre-determined strain level is applied; and the length of that region will be referred to as the gage length. After attaching the clamps with prepared test sample to the machine, alignment of the test sample with respect to the fixtures was rechecked using a protractor and the initial gage length of the test sample was also re-measured using a digital caliper without touching the entire fixture for certainty.

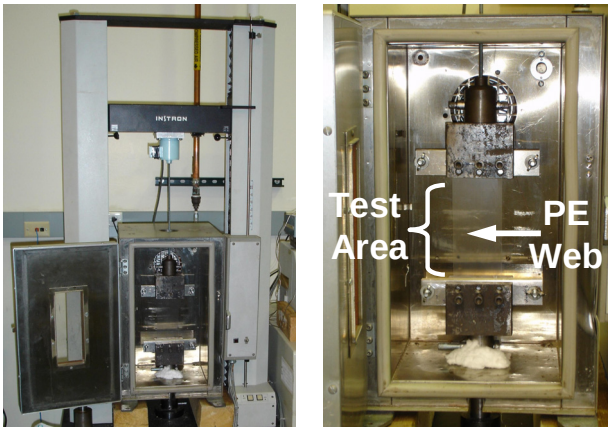

(a) (b)

Figure 4.4 : A prepared strip sample attached to the machine in preparation for relaxation test under 3% strain level condition; (a) an overview of the sample relative to the entire test frame, (b) close-up view of the sample inside the temperature chamber.

A thermocouple was placed near the center of the test sample before closing the temperature chamber and heating it to the desired temperature.

When the thermocouple reader indicates that temperature within the chamber has been stabilized at the desired temperature, the entire setup was maintained for another 30 minutes to ensure that the test sample and chamber had reached thermal equilibrium.

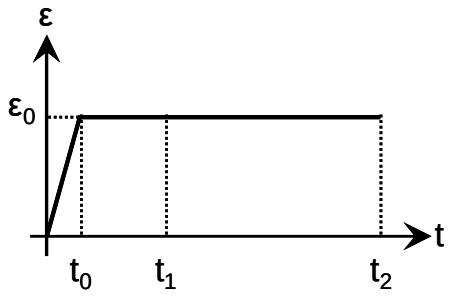

Figure 4.5 : A graph indicating the progress of applied strain with time from the onset of relaxation test: ε_0, t_0, t_1, t_2 represents the applied strain level on test sample, *rise time* of the experiment, initial data point for all plotted results and the time where test is halted respectively.

When thermal equilibrium had been reached, the test sample was then strained to the desired strain level by applying strain that follows the ramp profile displayed in Figure 4.5. From Figure 4.5, ε_0 represents the applied strain level on the test sample; while t_0 denotes the *rise time* of the experiment. *Rise time* is defined to be the amount of time it takes for the testing machine to generate the desired strain level on the sample. Ideally, the desired strain input should follow a step function profile to simulate instantaneous strain on the test sample based on viscoelastic theory. But in reality, this is not feasible thus an alternative route was used instead; which was a ramp function profile. To maintain consistency

throughout the in-plane accelerated life-time testing, a rise time of 1 second was used for every experiment.

Load and time data were recorded at a sampling rate of 1 Hz (one data point per second) on the data acquisition system that was controlled by LabView whilst the test sample was allowed to relax. Each test lasted 1600 seconds (approximately 27 minutes). Finally when all the relaxation experiments were completed, the collected data from each test were analyzed and plotted using *Tecplot* for visualization and characterization of in-plane viscoelastic material property.

4.2.1.1 Stress and Strain to Relaxation Modulus

The relaxation strain level refers to the engineering strain; which is defined to be the change in length, ΔL divided by the initial length of the test sample, L within the gage length and the expression in terms of percentage comes in the form of,

$$\varepsilon_p = \frac{\Delta L}{L} \times 100\,\% \tag{4.2}$$

For example, 3% strain level is desired for relaxation test and the prepared strip sample has the length of 12 inches. After attaching the aluminum clamps, the initial length will be reduced; thus it is determined that the initial gage length of the test sample will be 8 inches. At this point, ΔL is calculated to be 0.24 inches. This number represents the required displacement needed by the machine to perform the relaxation test correctly, for 3% strain level with initial gage length of 8 inches. Similarly, the machine only recognizes the speed setting

in terms of inch per minute. Therefore, if we wish to have a rise time of 1 second, the input speed on the machine should be 14.4 in/min. This explains all the parameters given in Table 4.2.

The relaxation modulus can be calculated using,

$$E(t) = \frac{\sigma(t)}{\varepsilon_0} \tag{4.3}$$

where $\sigma(t)$ denotes the engineering stress (ratio of load to the undeformed cross-sectional area of the sample at the test temperature) as a function of time and ε_0 represents the constant strain applied on the sample.

4.2.1.2 In-Plane Repeatability Testing and Verification

The last area that needs to be addressed is the repeatability verification of the entire in-plane relaxation experiment. This was accomplished by taking all three in-plane relaxation data at room temperature at identical strain level. Results on relaxation modulus are plotted in Figure 4.6. The comparison curve of each experiment against the calculated average of these three curves indicates that data are, in general repeatable with maximum difference about 5.5%. Therefore, it is proven that the entire in-plane relaxation experiment has good repeatability from Figure 4.6.

4.2.2 Relaxation Modulus

In previous section, strain in the form of ramp profile was used when conducting relaxation experiments; instead of step strain profile due to physical

limitations in experimentation. Now revisiting that discussion from theoretical perspective, there is dissimilarity between ramp and step loading on viscoelastic material response at the initial stages; ramp loading starts gradually then it peaks while step loading starts instantaneously to reach the peak. However, if the ratio of rise time is small compared to the initial time period, then eventually the response for both ramp and step loading will be approximately the same.

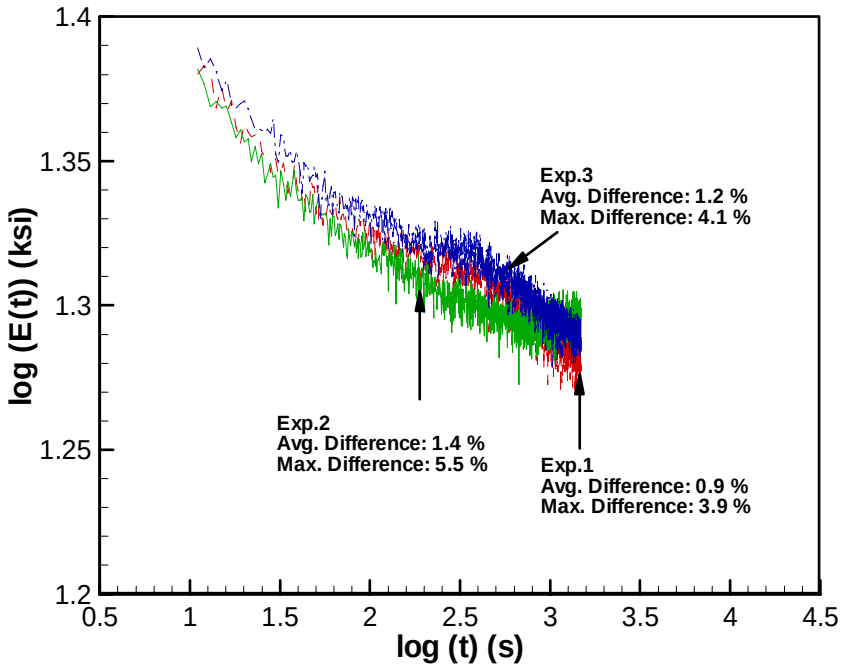

Figure 4.6 : In-plane relaxation curves at 3% strain level, 22^{o}C with rise time of 1 second for repeatability verification of the in-plane relaxation data.

Therefore, to maintain consistency throughout the entire experiment and accuracy of the experimental results, all plotted relaxation curves have the initial data point starting at t_1 = 11 seconds; omitting the first 10 seconds of experimental data, as illustrated in Figure 4.5. Additionally, it should be noted that the results presented herein represents the averaged data among the

multiple tests (at least 3) conducted for each temperature zone at their respective strain levels.

The relaxation modulus for 1% strain level at different temperatures is shown in Figure 4.7, whereas the 3% strain level results is in Figure 4.8. From observation of both plotted figures, the relaxation modulus decreases as time and temperature increases.

Time-temperature superposition was applied to obtain the relaxation master curves (long-term) for both 1% and 3% strain levels from the plotted short-term relaxation modulus curves in Figure 4.7 and Figure 4.8. Individual curves at different temperatures for each respective strain levels were shifted horizontally, using room temperature as the reference temperature to form the respective relaxation master curves.

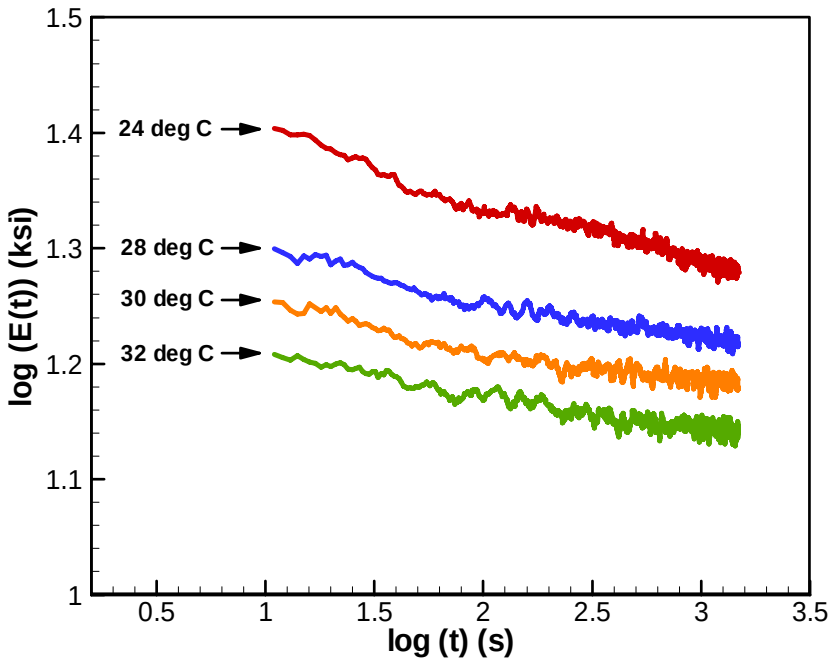

Figure 4.7 : In-plane relaxation modulus curves at different temperatures for 2.5 mil polyethylene web at 1% strain level.

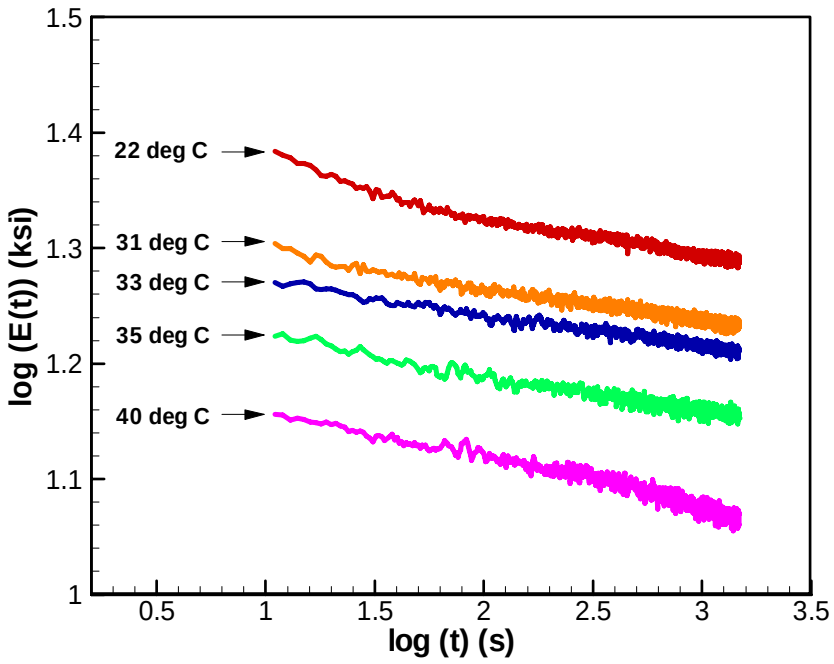

Figure 4.8 : In-plane relaxation modulus curves at different temperatures for 2.5 mil polyethylene web at 3% strain level.

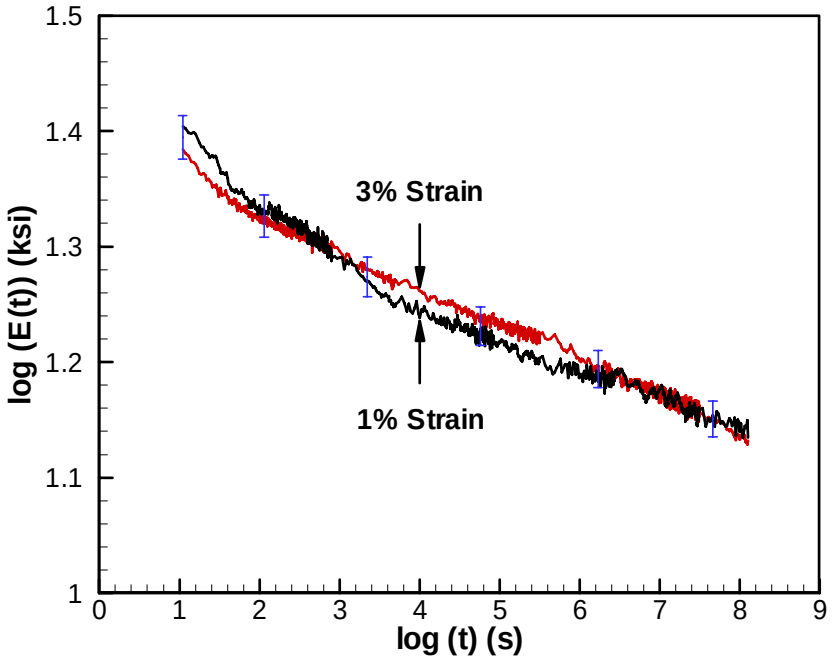

Figure 4.9 : In-plane relaxation master curve for 2.5 mil polyethylene web at 1% and 3% strain.

The relaxation master curve for 1% and 3% strain level are shown in Figure 4.9 and the shift factors used to move the relaxation curves at different temperatures to construct the master curve are tabulated in Table 4.3. It is noted that for 1% strain level, the relaxation master curve starts at 25.3 ksi and ends at 14.4 ksi; hence the change in relaxation modulus over the period of 1 year is 43.1%. In the case of 3% strain level, the master curve begins at 24.2 ksi and stops at 14.4 ksi; thus the change in relaxation modulus over 1 year is 40.7%.

Strain (%)	Shift Factors at Various Temperatures (s)				
3	22 deg. C	31 deg. C	33 deg. C	35 deg. C	40 deg. C
	0	1.858	2.662	4.458	6.459
1	24 deg. C	28 deg. C	30 deg. C	32 deg. C	-
	0	1.759	3.259	4.959	-

Table 4.3 : Log_{10} shift factors (in seconds) used to determine 1% and 3% strain level relaxation master curves (in-plane).

Strain	3%	1%
C_1	52.988	61.444
C_2 (K)	141.507	135.753

Table 4.4 : WLF equation constant coefficients for 1% and 3% strain level (in-plane).

The shift factors used for both 1% and 3% strain levels listed in Table 4.3 are plotted in Figure 4.10. In addition, the constant coefficients; C_1 and C_2, for

WLF equation (equation (4.1)) was solved for each strain level and the results is displayed in Table 4.4 for future reference.

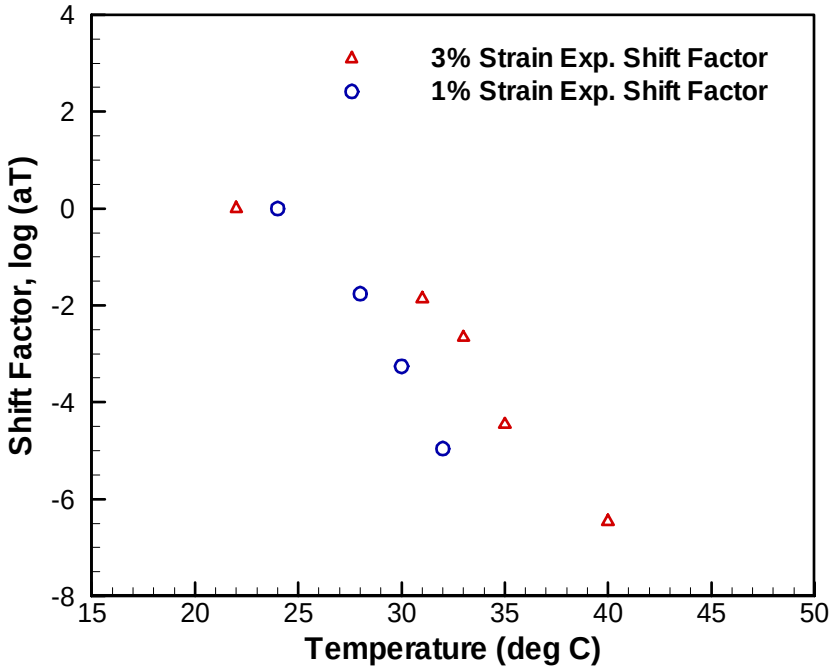

Figure 4.10 : Plotted shift factors used to determine 1% and 3% strain level relaxation master curves (in-plane).

In fact, when the relaxation master curves for both 1% and 3% strain levels in Figure 4.9 were examined, it was concluded that the in-plane relaxation master curves exhibits linear characteristics. With this conclusion, both relaxation master curves were combined and the averaged relaxation master curve is plotted in Figure 4.11.

Additionally, the average relaxation master curve was fitted using *Prony Series* as demonstrated in Figure 4.11. The *Prony Series* expression used for relaxation modulus master curve fitting is,

$$E(t) = E_{\infty} + \sum_{i=1}^{n} E_i \exp\left(-\frac{t}{\tau_i}\right) \qquad (4.4)$$

where $E(t)$ represents the relaxation modulus, E_i and E_{∞} denote the relaxation coefficients and τ_i is the relaxation times.

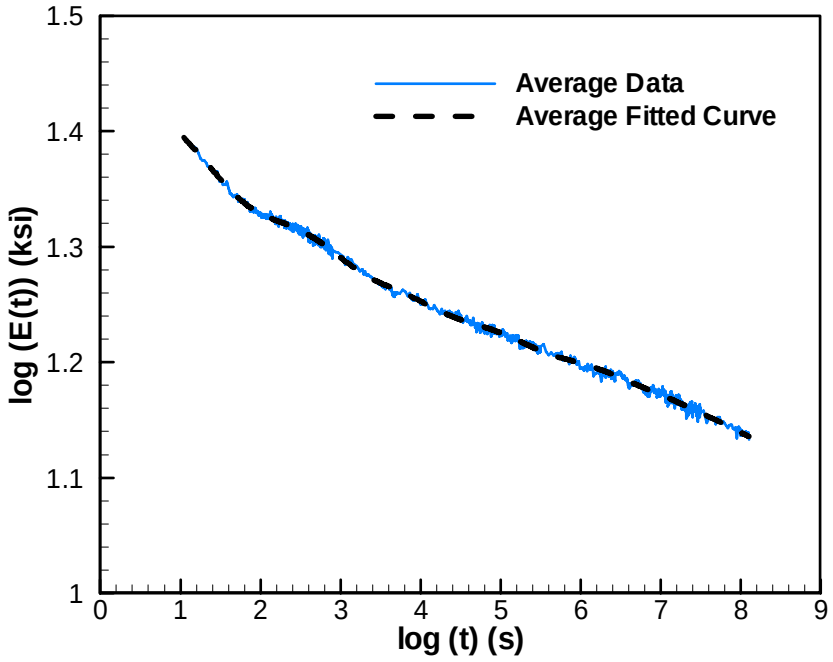

Figure 4.11 : In-plane relaxation master curve for 2.5 mil polyethylene web obtained by averaging both 1% and 3% in-plane relaxation master curves.

The average relaxation master curve begins at 24.8 ksi and ends at 14.4 ksi; thus the change in relaxation modulus over the period of 1 year is 41.9%. The fitted relaxation coefficients and relaxation times from *Prony Series* are shown in Table 4.5. The maximum error band for the average relaxation master curve is ±1.4%.

i	*Relaxation Coefficients* E_i *(ksi)*	Relaxation Times (s)
1	2.383	6.032
2	4.377	2.852×10^{1}
3	2.517	8.037×10^{2}
4	1.525	9.657×10^{3}
5	1.262	1.577×10^{5}
6	0.782	2.172×10^{6}
7	0.788	1.275×10^{7}
8	1.347	1.051×10^{8}
∞	13.2602	

Table 4.5 : Fitted relaxation coefficients and relaxation times of average in-plane relaxation master curve fitted by Prony Series.

4.2.3 Creep Compliance

Since the acquired in-plane relaxation material properties exhibit linear characteristics, the creep compliance properties can be determined from the relaxation function using the following expression,

$$\int_{0^+}^{t} E\left(t-\varsigma\right)\, J\left(\varsigma\right)\, d\varsigma \;=\; t \qquad (4.5)$$

where $E\left(t-\varsigma\right)$ represents the relaxation modulus and $J\left(\varsigma\right)$ is the creep compliance. A code was written in MatLab to perform the conversion based on equation (4.5) and Poisson's ratio is set to 0 since it is a unidirectional problem.

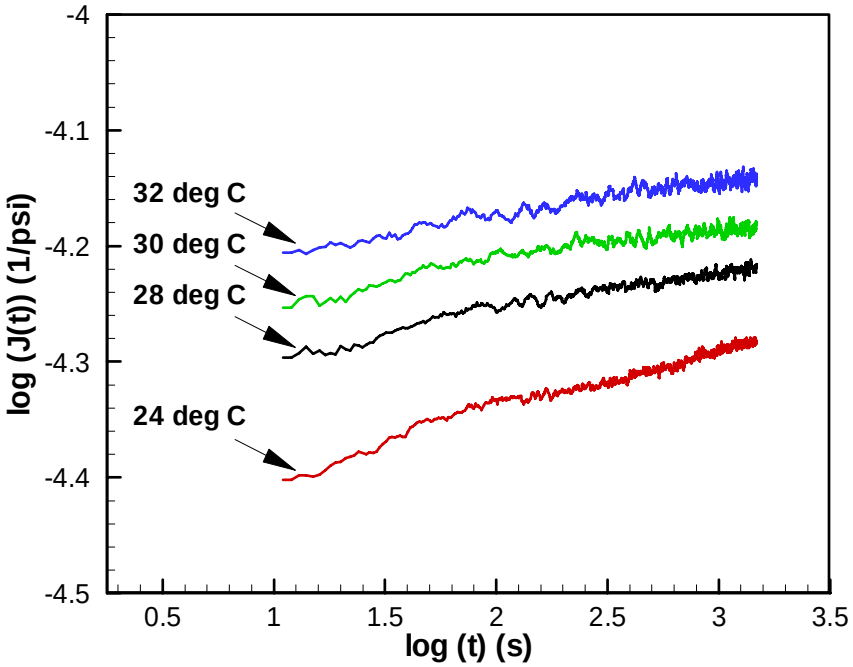

Figure 4.12 : In-plane creep compliance curves converted from in-plane 1% relaxation modulus (Figure 4.7) at different temperatures.

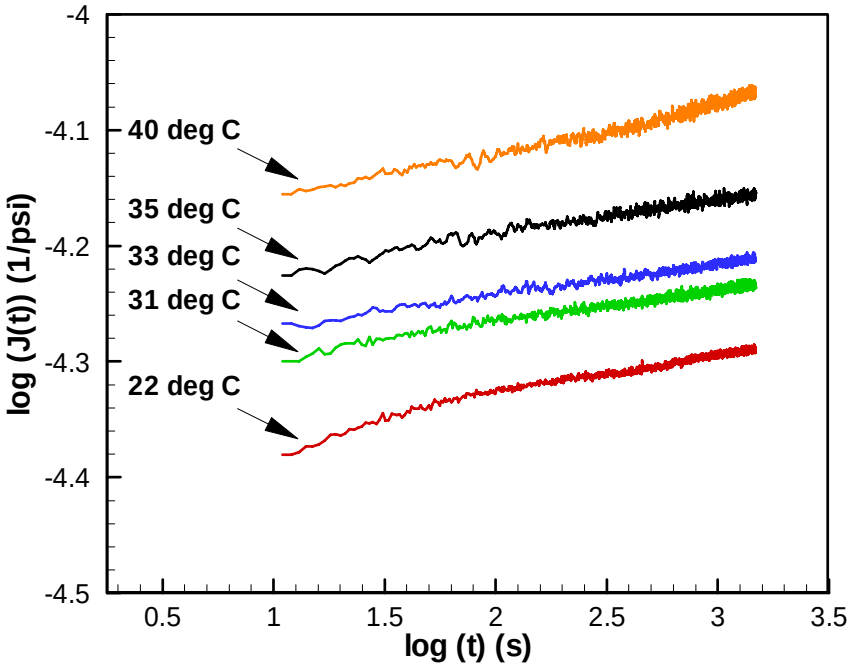

Figure 4.13 : In-plane creep compliance curves converted from in-plane 3% relaxation modulus (Figure 4.8) at different temperatures.

Using the code, the relaxation modulus curves in Figure 4.7 and Figure 4.8 were converted to creep compliance curves. The corresponding creep compliance curves are shown in Figure 4.12 and Figure 4.13 respectively.

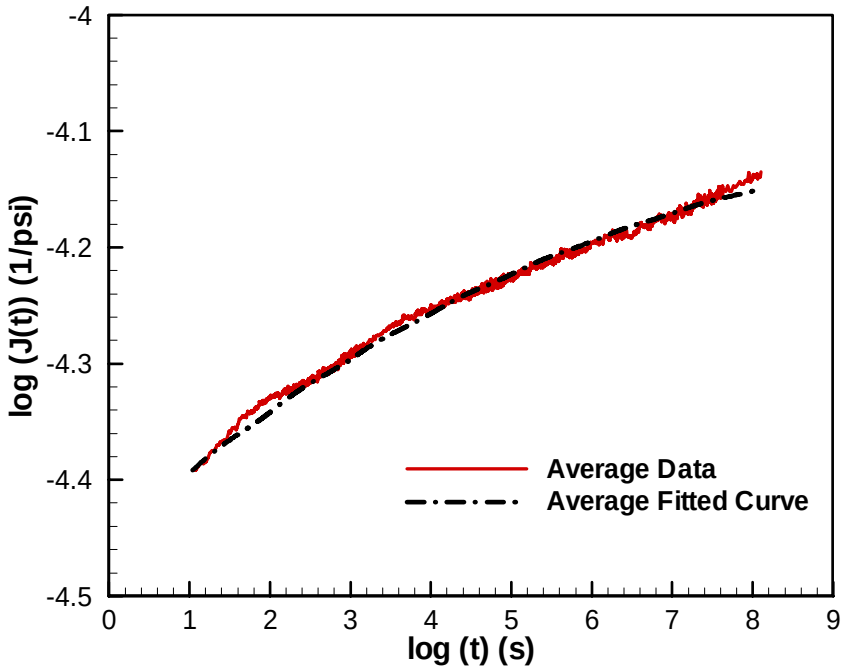

Figure 4.14 : In-plane creep compliance master curve for 2.5 mil polyethylene web obtained by averaging both 1% and 3% in-plane creep compliance master curves.

In view of the fact that in-plane relaxation master curves were linear, the in-plane creep compliance master curves should be linear. Time-temperature superposition was applied to Figure 4.12 and Figure 4.13; using room temperature as the reference temperature and same shift factors used in Table 4.3, to acquire the creep compliance master curves (long-term). The average creep compliance master curve is calculated and plotted in Figure 4.14.

i	*Creep Coefficients (1/psi)*	Retardation Times (s)
1	5.215 x 10 $^{-6}$	1.0 x 10 $^{-5}$
2	5.215 x 10 $^{-6}$	1.0 x 10 $^{-4}$
3	5.215 x 10 $^{-6}$	0.001
4	5.215 x 10 $^{-6}$	0.01
5	5.215 x 10 $^{-6}$	0.1
6	5.215 x 10 $^{-6}$	1
7	5.214 x 10 $^{-6}$	10
8	5.189 x 10 $^{-6}$	100
9	4.978 x 10 $^{-6}$	1000
10	4.740 x 10 $^{-6}$	1.0 x 10 ^{4}
11	4.396 x 10 $^{-6}$	1.0 x 10 ^{5}
12	3.898 x 10 $^{-6}$	1.0 x 10 ^{6}
13	3.605 x 10 $^{-6}$	1.0 x 10 ^{7}
14	3.192 x 10 $^{-6}$	1.0 x 10 ^{8}
0	5.215 x 10 $^{-6}$	

Table 4.6 : Fitted creep coefficients and retardation times of average in-plane creep compliance master curve using Prony Series.

The average creep compliance master curve was fitted using *Prony Series* as demonstrated in Figure 4.14 to determine the in-plane viscoelastic material properties characterization. The *Prony Series* used for creep compliance master curve is,

$$J(t) = J_0 + \sum_{i=1}^{n} J_i \left[1 - \exp\left(-\frac{t}{\varsigma_i} \right) \right] \qquad (4.6)$$

where $J(t)$ is the creep compliance at time t, J_0 and J_i represents the creep coefficients and ς_i are the retardation times. The fitted creep coefficients and retardation times obtained from *Prony Series* are shown in Table 4.6.

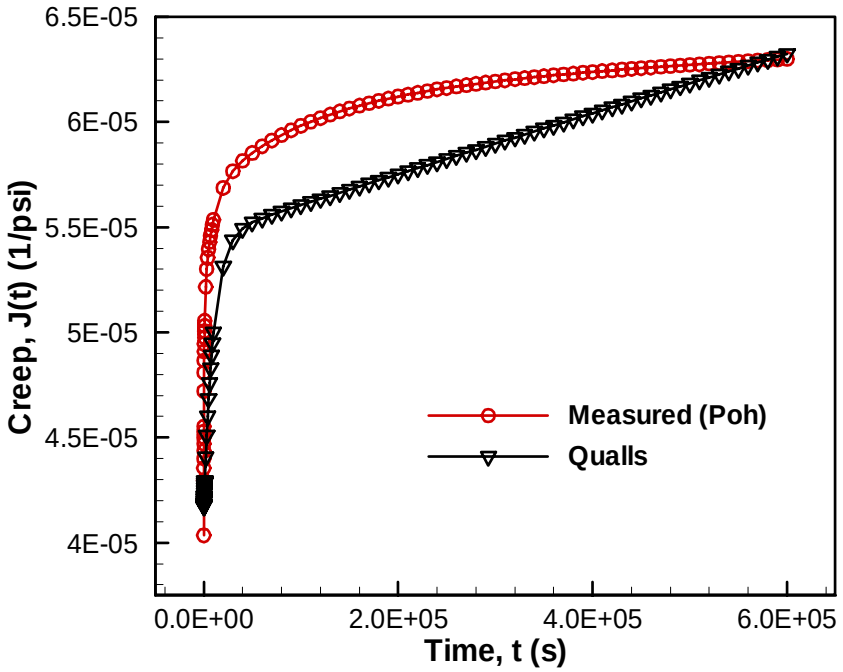

Figure 4.15 : Comparison of short-term (~ 7 days, Qualls' time duration of experiment) in-plane creep properties of polyethylene webs.

Lastly, creep coefficients and retardation times in Table 4.6, were validated by comparing against the short-term creep properties of polyethylene webs (approximately 7 days), previously measured by Qualls [69]. The verified results are displayed in Figure 4.15, whereas Table 4.7 indicates the similarities. As a reminder, the results obtained from this study distinctly differ from Qualls data, in terms of time scale. The creep coefficients and retardation times shown in Table 4.6 can be used, to determine the in-plane viscoelastic properties of

polyethylene webs for a year, whereas Qualls data can only predict the in-plane creep properties for a week.

Sources	References E_θ	In-Plane Creep (1/psi) from Figure 4.15		Avg. Difference
		$J_{t = 10\ s}$	$J_{t = 6E+5\ s}$	
Qualls [69]	E_θ = 24 ksi [i]	4.173 x 10^{-5}	6.3 x 10^{-5}	-
Experiment	Section 2.1.2 E_θ = 23 ksi	4.035 x 10^{-5}	6.325 x 10^{-5}	6.62%
Note: i. Qualls' Thesis Table 4.9 [69]				

Table 4.7 : Comparison between Qualls [69] data (measured for ~ 7 days) and experimental in-plane creep properties (after storing for 12 years from time of Qualls measurement).

4.3 Out-of-Plane Viscoelastic Material Properties

From Section 2.2.3 (Figure 2.9), it was estimated that typical radial strain on a perfectly wound polyethylene roll (web thickness of 2.5 mil) would be approximately 1% strain. Considering the addition of polyethylene inserts to create web bagginess (Section 3.1 & Section 3.3) on wound polyethylene roll and other winding contributions that were not considered in the modeling, it was estimated that the radial strain might increase to approximately 2% or 3% strain.

Therefore, a conservative approach was made to construct the out-of-plane relaxation master curve at 3% strain via compression method. Short-term relaxation experiments were performed at temperatures of 24^{o}C, 28^{o}C, 30^{o}C and 35.5^{o}C. The temperatures were selected to ensure each short-term relaxation

curve would overlap with its neighboring curves, so that they can be shifted horizontally to form a relaxation master curve. Experiments were also carried out at room temperature (24^{o}C) for 1% and 5% strain level.

Each test was conducted over a time period of 1600 seconds. Time-temperature superposition was employed to shift the data at different temperatures to form a master curve for one year, to predict the long-term relaxation behavior. The creep compliance master curve was also acquired by converting the relaxation data to creep compliance data and to allow the possibility of out-of-plane viscoelastic material property characterization assuming a linear inter-conversion relation.

4.3.1 Experimental Procedure

The experimental procedures are similar to the stack test described in Section 2.2.2 and the in-plane relaxation experiments in Section 4.2. Equipment used to execute the short-term relaxation experiments comprise of a hydraulic powered MTS 312 material test frame, a temperature chamber, a digital data acquisition system, a pair of compression platens, a type-K thermocouple with digital reader and a 55,000 lb load cell. The entire experimental setup can be viewed in Figure 4.16.

Stacks of polyethylene web (3”×3”×1”, *L*×*W*×*H*), with a web thickness of 0.0025 inches were used as the test samples, for the out-of-plane accelerated life-time testing. The height of each stack was measured using a digital caliper to ensure that each stack was precisely 1 inch in height and stored in separate

Ziploc® storage bags for identification. No annealing process was needed since the glass transition temperature, T_g of polyethylene sample is below room temperature (between -90^{o}C to -125^{o}C).

Figure 4.16 : The experimental setup used to conduct out-of-plane viscoelastic material property characterization.

The Instron FastTrack 8800 digital data acquisition system seen in Figure 4.17 with DAX FastTrack software package was used to collect the real-time load and time data when the experiment commences. This system allows digital calibration (semi-automatic) of the 55,000 lb load cell and to maintain data accuracy, calibration was performed before every test.

Figure 4.17 : The digital data acquisition system that was used to collect load and time data.

For each compression test, a stack of polyethylene web was placed in between the compression platen as demonstrated in Figure 4.18. Similarly with any stack test, edge effects of the sample were taken into consideration. A flat aluminum block (round stock) with a smaller surface area (2 inch diameter) than the polyethylene stack was used and placed on top of the test sample to remove the edge effects, as depicted in Figure 4.18(b). Alignment of the test stack with aluminum block at the top relative to the center of the compression platen was performed using visualization at different perspective angle.

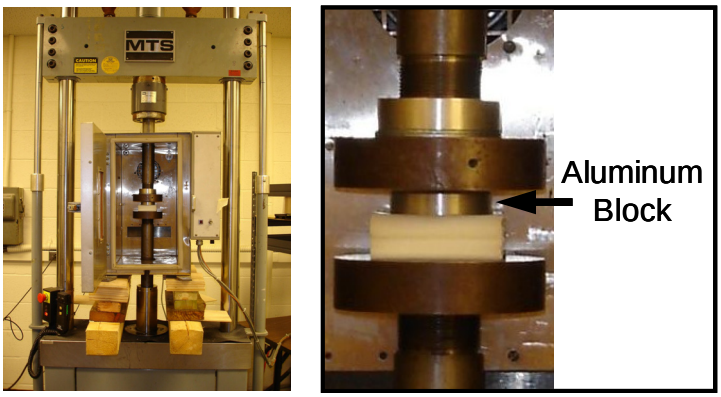

(a) (b)

Figure 4.18 : Prepared polyethylene stack in position to commence out-of-plane relaxation test (compression); (a) an overview of the sample relative to the entire test frame, (b) close-up view of the sample inside the temperature chamber.

After aligning the stack into position, the top platen was lowered to produce an initial compression load (pre-loading) of 3 lbs. Since cumulative height of both test stack and aluminum block was already known, the distance

between the upper and lower platen was checked with a digital caliper and compared; to ensure consistent data collection relative to the applied strain.

A thermocouple was then placed near the center of the test stack for temperature measurement and if required, heated to the pre-determined temperature. When the thermocouple reader indicates the correct temperature for testing within the chamber has been reached, the entire setup was left for another two hours to ensure thermal equilibrium.

Prior to actual testing, verification was made to measure the time duration for a stack of polyethylene web; (3”×3”×1”, *L*×*W*×*H*) with a web thickness of 0.0025 inches, to reach thermal equilibrium at 40^{o}C in the temperature chamber, using a thermocouple placed at the center of the stack. Results indicates that two hours were sufficient for the task, thus was used as standard thermal soak time for every test in the out-of-plane experiment at elevated temperatures.

Once the desired temperature condition has been reached, the stack sample was strained; via compression, to the desired strain level by applying strain that follows the ramp profile displayed in Figure 4.5. The experimental input parameters on the machine control interface (computer) for different strain levels are listed in Table 4.8. A rise time of 1 second was used throughout the out-of-plane accelerated life-time testing to preserve the consistency of all collected experimental data.

Load and time data were collected through a sampling rate of 10 Hz (10 data points per second) on the data acquisition system in the computer. Each test lasted 1600 seconds (approximately 27 minutes). When all relaxation

experiments (compression) were completed, the gathered data from each test were analyzed and plotted using *Tecplot* for visualization and characterization of out-of-plane viscoelastic material property.

Strain Rate (%)	Machine Displacement	
	Rate (in)	Speed (in/s)
1	-0.01	0.01
3	-0.03	0.03
5	-0.05	0.05

Table 4.8 : Input parameters for the machine control interface (computer) at different strain levels.

4.3.1.1 Out-of-Plane Repeatability Testing and Verification

Repeatability verification of out-of-plane relaxation experiment was accomplished by taking three identical out-of-plane relaxation data at room temperature and strain level conditions for comparison. The relaxation modulus results are plotted in Figure 4.19. The comparison of each experimental curve versus the calculated average shows that data were, in general, repeatable; since the maximum difference was 13.7%. Although the results may not be accurate but it was sufficient to be used as reference.

Repeatability can be improved by switching to a smaller load cell capacity on the hydraulic powered material test frame but caution should be taken from damaging the load cell since compression was applied instead of tension. To reduce the risk of load cell damage, an alternative test frame such as mechanical

or pneumatic powered systems should be used. By following these recommendations, the large variations among experimental curves can be reduced.

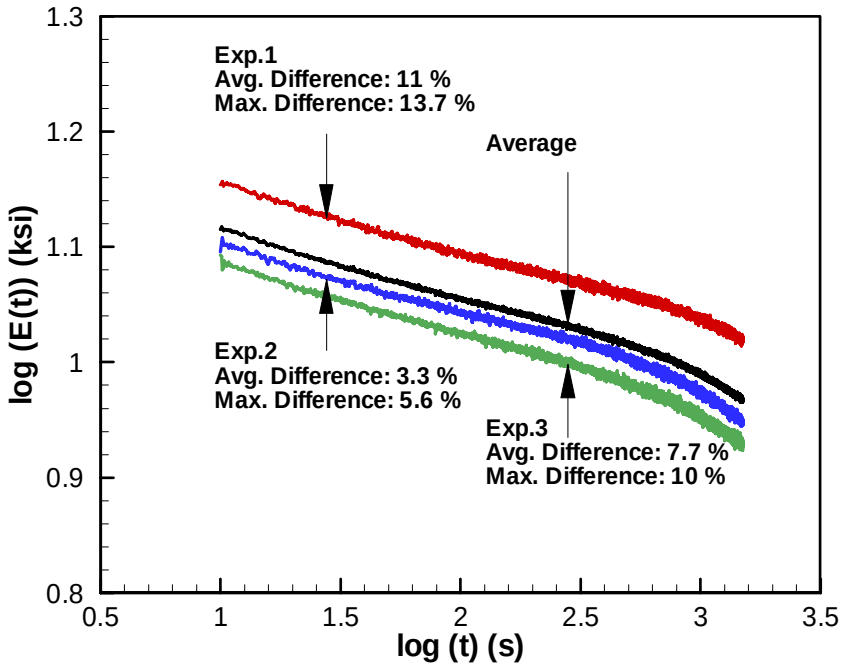

Figure 4.19 : Out-of-plane relaxation curves at 3% strain level and 24^{o}C with rise time of 1 second for verification of repeatability of the entire out-of-plane relaxation experiment.

4.3.1.2 Material Recycling

Since error rate from each test was quite high, as demonstrated in Figure 4.19; multiple tests were performed, instead of only three at different temperatures and its respective strain level. As a result, more polyethylene stacks were needed but supply was limited. Therefore, this issue needed to be resolved before the experiment could be completed.

Given that polyethylene material is a viscoelastic material hence it has inherent viscoelastic recovery characteristics. With these recovery characteristics in mind, it is possible for deformed polyethylene material to recover back to its original state, provided that the following conditions were met; (i) sufficient time was given for viscoelastic recovery, (ii) no stress or strain should be present in the material during its recovery period and (iii) the deformation experience by the material prior to recovery was not significant to the point of yielding.

In fact, these conclusions have already been proven through experimental results collected in Section 3.1.3 and Section 3.3.2. Furthermore, the rate of recovery depends on environmental temperature, thus it is possible to recycle the used polyethylene stacks. For verification, two new polyethylene stacks that have been compressed at 3% strain level, from relaxation tests at room temperature were identified, and placed into an environmental chamber, to be heated up to 37^{o}C for at least 5 days, to accelerate the viscoelastic material recovery rate.

The heating temperature of approximately 36^{o}C to 40^{o}C was determined based on the glass transition temperature, T_g, and melting temperature, T_m, of polyethylene web. Heating temperature lower than 36^{o}C, was too low for accelerated viscoelastic material recovery requirement (at least 5 days), whereas temperature higher than 40^{o}C will initiate the laminating process of polyethylene webs, which was undesirable.

After 5 days in the environmental chamber, the used stacks were gradually cooled to room temperature similar to annealing process. Once cooled,

the used stacks were retested under similar conditions and the results were compared in Figure 4.20.

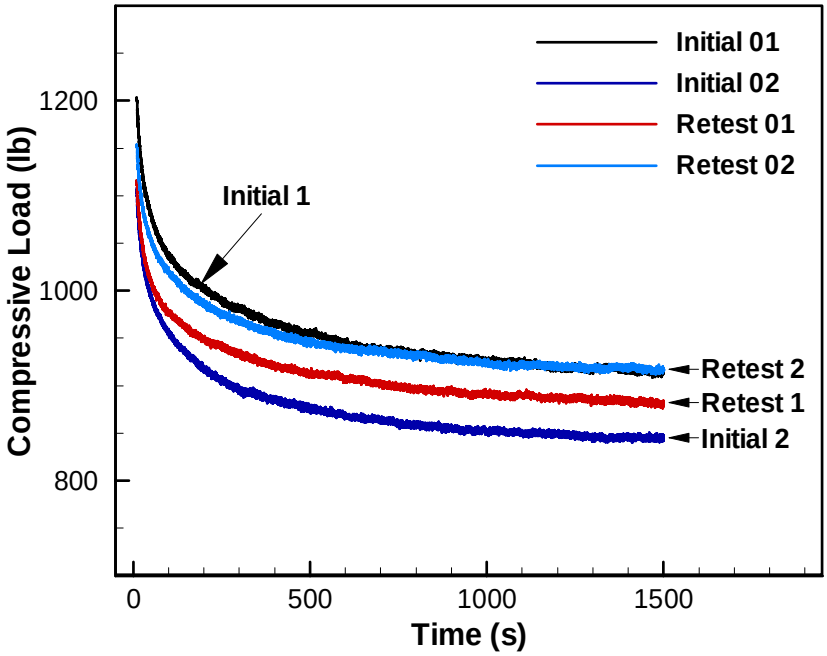

Figure 4.20 : Experimental verification of out-of-plane relaxation data for stack 1 and 2 at 3% strain level and 24^{o}C with rise time of 1 second, to prove that used polyethylene stacks can be reused after viscoelastic recovery.

Overall, the used polyethylene stacks showed viscoelastic recovery characteristics. Stack # 1 did recover to some degree, whereas stack # 2, the recovered results were higher than the initial results. These fluctuating results (does not overlap), especially for stack # 2, can be attributed to experimental setup and equipment used.

In summary, the used polyethylene stacks can be reused for out-of-plane relaxation test (compression) in this application because of viscoelastic recovery characteristics. Therefore, some of the out-of-plane relaxation data used in the

out-of-plane viscoelastic material property characterization was acquired from reused polyethylene stacks; that were recycled in the environmental chamber at approximately 36^{o}C to 40^{o}C for at least 5 days.

4.3.2 Relaxation Modulus

All out-of-plane relaxation experimental data were converted to relaxation modulus by applying equation (4.3) and the relaxation curves are plotted using Tecplot for visualization. Since numerous tests were completed for each temperature zone at their respective strain levels, the plotted relaxation curves correspond to the averaged values among those tests for its respective condition. The relaxation modulus for 3% strain level at different temperatures is displayed in Figure 4.21. Relaxation modulus for 1%, 3% and 5% strain level at room temperature are plotted together in Figure 4.22 for comparison and linearity verification.

There are several comments that can be stated from both Figure 4.21 and Figure 4.22. (1) The relaxation modulus decreases as time and temperature increases, thus displaying similar characteristics as the in-plane relaxation results. (2) All plotted curves have the initial data point starting at t_1 = 10 seconds, while omitting the first 10 seconds of experimental data; to account for the differences between ramp and step loading at the initial stage, and to maintain consistency throughout the experiment. (3) Results from Figure 4.22 suggest that out-of-plane viscoelastic material property behavior (polyethylene roll in the radial direction) to be non-linear.

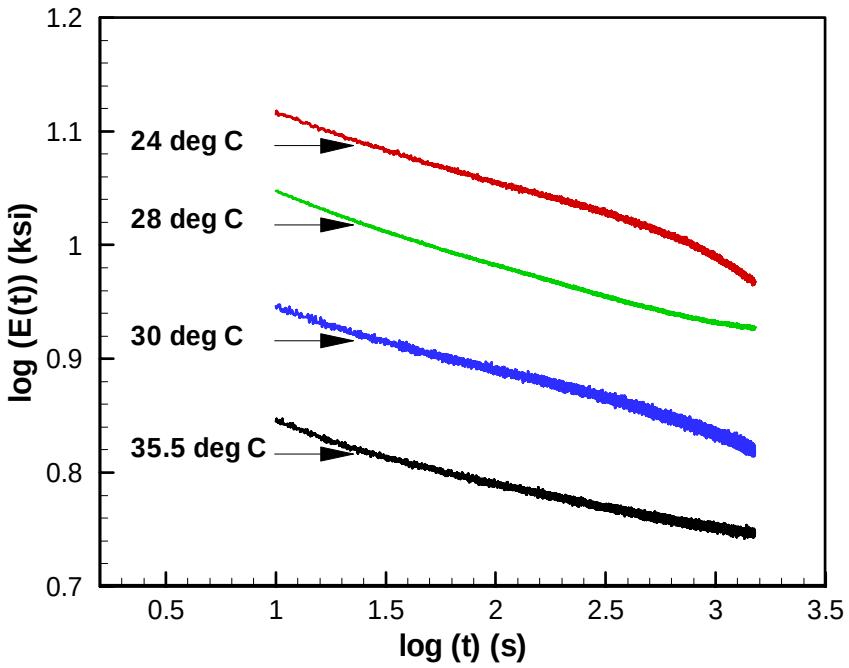

Figure 4.21 : Out-of-plane relaxation modulus curves at different temperatures for 2.5 mil polyethylene web at 3% strain level.

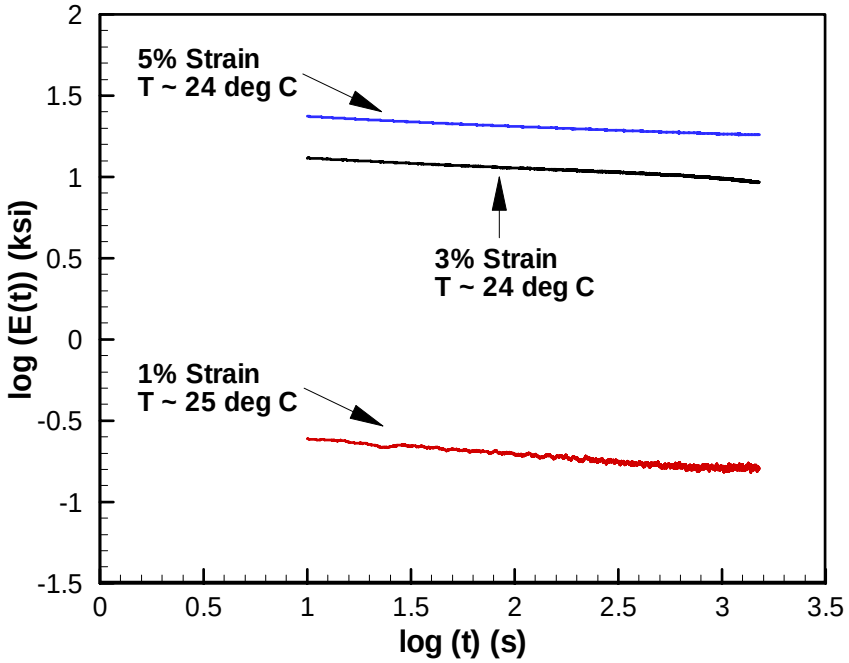

Figure 4.22 : Comparison between 1%, 3% and 5% strain level of out-of-plane relaxation modulus curves for 2.5 mil polyethylene web at room temperature.

Time-temperature superposition was applied to obtain the relaxation master curve (long-term) for 3% strain level. Individual curves at different temperatures were shifted horizontally using room temperature as reference temperature to construct the relaxation master curve. The relaxation master curve is shown in Figure 4.23 and the shift factors used to move the relaxation curve at different temperatures to create the master curve is tabulated in Table 4.9 and plotted in Figure 4.24. For 3% strain level, the relaxation master curve begins at 13 ksi and ends at 5.8 ksi; hence the change in relaxation modulus over the period of 1 year is 55.4%.

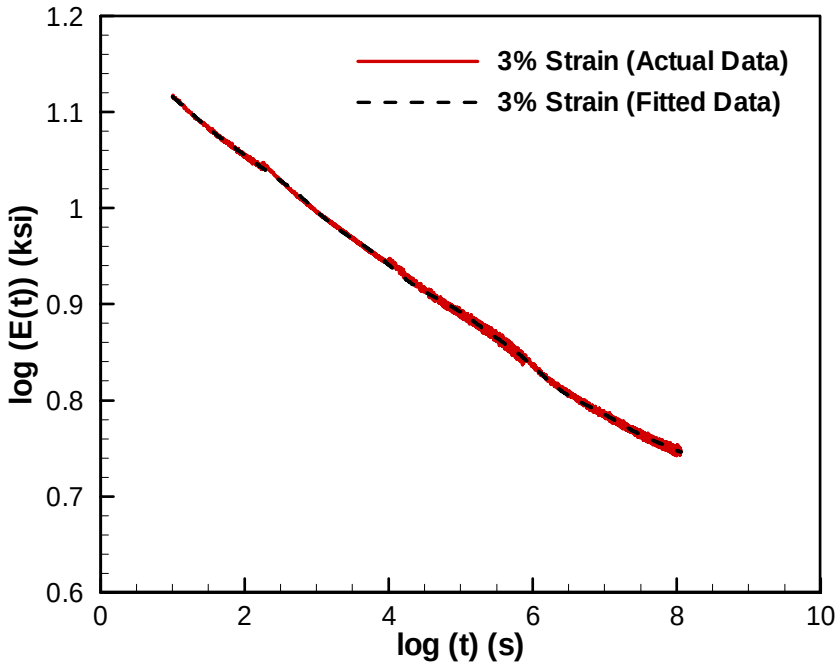

Figure 4.23 : Out-of-plane relaxation master curve for 2.5 mil polyethylene web at 3% strain level.

Strain (%)	Shift Factors at Various Temperatures (s)			
3	24 deg. C	26 deg. C	30 deg. C	35.5 deg. C
	0	1.25	3	4.875

Table 4.9 : Log_{10} shift factors (in seconds) used to determine 3% strain level relaxation master curve (out-of-plane).

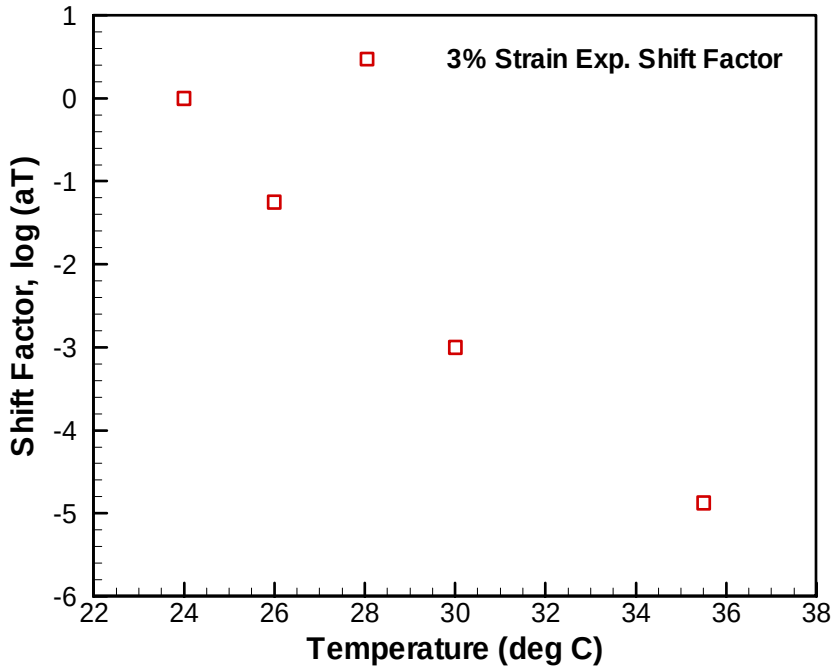

Figure 4.24 : Shift factors used to determine 3% strain level relaxation master curve (out-of-plane) at room temperature.

The relaxation modulus master curve was fitted using Prony Series similar to equation (4.4). In fact, the fitted curve can be viewed in Figure 4.23 whereas the fitted relaxation coefficients and relaxation times are shown in Table 4.10.

i	*Relaxation Coefficients* E_i *(ksi)*	Relaxation Times (s)
1	1.707	1.337×10^{1}
2	1.129	7.532×10^{1}
3	1.591	7.096×10^{2}
4	1.301	8.954×10^{3}
5	7.801×10^{-1}	1.023×10^{5}
6	1.126	1.020×10^{6}
7	5.784×10^{-1}	1.147×10^{7}
8	4.994×10^{-1}	1.031×10^{8}
∞	5.406	

Table 4.10 : Relaxation coefficients and relaxation times for out-of-plane relaxation master curve at 3% strain level fitted by Prony Series.

4.3.3 Creep Compliance

Creep compliance properties for 3% strain level condition at room temperature will now be computed from out-of-plane relaxation data using the linear inter-conversion equation (4.5). It should be noted that this linear inter-conversion relation cannot be applied to nonlinear viscoelastic behavior. Nevertheless, it still provides an estimate for creep compliance to be used for future reference.

Using the same code mentioned in Section 4.2.3 and the same Poisson's ratio, the short-term creep compliance for 3% strain level condition at different temperatures were converted and plotted in Figure 4.25. Similarly, relaxation modulus for 1% and 5% strain level, at room temperature were also converted

and plotted together with 3% strain level, at room temperature in Figure 4.26, to demonstrate the non-linear behavior in terms of creep compliance.

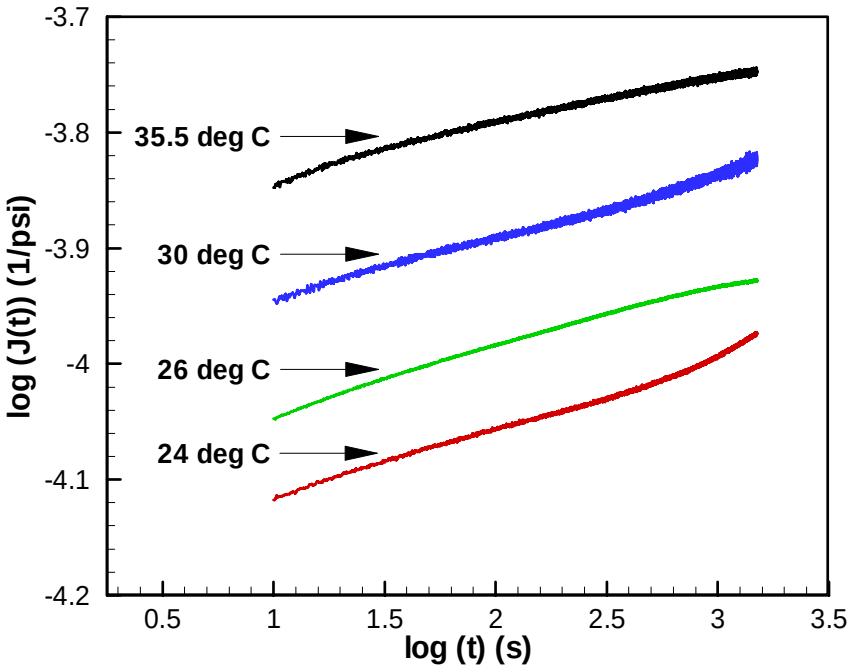

Figure 4.25 : Out-of-plane creep compliance curves converted from out-of-plane 3% relaxation modulus (Figure 4.21).

The time-temperature superposition technique was applied onto the short-term creep compliance curves at different temperatures; using room temperature as the reference temperature and identical shift factors listed in Table 4.9. As a result, the creep compliance master curve was constructed in Figure 4.27.

Creep compliance master curve was also fitted using Prony Series similar to equation (4.6), to establish the out-of-plane viscoelastic material properties for 3% strain level. The results of the fitted curve (3% strain level condition) is plotted in Figure 4.27, whereas the fitted creep coefficients and retardation times for 3% strain level condition obtained from Prony Series are tabulated in Table 4.11.

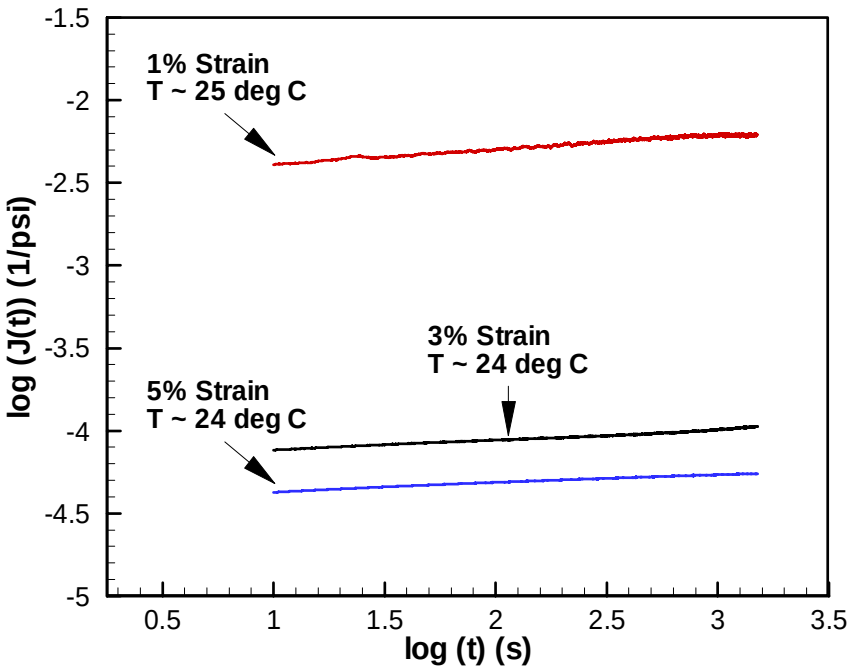

Figure 4.26 : Out-of-plane creep compliance curves converted from 1%, 3% and 5% relaxation modulus for 2.5 mil polyethylene web at room temperature.

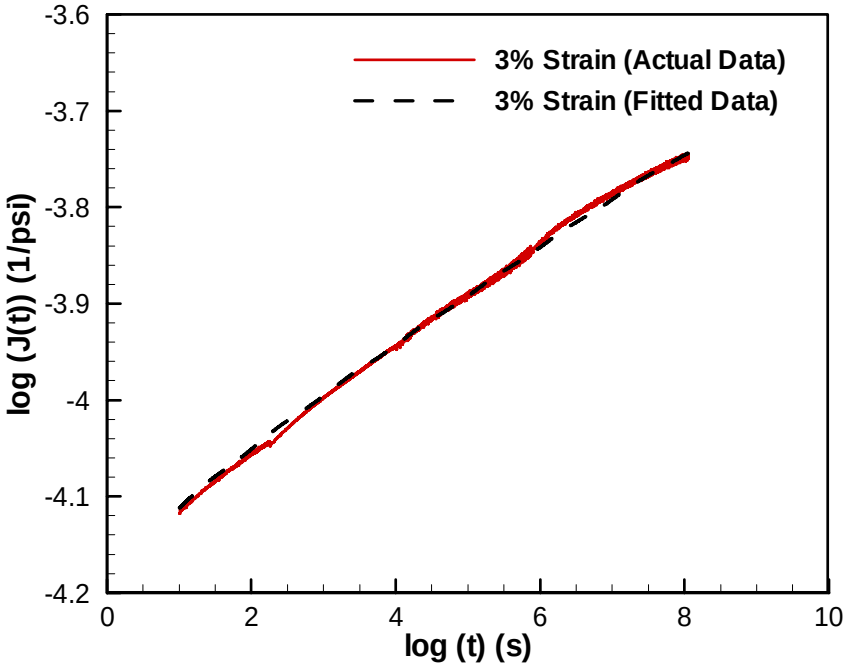

Figure 4.27 : Out-of-plane creep compliance master curve for 2.5 mil polyethylene web at room temperature (24^{o}C), constructed from Figure 4.25.

i	*Creep Coefficients (1/psi)*	Retardation Times (s)
1	1.146×10^{-5}	1.0×10^{-4}
2	1.146×10^{-5}	0.001
3	1.146×10^{-5}	0.01
4	1.146×10^{-5}	0.1
5	1.146×10^{-5}	1
6	1.147×10^{-5}	10
7	1.169×10^{-5}	100
8	1.211×10^{-5}	1000
9	1.33×10^{-5}	1.0×10^{4}
10	1.436×10^{-5}	1.0×10^{5}
11	1.64×10^{-5}	1.0×10^{6}
12	1.786×10^{-5}	1.0×10^{7}
13	2.145×10^{-5}	1.0×10^{8}
0	1.146×10^{-5}	

Table 4.11 : Creep coefficients and retardation times of out-of-plane creep compliance master curve fitted by Prony Series.

In Qualls' thesis [69], Qualls performed creep compliance measurement directly on the polyethylene webs whereas in this study, the data collected was relaxation data. Due to the nonlinear out-of-plane characteristics of polyethylene webs, it will be unjust to use the converted out-of-plane creep compliance data (estimated from linear inter-conversion relation) in this study as a comparison to Qualls data. It should be noted that although the initial relaxation behavior may be similar but the creep compliance characteristics may have changed over the

time span of 12 years from aging effect and pro-longed roll pressure (crystalline phase). As the result, only 3% strain divided by pressure over time (~ 7 days), from measured data, will be plotted in Figure 4.28 for future reference.

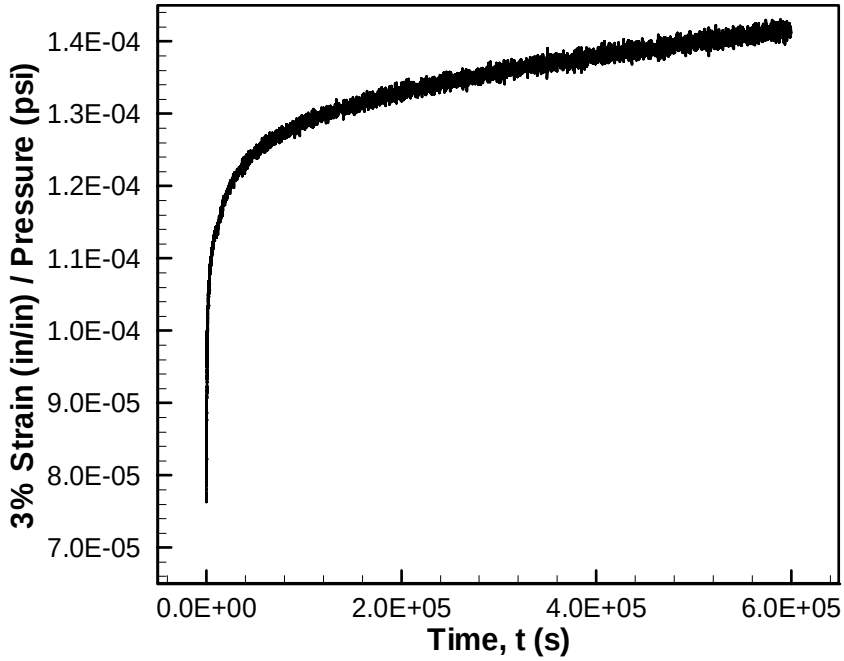

Figure 4.28 : Plot of 3% strain divided by pressure over time (~ 7 days), from measured data for future reference.

4.4 Chapter Summary

In-plane and out-of-plane relaxation experiments were carried out to investigate the long-term viscoelastic material properties of polyethylene web, in par with the objective, to obtain both relaxation and creep material properties characterization for polyethylene web at typical winding conditions. Hence, in-plane relaxation modulus at 1% and 3% strain levels, and out-of-plane relaxation modulus at 3% strain level were acquired to cover the duration of 1 year at room

temperature. Attempts were also made to obtain out-of-plane relaxation modulus at 1% and 5% strain levels at room temperature for linearity verification.

Time-temperature superposition principle was utilized to accelerate the characterization of viscoelastic material properties. Results obtained from the relaxation master curves indicate that the tangential direction (in-plane property) of wound polyethylene roll to be linear whereas the radial direction (out-of-plane property) of the roll to be non-linear. It should be noted that further tests in the area of creep compliance and relaxation at different strain levels need to be carried out for radial direction (out-of-plane) of the roll, to obtain a complete set of viscoelastic material properties characterization of polyethylene webs.

The in-plane relaxation master curves at 1% and 3% strain levels were linear, hence the average relaxation master curve was used and the change in relaxation modulus can be observed in Table 4.12. On the other hand, out-of-plane relaxation master curve at 3% strain level was only available; so the change in relaxation modulus for this case was listed in Table 4.13.

Time	Relaxation Modulus (ksi)	Change over time (%)
11 seconds	24.8	-
1 hour	18.4	25.9
1 day	16.8	32.1
1 month (30 days)	15.4	38
1 year (365.25 days)	14.4	41.9

Table 4.12 : 2.5 mil polyethylene web in-plane behavior at room temperature within 1% to 3% strain range.

Time	Relaxation Modulus (ksi)	Change over time (%)
10 seconds	13	-
1 hour	9.2	29.2
1 day	7.8	40
1 month (30 days)	6.5	50.2
1 year (365.25 days)	5.8	55.4

Table 4.13 : 2.5 mil polyethylene web out-of-plane behavior at room temperature under 3% strain.

CHAPTER 5

NON-CONTACT DIGITAL SURFACE IMAGING OF BAGGY WEB

This chapter will investigate the prospect of using a pair of cameras to detect web bagginess; specifically baggy lanes. The discussion focuses on the application of two codes and utilizes photogrammetric method since it allows concurrent measurement of multiple points real-time in web handling applications. Further more, this method have the advantage of accuracy, reliability, scalability and the capacity to store collected data for further analysis and post-processing.

5.1 Camera Calibration

The use of cameras for mapping purposes has come a long way as pointed out by Clarke [13], and are commonly used in scientific research, especially in the measurement of three-dimension and two-dimension objects. Before captured images can generate useful information in three-dimensional computer vision, the images will have to be converted and to accomplish this task, cameras will have to be calibrated.

Nonetheless, distortions or errors are unintentionally introduced due to the physical limitations of the camera itself. To remove these unwanted errors, many models and techniques have been developed for this purpose; especially Brown

[7,8,22] who has made significant contribution in this area. Typical calibration techniques that can be utilized are *photogrammetric calibration* [5,77,97], *self-calibration* [30,53,55] and *line-based calibration* [83] to name a few. In this study, the code used to perform camera calibration, will be based on the photogrammetric calibration method.

Photogrammetric calibration method is conducted by observing a planar pattern of known geometry in three-dimensional space at a few different orientations. The technique requires either the camera or the planar pattern to be able to move freely during the calibration process, while the other stays in a fixed position. One advantage to be gained from this method is the ease of producing the planar pattern; by using a laser printer, a simple and low cost chessboard pattern should be sufficient for the purpose.

Self-calibration method, in contrast, does not require a calibration object. Instead, the calibration is performed by moving a camera in a static scene, where the rigidity of the scene is sufficient to determine the constraints needed by the camera's internal parameters from the image displacement information.

Line-based calibration on the other hand relies only on the assumption where the straight lines in the three-dimensional world must project to straight lines in the image plane. Consequently, if the user locates a curve line in the image where it should have been a straight line in the three-dimensional world, the algorithm will seek to find the distortion parameter of that line that causes it to be curved in the image. Although this calibration method does not rely on

calibration pattern or other camera parameters, it does require a scene containing straight lines.

5.1.1 Coordinate Systems and Definitions

It is important to understand the fundamental coordinate systems used in digital imaging, since computers do not see the three-dimensional world like a human does. Thus, several steps will have to be taken to convert one coordinate system to another and ultimately producing a three-dimensional image on screen. Figure 5.1 summarizes these steps; in addition, there are two important variables in camera calibration process which are known as *intrinsic* and *extrinsic parameters* [14,33,87,97].

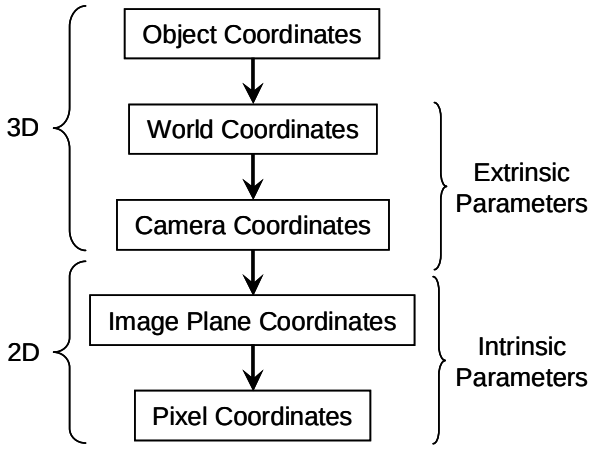

Figure 5.1 : Different coordinate systems involved in a digital imaging process.

Extrinsic parameters are external parameters which define the location of the camera with respect to the object in three-dimensional space. In other words it transforms the coordinates of the object into a coordinate frame that is camera

centered and it plays an important role when there exists a multi-camera system because it also describes the relationship between these cameras. Examples of extrinsic parameters are; *translational position* and *angular position* of the camera in the Cartesian coordinate (x, y, z) frame.

Intrinsic parameters on the other hand, are parameters that are innate to the camera itself and are not affected by external circumstances. Examples of intrinsic parameters are; *focal length*, *principal point*, *skew coefficient* and *lens distortion (radial and tangential distortions) parameter*.

Focal length is essentially the distance between the optical center of the lens to the image sensor of the camera when the lens is focused on infinity and it determines the angle of view and size of the object within the image. In physical sense if we increase the focal length, it means that we are reducing the angle of view however we are enhancing or magnifying the image of the object.

Principal point is the point of intersect between the lens surface plane where the projection of entering and exiting ray intersects and the optical axis of the camera lens.

Skew Coefficients define the angle between the x and y pixels on the image sensor. *Lens distortion* refers to the radial and tangential distortions of the image captured from the object by the camera.

5.1.2 Pinhole Camera Model

The camera model in this chapter uses the *Pinhole Camera Model*, where the model is based on the *Principle of Collinearity*. An illustration in Figure 5.2

describes this model, where every point observed by the camera is projected via imaginary straight lines through the projection center into the image plane of the camera.

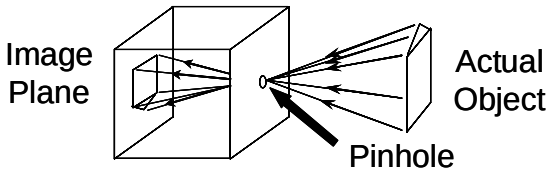

Figure 5.2 : Illustration of *Pinhole Camera Model*.

This model takes arbitrary points in three-dimensional space and converts them to camera coordinates using a transformation matrix that takes translation and rotation of each point into account; then, the points are normalized into the image plane [33]. In most literatures, the image coordinate system is defined to be on the upper left corner of the image array [33].

To account for inaccuracies that affect the real camera projection, two types of distortions were considered, which are the *radial lens distortions* and *tangential lens distortions* [4,33]. The extended model is expressed in the form of,

$$\begin{bmatrix} u_i \\ v_i \end{bmatrix} = \begin{bmatrix} D_u s_u \left(\tilde{u}_i + \delta u_i^{(r)} + \delta u_i^{(t)} \right) \\ D_v \left(\tilde{v}_i + \delta v_i^{(r)} + \delta v_i^{(t)} \right) \end{bmatrix} + \begin{bmatrix} u_o \\ v_o \end{bmatrix} \tag{5.1}$$

where D_u and D_v represents the conversion coefficients (from metric units to pixels), s_u signify the scaling factor, (u_o, v_o) is defined as the principal point, while $(\tilde{u}_i, \tilde{v}_i)$ is the normalized projection in the image plane, $\left(\delta u_i^{(r)}, \delta v_i^{(r)} \right)$

corresponds to the radial lens distortions and $\left(\delta u_i^{(t)}, \delta v_i^{(t)} \right)$ is the tangential lens distortions [33].

The radial lens distortion causes the actual image point to be displaced radially in the image plane [77]. While the tangential lens distortions occurs, when there is imperfect centering of the lens components within the camera [33], and may also include other manufacturing defects in the lens [4]. In some literature, it is sometimes referred to as *decentering distortion* and has both a radial and tangential component in it [33,77].

In summary, both Heikkilä and Bouguet [4,33] identify this extended model to be the *intrinsic camera model*. Note that each intrinsic parameter $\left(f, s_u, u_o, v_o \right)$ and the distortion coefficients have a certain significant physical representation of the camera. In addition, the development of this *intrinsic camera model* has the assumption that the calibration procedure uses a three-dimensional target with known geometry in its image observation.

5.1.3 Camera Calibration Toolbox

Some authors have generously made their camera calibration codes available through their websites in the internet [4,32,97]. The camera calibration toolbox employed in this study originates from Bouguet [4] and it requires *MatLab* to operate.

In Bouguet's code [4], the main initialization phase of the code was motivated from Zhang's work [97] whereas Zhang's *initial estimation of planar homographies* and *maximum likelihood estimation* were identical. Bouguet [4]

uses the *orthogonality of vanishing points* [10,42] in solving for the closed–form solution of the unknown parameters. Lastly, the *intrinsic camera model* used by Bouguet [4] is very similar to the paper presented by Heikkilä [33].

5.2 Digital Image Correlation (DIC) Method

Digital Image Correlation [9,52,63,80,82], or *DIC*; is a widely accepted technique of measuring displacements and displacement gradients in material under deformation. This non-contact method of measurement has been used at different temperatures for both rigid and soft materials. DIC can measure both infinitesimal and large deformations. The technique originally proposed by a group of researchers from University of South Carolina has been refined by others [11,45,49,88-91], while several have proved its reliability through a wide number of applications [25,35,62,93].

Vendroux and Knauss [49,88-91] proposed an algorithm to refine the existing algorithm in four areas: (i) a least square correlation coefficient was used; (ii) an approximate Hessian matrix was used; (iii) a bi-cubic spline surface was used to interpolate the image grayscale values; (iv) large deformation theory with the consideration of the Lagrangian strain tensor, Φ and rigid body rotation, θ in the material was used.

Lu and Cary [11,45] extended the two-dimensional large deformation method by incorporating a second order approximation into the algorithm and implementing an incremental correlation procedure. Initially, the algorithm utilizes a subset around the location of interest to determine the translation and

deformation gradients of that location; however, if nonlinear deformation occurs, the linearity of the displacement gradient diminishes due to the presence of second-order deformations. Therefore, with the introduction of the second order approximation, yielding 13 mapping parameters prevents the higher order gradients from obscuring the strain component that only depends on the first order partial derivatives. The method allows better convergence to produce better accuracy under large deformations; as compared to the previous algorithm where only 7 parameters were used.

Following the work by Lu and Cary, Ganesan [24] included the third-order displacement mapping for non-linear deformation with 23 mapping parameters. Preliminary results indicate an improvement in infinitesimal strain measurement compared to the first and second-order algorithms, but problems occurred when measuring deformations near a crack because the algorithm was unable to converge near the crack tip. On the same note, both Sutton [81] and Knauss [38] reported similar problems in areas around cracks in their respective research work.

Periasamy [62] made an attempt to surmount this difficulty by allowing the algorithm to first identify the crack edge position, employing the connected component labeling technique, then taking into consideration the presence of the crack in deformation measurement during computation. As the image correlation progresses, the nodes around the crack region were discarded by the displacement computation. Validation results of this proposed method conducted

by Periasamy shows that the new algorithm was able to detect the specimen deformation values near crack tip.

5.2.1 WinDIC Software

A proprietary digital image correlation software developed by Lu et al. [11,45,62], called WinDIC_LS (Version 2.0) is used to determine the two-dimensional image coordinates for both left and right cameras. The software compares a reference image with a deformed image, to measure the changes in displacement that occur between both images, hence producing the deformation field. In order for the software to function properly, a *grayscale pattern* is needed on the location of interest for all images to be used for the procedure. Typically, a grayscale pattern consists of different shades of gray with varying light intensity; as in black as the weakest intensity to white as the strongest intensity and usually stored in the form of 8-bit images in computer imaging. Speckle patterns illustrated in Figure 5.3 are examples that are generally used for digital image correlation method.

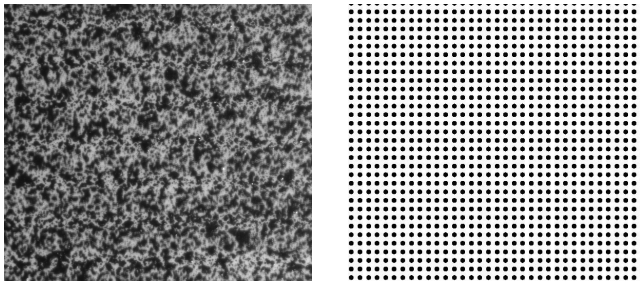

(a) (b)

Figure 5.3 : Examples of grayscale speckle patterns for projection onto a web: (a) random pattern, (b) grid pattern.

5.3 Merging Camera Calibration Toolbox with WinDIC

This section will address the entire imaging analysis procedures that was used in this study. Two software programs, *Camera Calibration Toolbox for MatLab* by Dr. Jean-Yves Bouguet [4] and *WinDIC* developed by Dr. Hongbing Lu at Oklahoma State University [11,24,45,62], were utilized in combination, to obtain the three-dimensional surface profile of an object such as a baggy web using two cameras. An overview of the procedures is given in Figure 5.4 while a detail description on each section can be found in Appendix A.

5.4 Surface Profile

The idea of non-contact digital surface profiling using two cameras will now be evaluated using polyethylene webs. Three experiments will be discussed where the first will be a validation of the idea using simulated web bagginess, second will be the detection of actual specific web bagginess and the last will be on the testing of the accuracy of the system.

5.4.1 Non-Contact Imaging of Simulated Baggy Lane

The aim of this experiment is to verify the non-contact digital surface profiling idea to acquire three-dimensional surface profile of baggy lanes for certain baggy web using a simulated baggy web.

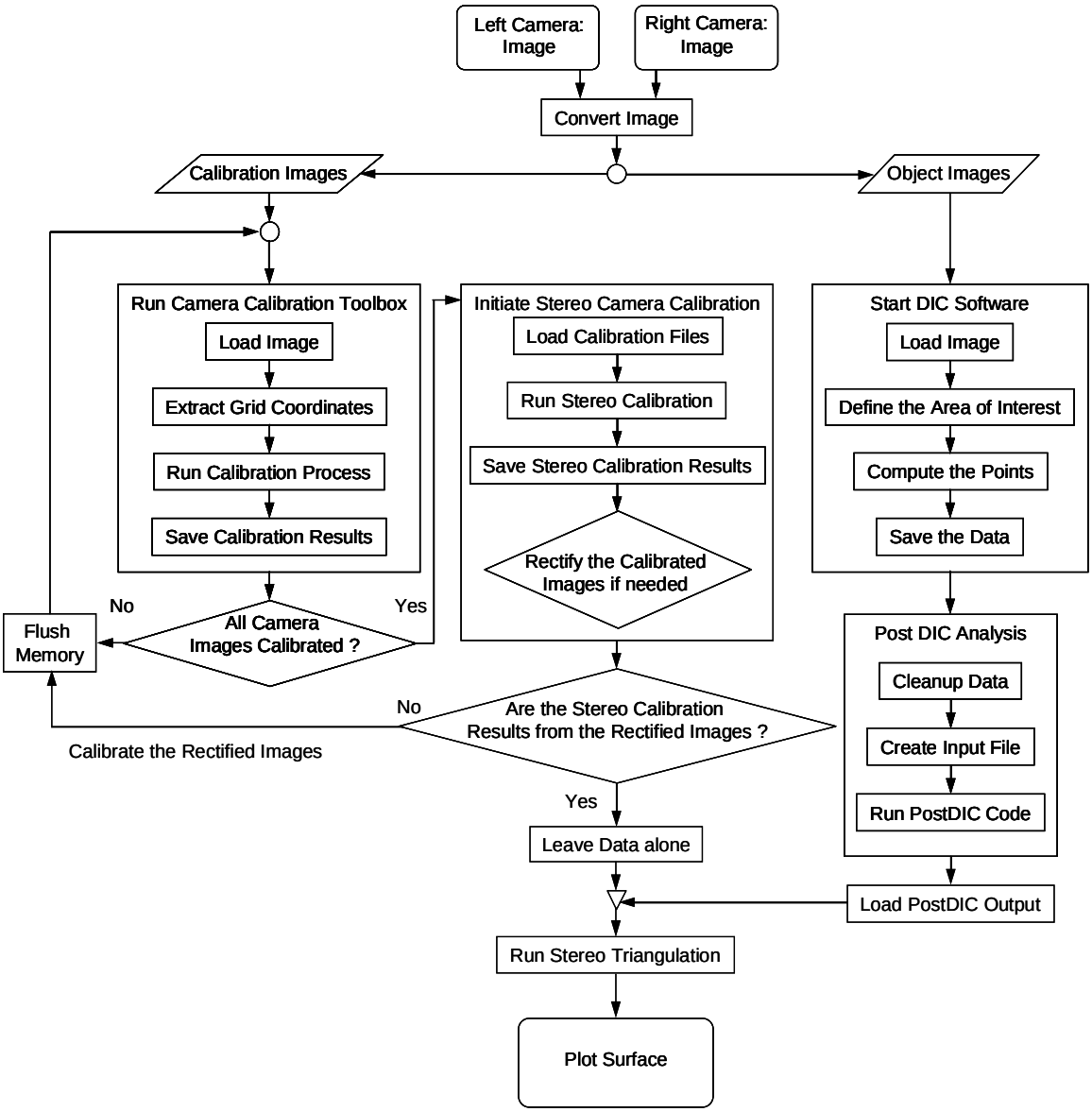

Figure 5.4 : Flowchart of the entire procedures used to obtain the three-dimensional surface profile of baggy lanes.

5.4.1.1 Experimental Procedure

The equipment used in this experiment consisted of two digital cameras (Kodak Model: CX6230; 2 Mega-pixels, and Kodak Model: DC215; 1 Mega-

pixels), a digital projector, two camera tripods and a portable notebook computer for downloading images and analysis. The equipments set up is shown in Figure 5.5. The distance between the simulated baggy web and the cameras was approximately 1.6 meters, while both cameras were positioned 0.3 meters apart.

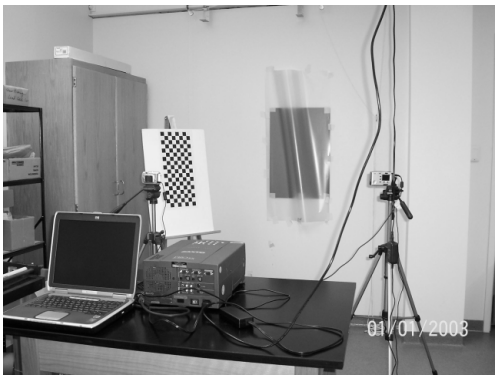

Figure 5.5 : Experimental setup used for the simulated baggy web.

The web material used to simulate the baggy web; represented by a *bump*, was an 18 inches wide Tyvek® paper approximately 3 feet in length, as shown in Figure 5.6. A chessboard pattern with a grid size of 240 x 540 mm^2 was used for calibration purposes and the size of each square in the grid is 30 x 30 mm^2, as demonstrated in Figure 5.6.

A total of 50 calibration images at different orientations were captured (25 images each for left and right camera; acquired in pairs) during the image acquisition process. Depending on the experimental setup, the number of calibration images taken during each experiment may vary. Also, the quality of the calibration results depends on the number of calibration images taken at different orientations hence, a higher number of calibration images will yield better calibration results.

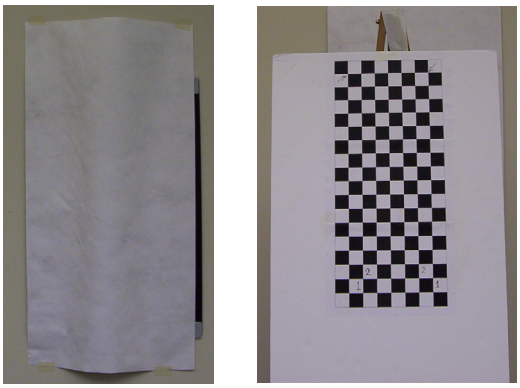

(a) (b)

Figure 5.6 : (a) The Tyvek® paper used to simulate the baggy web with a *bump* in the middle. (b) The chessboard calibration pattern glued to a foam board for rigidity used in the experiment. A poster stand is used to support the foam board when the calibration patterns are moved at different orientation during the experiment.

Although a pair of object images is needed to find the pixel coordinates of the baggy web, additional object images will help, in case some pairs are severely distorted or poorly focused. Five pairs of object images were taken in this experiment, by both left and right cameras.

During the image acquisition process, the flash mode on the cameras was turned off to prevent any unwanted light interference that could hinder the camera calibration process. Also, caution was taken to prevent any dislocation of the tripods, where the cameras were mounted, from their original position once the experiment commenced. This is done in order to avoid any unnecessary errors that could cause the disruption of the camera calibration process at the later stage.

When projecting speckles onto the web material with a digital projector, the lights in the room were turned off. A reduction in the environmental light source, other than the digital projector, helps the cameras to capture higher quality speckle images. Thus, the experiments were commonly carried out at night. Figure 5.7 illustrates the view of the object observed by each camera.

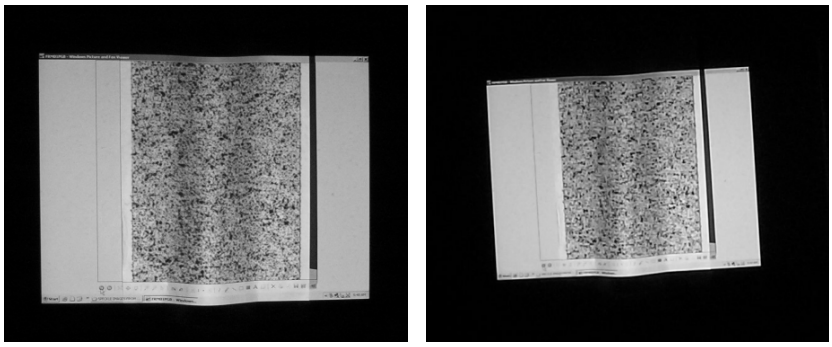

(a) (b)

Figure 5.7 : (a) The left camera viewpoint of the Tyvek® paper and, (b) the right camera viewpoint when the speckles are projected onto the simulated baggy web.

5.4.1.2 Surface Profile

Once the image acquisition procedure had been completed, all images were uploaded into the computer for conversion to *tiff* format in grayscale. All images were also resized to 800 × 600 resolutions for consistency. WinDIC were used to obtain the pixel coordinates of the *bump* using 150 nodes (25 x 6 nodes) with 5 x 5 spacings.

Images captured by both cameras with chessboard pattern were used as calibration images and Dr. Bouguet's Camera Calibration Toolbox for MatLab

was used to perform the calibration computation. The rectified intrinsic parameters, including the distortions after the stereo camera calibration result, for the left camera are given in Table 5.1. The results for the right camera are given in Table 5.2.

	x	y	± x error	± y error
Focal Length	630.72996	630.60981	3.19218	3.10154
Principal Point	304.39681	282.36437	2.52701	2.81126
Skew Coefficient	0.0		0.0	

Distortion			Tolerance (±)
Radial	k_1	0.00886	0.00926
	k_2	-0.01262	0.01572
	k_3	0.0	0.0
Tangential	p_1	-0.00006	0.00124
	p_2	-0.00033	0.00167

Table 5.1: Left camera rectified intrinsic parameters including the distortions after stereo camera calibration for Experiment 1.

The rectified extrinsic parameter results (position of right camera with respect to the left camera) after stereo camera calibration are,

Rotation vector:

om = [0.00001 0.00198 0.00004] ± [0.00502 0.00442 0.00070]

Translation vector:

T = [-313.74035 -0.05879 -0.26115] ± [0.35971 0.26873 1.70718]

	x	y	± x error	± y error
Focal Length	630.48921	630.39514	3.13116	3.11309
Principal Point	338.30817	282.38690	2.53762	3.37450
Skew Coefficient	0.0		0.0	

Distortion			Tolerance (±)
Radial	k_1	0.00268	0.01395
	k_2	-0.00910	0.06328
	k_3	0.0	0.0
Tangential	p_1	0.00028	0.00187
	p_2	0.00012	0.00124

Table 5.2 : Right camera rectified intrinsic parameters including the distortions after stereo camera calibration for Experiment 1.

Finally, the surface profile obtained from the analysis can be observed in Figure 5.8 whereas the positions of the calibration grid plotted in camera reference frame can be seen in Figure 5.9.

Although the shape of the plotted surface profile in Figure 5.8 looks similar to the actual *bump*, but the height of the plotted *bump* is actually smaller than the actual. This error can be attributed to the size of each square used in the grid. For better characterization of the actual surface profile, higher grid resolution is needed, which means smaller size squares.

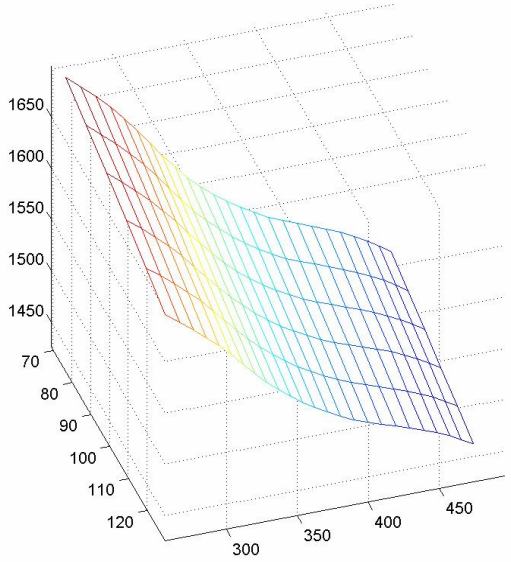

Figure 5.8 : Surface profile of the simulated baggy web using Tyvek® paper.

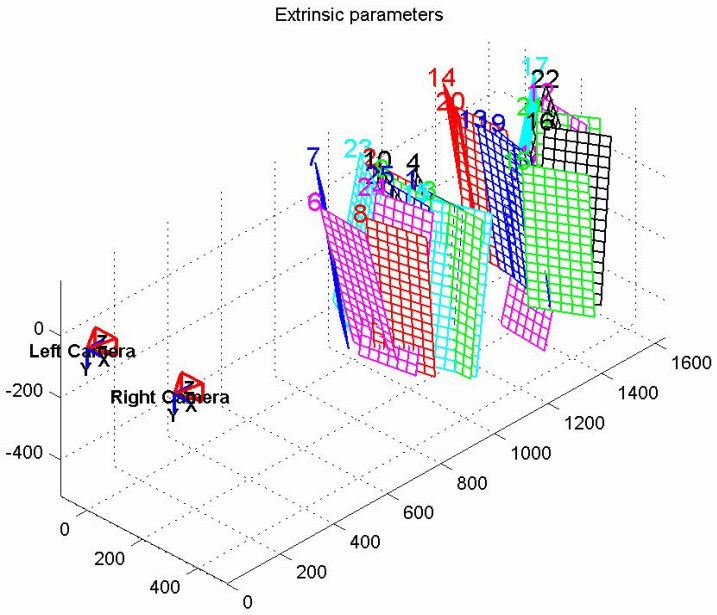

Figure 5.9 : Positions of the calibration grid plotted in camera reference frame for Experiment 1.

5.4.2 Non-Contact Imaging of an Actual Baggy Lane

In this experiment, a polyethylene web with actual baggy lanes created during winding is evaluated, to obtain the three-dimensional surface profile using the proposed non-contact method.

5.4.2.1 Experimental Procedure

Equipment used in this experiment consists of two identical digital cameras (Sony Model: DSC-P100 Cyber-shot; 5 Mega-pixels), an Infocus digital projector, two camera tripods and a computer for storing images, and analysis. The cameras were positioned in the following way as indicated in Figure 5.10 with respect to the object. A beam leveler was used to ensure that both tripods and cameras were at the same elevation. The distance between the object and the cameras was approximately 0.5 meters while both cameras were roughly 0.2 meters apart.

To be consistent throughout the entire study of baggy lanes, a 6 inch wide polyethylene web with 1 inch wide baggy lanes was used as shown in Figure 5.11. The baggy lanes were created during winding and the details in creating this type of baggy lanes has been described previously in Section 3.3. It should be noted that transparent polyethylene web does not reflect projected speckles from digital projector very well, causing the object images to become hazy. Thus, to achieve greater clarity of the projected speckles on the baggy web, this issue needs to be resolved.

Figure 5.10 : Experimental setup used for the polyethylene web with real baggy lanes.

Several methods have been tested, the initial results does not show any promise. Some products were found to react with the polyethylene web causing irregular surface tension due to the sudden drop in temperature of the web when the paint was applied, while others tend to peel-off when the polyethylene web was unwound. Eventually, a solution was found by applying a thin coating of white colored aerosol paint (*Krylon Fusion for Plastics*) onto an area of the web during winding, and left within the wound roll for several days until it was time to conduct the experiment. The results can be observed in Figure 5.11.

Similar to the previous experiment, a chessboard pattern was used for calibration. In this experiment, the grid size is 60 × 80 mm^2, as demonstrated in Figure 5.11; while the size of each square in the grid has been reduced to 5 × 5 mm^2 for improve accuracy.

Overall, 84 calibration images at different orientations were collected (42 images each for left and right camera; acquired in pairs) during the image acquisition process to produce better calibration results. Precautions discussed

in the earlier experiment were followed, to avoid any possibility for errors that could cause the termination of the camera calibration process at the later stage. The experiment was carried out at night and the lights in the room were turned off, when photographing the object; to ensure the projected speckles from the digital projector would show up clearly in the camera. The flash mode of the camera was disabled throughout the entire experiment with the similar purpose of reducing the environmental light source. Figure 5.12 exemplifies the view of the object observed by each camera in this experiment.

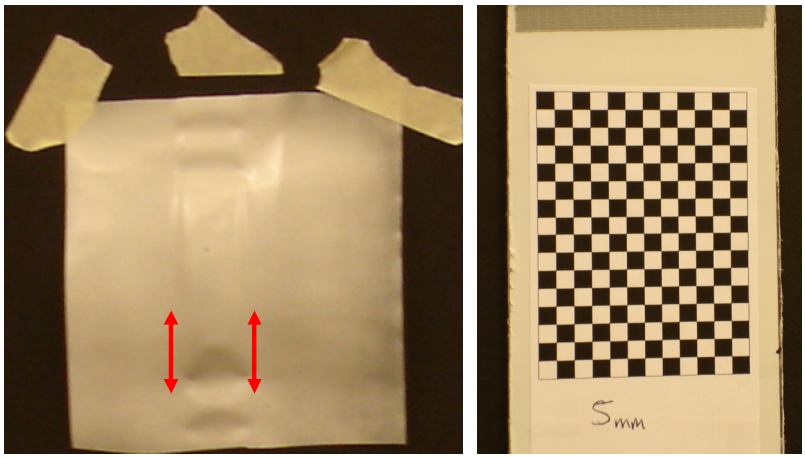

(a) (b)

Figure 5.11 : (a) Coated 6 inches wide polyethylene web with real baggy lanes created during winding. The arrows indicate the location of the baggy lanes that transverse across the web in the MD-direction. (b) Higher resolution calibration pattern glued to a piece of polycarbonate for rigidity. Note that, both images are not scaled relative to one another.

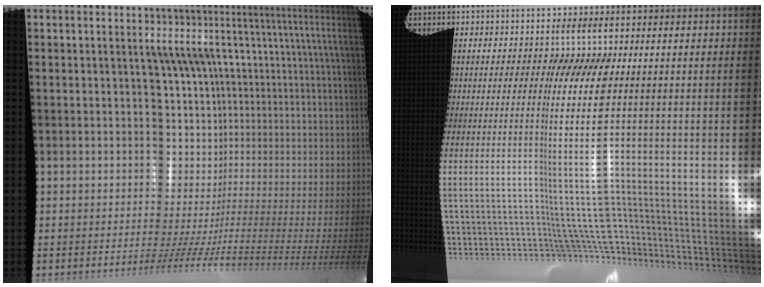

(a) (b)

Figure 5.12 : Camera viewpoints of the polyethylene web: (a) left camera and, (b) right camera, when speckles are projected onto the baggy web via a digital projector.

5.4.2.2 Surface Profile

The images uploaded into the computer were converted to *tiff* format in grayscale and resized to 640 × 480 resolutions. WinDIC nodes were set to 30 × 6 with 6 × 6 spacing for this experiment, to compute the pixel coordinates of the object image while Dr. Bouguet's Camera Calibration Toolbox for MatLab was used to perform the camera calibration.

Results of the left camera rectified intrinsic parameter including the distortions after stereo camera calibration are in Table 5.3 while the results for the right camera are noted in Table 5.4.

The rectified extrinsic parameter results (position of right camera with respect to the left camera) after stereo camera calibration are,

Rotation vector:

om = [0.02355 -0.00296 -0.00382] ± [0.01814 0.01934 0.00194]

Translation vector:

T = [-239.12357 0.12737 0.12672] ± [0.53681 0.29930 3.56205]

	x	y	± x error	± y error
Focal Length	1984.42281	1999.15672	17.55710	9.59344
Principal Point	-61.60840	186.34599	28.52285	30.08530
Skew Coefficient	0.0		0.0	

Distortion			Tolerance (±)
Radial	k_1	-0.13101	0.07552
	k_2	0.30181	0.21761
	k_3	0.0	0.0
Tangential	p_1	-0.00739	0.00368
	p_2	0.01838	0.01250

Table 5.3 : Left camera rectified intrinsic parameters including the distortions after stereo camera calibration for Experiment 2.

Lastly, the surface profile obtained from the analysis can be observed in Figure 5.13, whereas the positions of the calibration grid plotted in camera reference frame can be seen in Figure 5.14. The plotted surface profile is similar to the actual profile of the baggy polyethylene web, as shown in Figure 3.19. Improvements to this result can be attributed to the reduction of the size of each square in the grid and the distance between the cameras and the object yielding better quality images.

	x	y	± x error	± y error
Focal Length	2011.00352	2005.37767	23.54263	10.43819
Principal Point	743.79092	234.12323	28.85966	19.71870
Skew Coefficient	0.0		0.0	

Distortion			Tolerance (±)
Radial	k_1	0.05717	0.08478
	k_2	-0.14807	0.15717
	k_3	0.0	0.0
Tangential	p_1	-0.00128	0.00252
	p_2	0.00786	0.01682

Table 5.4 : Right camera rectified intrinsic parameters including the distortions after stereo camera calibration for Experiment 2.

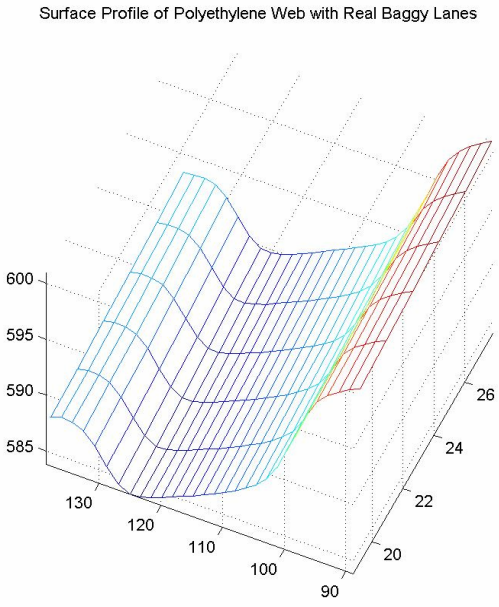

Figure 5.13 : Surface profile of polyethylene web with real baggy lanes created during winding.

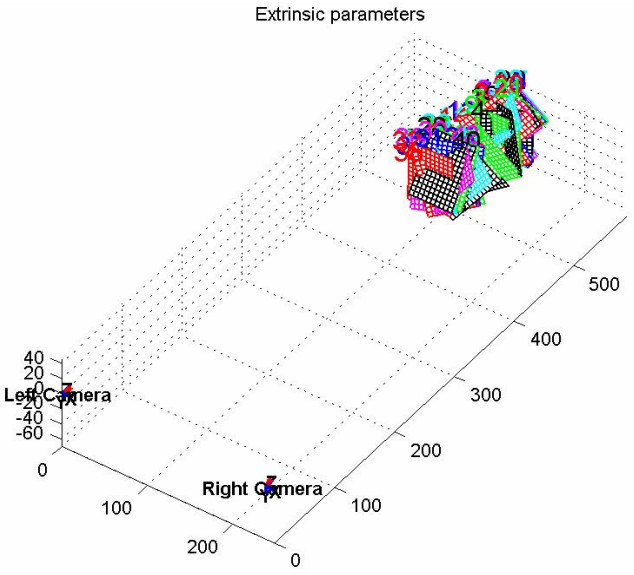

Figure 5.14 : Positions of the calibration grid plotted in camera reference frame for Experiment 2.

5.4.3 System Accuracy

This experiment addresses the accuracy via z-axis displacements and errors of the camera calibration method, as supporting evidence to show that the non-contact digital surface profiling method has the potential to acquire three-dimensional surface profile of baggy lanes.

5.4.3.1 Experimental Procedure

Equipment used in this experiment consisted of two digital cameras with their respective tripods, *Melles-Griot* uniaxial translation and rotational stage, a block of aluminum and a computer for storage and analysis. The distance

between the rotation stage and the cameras was approximately 0.8 meters, while both cameras were roughly 0.2 meters apart.

To perform the experiment, a chessboard pattern with the grid size of 210 × 210 mm^2 was used; and the size of each square in the grid was 30 × 30 mm^2. The pattern was glued to a board to hold the pattern upright then taped to a solid aluminum block, and placed perpendicular to the z-plane direction on the *Melles-Griot* rotation stage as shown in Figure 5.15.

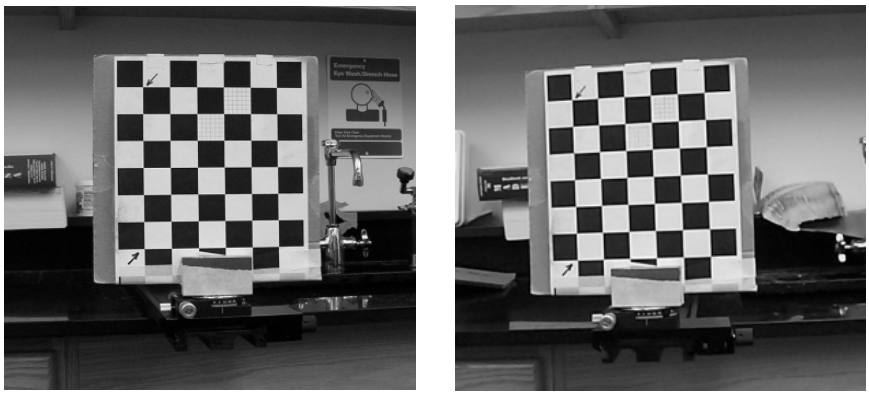

(a) (b)

Figure 5.15 : Sample viewpoint of chessboard pattern placed on top of a *Melles-Griot* uniaxial translation and rotational stage observed by (a) left camera, (b) right camera, during experiment.

The *Melles-Griot* uniaxial translation stage was used primarily to displace the grid, by some known distances in the z-plane direction. These actual displacement values will be compared to the predicted values computed by the camera calibration toolbox for accuracy.

A total of 28 calibration images at different rotation angles were captured (14 images each for left and right camera; acquired in pairs) during the image acquisition process. This was followed by an additional 12 images (6 images each), taken at different z-plane locations for accuracy measurement. Figure 5.15 represents a sample viewpoint observed by both cameras in the experiment.

It should be noted that most of the precautions and steps discussed by earlier experiments were followed in this experiment to maintain an accurate measurement.

5.4.3.2 Error Analysis

All images were uploaded into the computer for conversion to *tiff* format in grayscale and resized into two different sets of resolution; 640 × 480 and 1632 × 1232 resolutions respectively. There are several reasons for doing so, mainly to determine how resolutions will affect the accuracy and to check the stability of the camera calibration toolbox when using higher resolution images.

Computation using Dr. Bouguet's Camera Calibration Toolbox for MatLab was performed on the set of images with 640 × 480 resolutions first. The size of a pixel at this resolution was 1.2 mm and was obtained using the following equation,

$$pixel\ size = \frac{(\ length\ of\ the\ side\ of\ a\ square\ )}{(\ number\ of\ pixels\ on\ that\ side\ )} \qquad (5.2)$$

Once the calibration results were obtained for this set, the origin of the chessboard pattern selected during grid corner extraction process was used as the *target point*.

A target object usually consists of multiple points to form the shape of an object when the *stereo triangulation* subroutine is called, but in this experiment, only a point was needed specifically the z-coordinate of that point; so, in this context, we define that point as a *target point* for convenience. The origin of the chessboard pattern selected during the grid corner extraction process was used as the *target point* and the location remained fixed throughout the entire experiment.

Once the calibration results were obtained for this set of images, the pixel coordinates for the additional images taken during the experiment were extracted manually. Then, each pair of pixel coordinates was triangulated using the calibration results to acquire the z-plane displacement. The displacements were then compared to the actual displacement of the *Melles-Griot* uniaxial translation stage to ascertain the accuracy and error of the method.

The analysis was repeated for 1632 × 1232 resolutions images and the rectified version of 640 × 480 resolution images. Finally, the results from analysis for both unrectified and rectified versions of 640 × 480 resolution images can be viewed in Figure 5.16 and Figure 5.17 respectively, while the unrectified version of 1632 × 1232 resolutions images can be found in Figure 5.18.

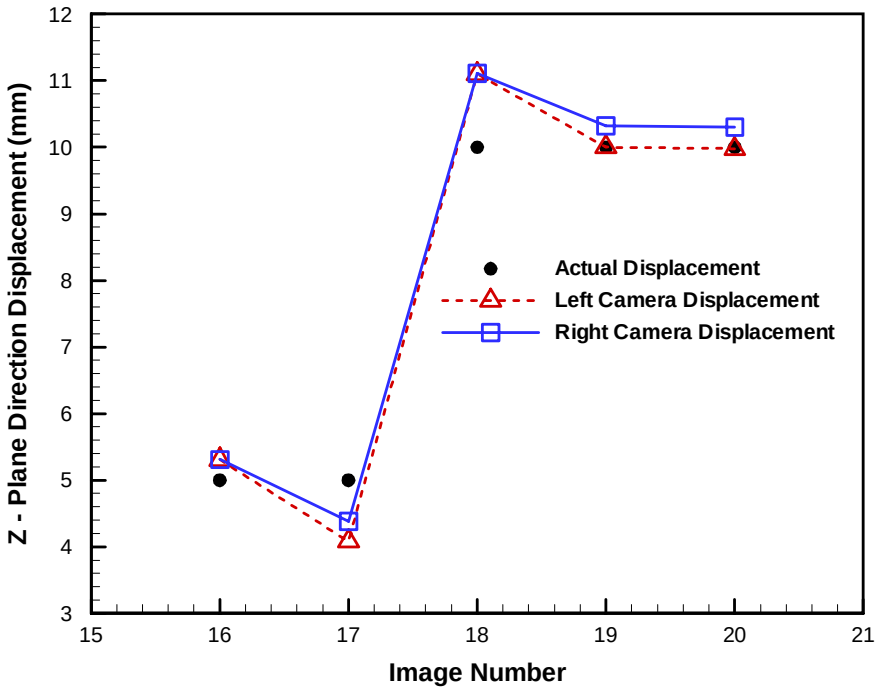

Figure 5.16 : Comparison of results for camera displacement versus actual displacement for unrectified 640 × 480 resolution images.

Although rectified results from 640 × 480 resolutions (Figure 5.17), do not fall close to the actual displacement data as compared to the unrectified results (Figure 5.16), the rectified curve is smoother than the unrectified curve. This can be explained from the *'smoothing'* process of the data points when the images were corrected for distortions, as compared to the unrectified irregular fluctuating characteristics.

As expected, results from the unrectified higher resolution images (Figure 5.18) do yield better accuracy except for the inability of the Camera Calibration Toolbox to rectify high resolution images, due to memory management problems

in *MatLab*. Several attempts were made to resolve this issue but all resulting in failure.

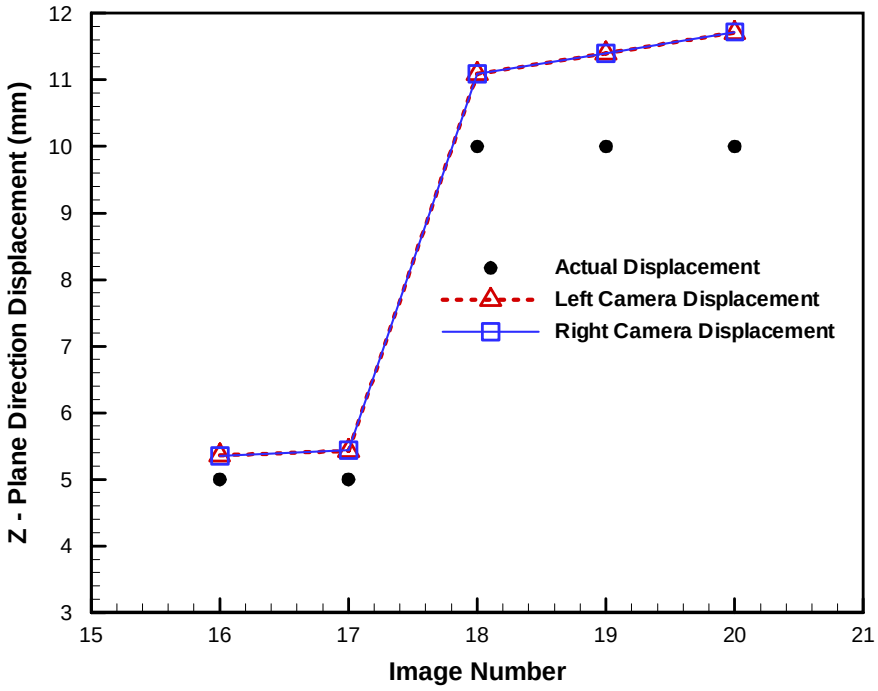

Figure 5.17 : Comparison of results for camera displacement versus actual displacement for rectified 640 × 480 resolution images.

Overall, the maximum error average calculated for both unrectified and rectified 640 x 480 resolutions results are no more than ±1 mm. Even though additional tests and computation will have to be conducted, with no less than 30 more arbitrary points for a statistically conclusive answer, it is plausible to utilize the proposed method to detect certain cases of baggy lanes, considering that 1 mm is approximately 0.04 inch. In fact, additional improvements to the camera calibration toolbox in terms of memory management and utilizing high resolution cameras, it will no doubt allow the proposed method to detect even thinner webs.

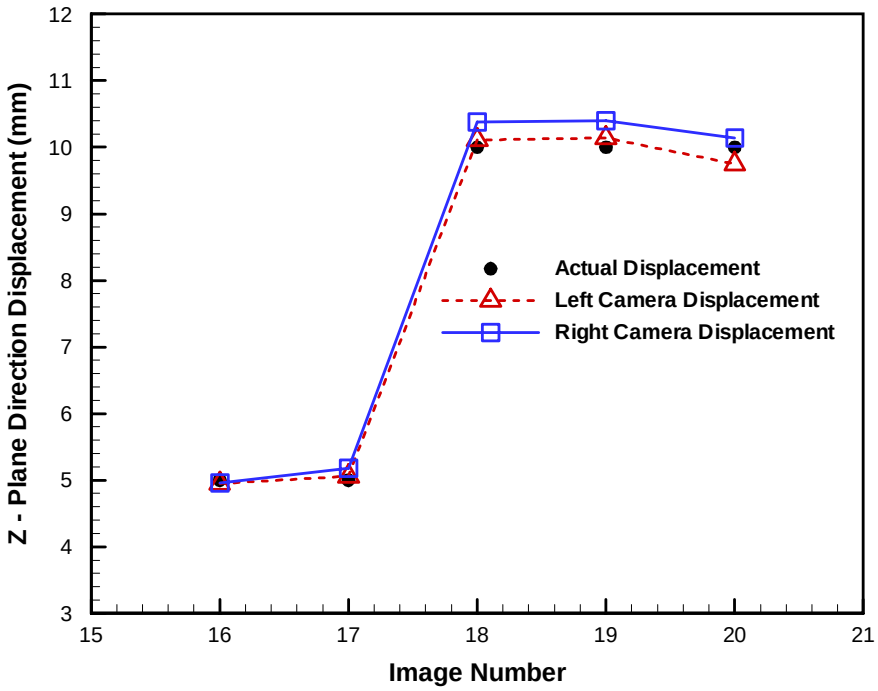

Figure 5.18 : Comparison of results for camera displacement versus actual displacement for unrectified 1632 × 1232 resolution images.

5.5 Accuracy, Errors and Limitations Discussion

Errors during camera calibration are unavoidable and can affect the accuracy of the baggy web surface profile. Similarly with all measurement methods, this method has its limitations also. Therefore, before we conclude this chapter, we will address the sources of error and limitations of the method.

5.5.1 Errors

Due to the nature of this method (non-contact measurement), the only light source in the measurements area comes from the digital projector. Typically, lightning conditions are commonly ignored in camera calibration techniques, as

pointed out by Heikkilä [32]. However, illumination variations (lighting condition) from the digital projector itself can also affect the perception of the camera significantly during calibration or when acquiring image of the baggy webs. Consequently, chromatic aberration has been observed in some of the acquired images of baggy webs.

Although, images with noticeable chromatic aberration were removed from analysis, it is uncertain the extent of chromatic aberration influences on image analysis (images with indistinguishable chromatic aberration) in terms of error; it could be detrimental to image analysis. This effect should be investigated further, but since the primary focus is to demonstrate the potential of this method, hence the rate it affects the plotted surface profile in terms of error was not considered at that time.

Corner point extraction can be another source of error, since it assists in the computation for the location of points in the three-dimensional space. This error is normally introduced by the user unintentionally when selecting the four corner points on the grid during calibration, principally when the selected point is off by the allowable 5 pixels restriction encoded in the toolbox [4].

Higher resolution images are always desirable, due to improvement in accuracy at the cost of computational power. In addition, either the degree of error will be reduced during optimization, since pixel-to-pixel error is lesser or the selected pixel may be completely off causing an error. Low resolution images on the other hand, have fewer pixels, hence it is easier to single out target points, but pixel-to-pixel error is large, thus it is possible to generate undesirable errors.

Thus, the degree of error depends on the quality of the image and how well the toolbox optimizes the corners correctly.

Selection of the wrong pixel coordinate to represent the target point can contribute error to the image processing, especially for hazy images. The occasional poor image quality tends to show different shades of similar color, making it strenuous when deciding which correct pixel coordinate to choose, hence reducing the accuracy of the calibration.

The number of calibration images and the number of sampled points used to calibrate the cameras can affect the accuracy of the measurement and yield undesirable errors, since the optimization of calibration parameters uses least square approximation algorithm. If those numbers are insufficient, the computational time will be longer and the error values will increase.

The way cameras are handled during measurement can also cause errors to the calibration process. In this case, both cameras were mounted on standard tripods to provide stability throughout the entire experiment. Although acceptable in conventional photography, it is inadequate when high accuracy is expected. Subtle vibrations (unintentional) during image acquisition process can cause unwanted errors. Thus, rigid fixtures should be used to mount the cameras in order to reduce the errors. In addition, cameras should be controlled remotely and should be triggered in tandem to maintain consistency, and to reduce physical errors during measurement.

5.5.2 Limitations

Ideally, calibration patterns should cover at least 60 percent of the entire image but it also depends on the size of the baggy web to be profiled. Usually, calibration grid selections are based on size of the entire grid, size of each square and the number of squares used on the grid. It is crucial to check the error difference between different calibration grids to determine the best grid for detecting a specific baggy web surface profile and the degree of acceptable bagginess. Therefore, to implement the proposed method on a large web line can be problematic, due to the limited number of web bagginess that can be detected.

Another limitation to this detection method is the severe fluttering of the web during web transportation, especially webs that pass through air floatation devices, in which case high speed photography needs to be implemented.

CHAPTER 6

CONCLUSION AND FUTURE WORK

Both in-plane and out-of-plane viscoelastic properties have been characterized for 2.5 mil polyethylene web. With this information, it is now possible to evaluate the pseudo-three-dimensional winding code that is currently under development at the Web Handling Research Center; to predict long-term viscoelastic characteristics of wound roll stress, strain distribution for a wide range of winding and storage conditions. This approach of measuring long-term properties of polymers using time-temperature superposition can also be applied to other web materials.

The formation of several web bagginess cases such as cambered web, baggy edges due to slitting process, baggy lane and localized baggy patches have been observed. In each case, analysis of web bagginess has been conducted. These will provide information to evaluate models for the web bagginess. However, it should be noted that there are still other web bagginess cases which have not been investigated; and will be addressed in the following section related to future work and recommendations.

Experimental results from Chapter 5 have confirmed that the proposed image analysis method has the potential to detect certain types of web bagginess in web handling. Furthermore, this approach can be developed further to couple

camera calibration method with two-dimensional digital image correlation to create a three-dimensional digital image correlation method to allow measurements of deformations on curved surfaces.

6.1 Future Work and Recommendation

Although this study has been concluded, there are still some areas that need to be investigated before the phenomenon of web bagginess can be fully understood. Further investigation on other source and behavior of web bagginess that are not covered in this study will need to be conducted, such as baggy edges from starring defects and other localized baggy patches.

In addition, baggy edges due to slitting process, discussed in this study, will need to be replicated in the laboratory. To accomplish this goal, all slitting parameters need to be investigated before a solid conclusion can be deduced. If baggy edges due to slitting process can be successfully replicated in the laboratory, then we have effectively identified some of the slitting parameters that cause baggy edges.

Higher image resolution will enable the detection of baggy edges and more subtle web bagginess; instead of just baggy lanes. But first, the camera calibration toolbox will need to be recoded into another programmable language to resolve the insufficient memory issue with MatLab and to allow the coupling with WinDIC into a single software package. This will allow not only the analysis of higher resolution images, but also the development of user-friendly software to reduce the image processing steps.

Also, there have been new developments in the three-dimensional digital image correlation method during the progress of this thesis, according to available literature search. Therefore, it is recommended to investigate those methods and compare with the proposed method in this thesis; to decide which is the better path to proceed in the development of a three-dimensional digital image correlation method, and to allow measurements of deformations on curved surfaces.

It is also recommended to have more robust platform to mount the cameras; instead of camera tripods, especially when more accurate results are needed.

REFERENCES

[1] **Altmann, H.C.** (1968): Formulas for computing the stresses in center-wound rolls. *Tappi Journal*, v51, n4, pp. 176-179.

[2] **Argon, A.S.** (1973): Low-temperature plastic deformation of glassy polymers. *The Philosophical Magazine*, v28, n4, pp. 839-865.

[3] **Arocona, C.; Dow, T.A.** (1996): The role of knife sharpness in the slitting of plastic films. *Journal of Material Science*, v31, pp. 1327-1334.

[4] **Bouguet, Jean-Yves** (1999): *Camera Calibration Toolbox for Matlab*. Available url: http://www.vision.caltech.edu/bouguetj/calib_doc/

[5] **Bouguet, Jean-Yves** (1999): *Visual methods for three-dimensional modeling*. Ph.D Thesis, California Institute of Technology, Pasadena, California.

[6] **Boyce, M.C.; Parks, D.M.; Argon, A.S.** (1988): Large inelastic deformation of glassy polymers, Part I: rate-dependent constitutive model. *Mechanics of Materials*, v7, pp. 15-33.

[7] **Brown, D.C.** (1971): Close-range camera calibration. *Photogrammetric Engineering*, v37, n8, pp. 855-866.

[8] **Brown, D.C.** (1966): Decentering distortion of lenses. *Photogrammetric Engineering*, v32, n3, pp. 444-462.

[9] **Bruck, H.A. McNeil, S.R. Sutton, M.A. Peters, W.H.** (1989): Digital

image correlation using Newton-Raphson method of partial differential correction. *Experimental Mechanics*, v29, n3, pp. 261-267.

[10] **Caprile, B. Torre, V.** (1990): Using vanishing points for camera calibration. *The International Journal of Computer Vision*, v4, n2, pp. 127-140.

[11] **Cary, P.D.** (1999): *Digital image Correlation for large deformation*. Creative Component, Oklahoma State University, Stillwater, Oklahoma.

[12] **Cerda, E. Ravi-Chandar, K. Mahadevan, L.** (2002): Wrinkling of an elastic sheet under tension. *Nature,* v 419, pp. 579-580.

[13] **Clarke, T.A.; Fryer, J.G.** (1998): The development of Camera Calibration Methods and Models. *Photogrammetric Record*, v16, n91, pp. 51-66.

[14] **Clarke, T.A.; Fryer, J.G.; Wang, X.** (1998): The principal point and CCD cameras. *Photogrammetric Record*, v16, n92, pp. 293-312.

[15] **Doi, M.** (1986): *The Theory of Polymer Dynamics*. Oxford University Press.

[16] **Eyring, H.; Ree, T.** (1958): *In: Rheology, Ed By F.R. Eirich, Vol. II*. Academic Press, New York.

[17] **Feiertag, B.** (2003): *An Application Seminar on Web Handling*. Oklahoma State University, Stillwater, Oklahoma.

[18] **Feiertag, B.; Shelton, J.J.; Markum, R.** (2005): Private communications on typical winding tension for polyethylene webs.

[19] **Ferry, J.D.** (1980): *Viscoelastic Properties of Polymers*. John Wiley & Sons, 3rd Ed., pp. 7 &17.

[20] **Findley, W.N.; Lai, J.S.Y.** (1966): *Brown University Report*. *EMRL-27*.

[21] **Friedl, N.; Rammerstorfer, F.G.; Fischer, F.D.** (2000): Buckling of Stretched Strips. *Computer and Structures*, v78, n1, pp. 185-190.

[22] **Fryer, J.G.; Brown, D.C.** (1986): Lens Distortion for Close-Range Photogrammetry. *Photogrammetric Engineering and Remote Sensing*, v52, n1, pp. 51-58.

[23] **Fung, Y.C.** (1993): *Biomechanics, Mechanical Properties of Living Tissues, 2nd.* Springer-Verlag, New York.

[24] **Ganesan Balaji** (2000): *Deformation Measurements by digital image correlation: Implementation of third-order displacement gradients*. M.S. Thesis, Oklahoma State University, Stillwater, Oklahoma.

[25] **Garcia, D.; Orteu, J.J.; Penazzi, L.** (2002): A combined temporal tracking and stereo-correlation technique for accurate measurement of 3D displacements: application to sheet metal forming. *Journal of Materials Processing Technology*, v125-126, pp. 736-742.

[26] **Good, J.K.; Vaidyanathan, N.** (1995): The importance of torque capacity in predicting crepe wrinkling and starring in wound rolls. *Proceedings of the 3rd International Conference on Web Handling*, Web Handling Research Center, Stillwater, Oklahoma, June 18-21.

[27] **Ha, K.; Schapery, R.A.** (1998): A three-dimensional viscoelastic constitutive model for particulate composite with growing damage and its experimental validation. *International Journal of Solids and Structures*, v35, n26-27, pp. 3497-3517.

[28] **Habeger, C.C.** (1993): Tension wrinkling and the fluting of light-weight coated papers in web-offset printing. *Journal of Pulp and Paper Science*, v19, n5, pp. J214-J218.

[29] **Hakiel, Z.** (1987): Nonlinear model for wound roll stresses. *Tappi Journal*, v75, n3, pp. 113-117.

[30] **Hartley, R.I.** (1994): An algorithm for self calibration from several views. *Proc. IEEE Conference on Computer Vision and Pattern Recognition*, Seattle, WA, pp. 908-912.

[31] **Hasan, O.A.; Boyce, M.C.** (1995): A constitutive model for the nonlinear Viscoelastic viscoplastic behavior of glass polymers. *Polymer Engineering and Science*, v35, n4, pp. 331-344.

[32] **Heikkilä, J.** (2000): Geometric Camera Calibration using Circular Control Points. *IEEE Transactions on Pattern Analysis and Machine*, v22, n10, pp. 1066-1077.

[33] **Heikkilä, J.; Silvén, O.** (1997): A Four-step Camera Calibration Procedure with Implicit Image Correction. *IEEE Computer Society Conference on Computer Vision and Pattern Recognition*, San Juan, Puerto Rico, pp. 1106-1112.

[34] **Hopkins, I.L.** (1958): Stress relaxation or creep of linear viscoelastic substances under varying temperature. *Journal of Polymer Sciences*, v28, n118, pp. 631-633.

[35] **Jorge Abanto-Bueno; John Lambros** (2002): Investigation of crack growth in functionally graded materials using digital image correlation.

Engineering Fracture Mechanics, v69, pp. 1695-1711.

[36] **Kim, Gyu-ho** (2003): *Accelerated lifetime testing of carbon filled polycarbonate under cyclic loading conditions*. PhD. Thesis, Oklahoma State University, Stillwater, Oklahoma.

[37] **Knauss, W.G.; Emri, I.J.** (1981): Non-linear viscoelasticity based on free-volume consideration. *Computers & Structures*, v13, n1-3, pp. 123-128.

[38] **Knauss, W.G.; Gonzalez, J.** (1998): Strain inhomogeneity and discontinuous crack growth in a particulate composite. *Journal of Mechanics and Physics of Solids*, v46, n10, pp. 1981-1995.

[39] **Lai, J.; Bakker, A.** (1995): An integral constitutive equation for nonlinear plasto-viscoelastic behavior of high density polyethylene. *Polymer Engineering and Science*, v35, n17, pp. 1339-1347.

[40] **Leadermann, H.** (1943): *Elastic and creep preperties of filamentous materials*. Textile Foundation, Washington D.C..

[41] **Lemaitre, J.** (1990): Micro-mechanism of crack initiation. *International Journal of Fracture*, v42, pp. 87.

[42] **Liebowitz, D.; Zisserman, A.** (1998): Metric rectification for perspective images of planes. *Proc. IEEE Conference on Computer Vision and Pattern Recognition*, Santa Barbara, CA, pp. 482-488.

[43] **Lin, P.M.; Wickert, J.A.** (2006): Corrugation and buckling defects in wound rolls. *Journal of Manufacturing Science and Engineering (Transactions of the ASME)*, v128, n1, pp. 56-64.

[44] **Liu, C.; Lu, H.; Huang, Y.** (2005): Dynamic steady-state stress field in web during slitting. *Journal of Applied Mechanics*, v72, pp. 157-164.

[45] **Lu, H.; Cary, P.D.** (2000): Deformation measurements by digital image correlation: implementation of a second-order displacement gradient. *Experimental Mechanics*, v40, n4, pp. 393-400.

[46] **Lu, H.; Katti, A.; Kim, Gyu-ho; Huang, G.; Poh, Jo-Ong E.** (2003*): Accelerated material property testing of Tecothane used in the Grommet under saturated saline conditions*. Final Report to Medtronic.

[47] **Lu, H.; Knauss, W.G.** (1999): The role of dilatation in the nonlinearly viscoelastic behavior of PMMA under multiaxial stress states. *Mechanics of Time-Dependent Materials*, v2, n4, pp. 307-334.

[48] **Lu, H.; Liu, C.** (1999): The stress field in a web during slitting - opening mode. *Proceedings of the 5th International Conference on Web Handling*, Oklahoma State University, pp. 235-250.

[49] **Lu, H.; Vendroux, G.; Knauss, W.G.** (1997) : Surface deformation measurements of a cylindrical specimen by digital image correlation. *Experimental Mechanics*, v37, n4, pp. 433-439.

[50] **Lu, H.; Wang, B.; Iqbal,J.** (2001): Deformation in shear slitting of polymeric webs. *Proceedings of the 6th International Conference on Web Handling*, Oklahoma State University, pp. 389-402.

[51] **Lu, H.; Zhang, X.H.; Knauss, W.G.** (1997): Uniaxial shear and poisson relaxation and their conversion to bulk relaxation - Studies on Polymethyl Methacrylate. *Polymer Engineering and Science*, v37, n6, pp. 1053-1064.

[52] **Luo, P.F.; Chao, Y.J.; Sutton, M.A.; Peters, W.H.** (1993): Accurate Measurement of the Three-dimentional deformations in deformable and rigid bodies using computer vision. *Experimental Mechanics*, v33, n2, pp. 123-132.

[53] **Luong, Q.-T.; Faugeras, O.** (1997): Self-calibration of a moving camera from point correspondences and fundamental matrices. *The International Journal of Computer Vision*, v22, n3, pp. 261-289.

[54] **Ma, Jin; Lu, H.; Li, Ming; Wang, B.** (2006): Burr height in shear slitting of aluminum webs. *Journal of Manufacturing Science and Engineering (Transactions of the ASME)*, v128, pp. 46-55.

[55] **Maybank, S.J.; Faugeras, O.D.** (1992): A theory of self-calibration of a moving camera. *The International Journal of Computer Vision*, v8, n2, pp. 123-152.

[56] **McCrum, N.G.; Buckley, C.P.; Bucknall, C.B.** (2003): *Principles of polymer engineering*. Oxford University Press, USA, pp. 117-176.

[57] **Meehan, R.R.; Burns, S.J.** (1998): Mechanics of slitting and cutting webs. *Experimental Mechanics*, v38, n2, pp. 103-109.

[58] **Meehan, R.R.; Kumar, J.; Earl, M.; Svenson, E.; Burns, S.J.** (1999): Role of blade sharpness in cutting instabilities of Polyethylene Teraphthalate. *Journal of Materials Science Letters*, v18, n2, pp. 93-95.

[59] **Meyers, M.A.; Chawla, K.K.** (1999): *Mechanical Behavior of Materials*. Prentice-Hall, pp. 98-103.

[60] **Mukherjee, B.; Burns, D.J.** (1971): Fatigue-crack growth in Polymethyl Methacrylate. *Experimental Mechanics*, vii, n10, pp. 433-469.

[61] **Palanisamy, Muthazhagu** (2004): Development of surface profile measurement technique for measuring baggy lanes. *M.S. Thesis*, Oklahoma State University, Stillwater, Oklahoma.

[62] **Periasamy, Sampath Kumar** (2002): *Digital image correlation for deformation measurements near a crack*. M.S. Thesis, Oklahoma State University, Stillwater, Oklahoma.

[63] **Peters, W.H.; Ranson, W.F.** (1982): Digital imaging techniques in experimental stress analysis. *Optical Engineering*, v21,n3, pp. 427-432.

[64] **Pfeiffer, J.D.** (1981): Measurement of the K2 factor for paper. *Tappi Journal*, v64, n4, pp. 105-106.

[65] **Pfeiffer, J.D.** (1979): Prediction of roll defects from roll structure formulas. *Tappi Journal*, v62, n10, pp. 83-85.

[66] **Pfeiffer, J.D.** (1966): Internal Pressures in a Wound Roll of Paper. *Tappi Journal*, v49, n8, pp. 342-347.

[67] **Poh, Jo-Ong E.; Palanisamy, Muthazhagu; Lu, H.** (2005): Non-contact three-dimensional surface profiling for web baggy lanes detection. *AIAA/ASME Oklahoma Symposium XXV*, pp. 41.

[68] **Prall, G.M.**: *How to solve blown film problems*. Technical Brochure from Battenfield-Glouster.

[69] **Qualls, W.R.** (1995): *Hygrothermomechanical Characterization of Viscoelastic Centerwound Rolls*. PhD. Thesis, Oklahoma State University,

Stillwater, Oklahoma.

[70] **Roisum, D.R.** (2001): Baggy webs: making, measurement and mitigation thereof. Available url: http://roisum.com/Downloads.htm

[71] **Roisum, D.R.** (1998): Wrinkling of Thin Webs. *41st Annual Technical Conference Proceedings (Society of Vacuum Coaters)*, pp. 406-411.

[72] **Schapery, R.A.** (1997): Thermoviscoelastic constitutive equations for polycrystalline ice. *ASCE Journal of Cold Regions Engineering*, ASCE11, pp. 146-157.

[73] **Schapery, R.A.** (1997): Nonlinear viscoelastic and viscoplastic constitutive equations based on thermodynamics. *Mechanics of Time-Dependent Materials*, v1, pp. 209-240.

[74] **Schapery, R.A.** (1969): On the Characterization of Nonlinear Viscoelastic Materials. *Polymer Engineering and Science*, v9, n4, pp. 295 - 310.

[75] **Shelton, J.J.** (1997): Effects of web camber on handling. *Proceedings of the 4th International Conference on Web Handling*, Oklahoma State University, pp. 248-259.

[76] **Shelton, J.J.** (1993): Buckling of webs from lateral compressive forces. *Proceedings of the 2nd International Conference on Web Handling*, Oklahoma State University, pp. 303-321.

[77] **Slama, C.C. (ed)** (1980): *Manual of photogrammetry, 4th Ed.* American Society of Photogrammetry.

[78] **Smith, R.D.** (1995): *Roll and web defect terminology*. TAPPI Press.

[79] **Struik, L.C.E.** (1978): *Physical Aging in Amorphous Polymers and Other Materials*. Elsevier Scientific Publishing Company.

[80] **Sutton, M.A.; Cheng, M.; Peters, W.H.; Chao, Y.J.; McNeill, S.R.** (1986): Application of an optimized digital image correlation method to planar deformation analysis. *Image Vision Computing*, v4, n3, pp. 143-150.

[81] **Sutton, M.A.; Turner, J.L.; Bruck, H.A.; Chae, T.A.** (1991): Full-field representation of discretely sampled surface deformation for displacement and strain analysis. *Experimental Mechanics*, v31, n2, pp. 168-177.

[82] **Sutton, M.A.; Wolters, W.J.; Peters, W.H.; Ranson, W.F.; McNeill, S.R.** (1983) Determination of displacements using an improved digital correlation method. *Image Vision Computing*, v1, n3, pp.133-139.

[83] **Thormählen, T.; Broszio, H.; Wassermann, I.** (2003): Robust line-based calibrations of lens distortion from a single view. *Proceedings of Mirage 2003,* INRIA Rocquencourt, France, pp. 105-112.

[84] **Timoshenko, S.P.; Gere, J.M.** (1961): *Theory of elastic stability*. McGraw-Hall, New York, 2nd ed., pp.348-439.

[85] **Tramposch, H.** (1967): Anisotropic Relaxation of Internal Forces in a Wound Reel of Magnetic Tape. *Journal of Applied Mechanics*, v34, pp. 888-894.

[86] **Tramposch, H.** (1965): Relaxation of Internal Forces in a Wound Reel of Magnetic Tape. *Journal of Applied Mechanics*, v32, n4, pp. 865-873.

[87] **Tsai, R.Y.** (1987): A Versatile Camera Calibration Technique for High-Accuracy 3D Machine Vision Metrology Using Off-the-Shelf TV Cameras and Lenses. *IEEE J. of Robotics and Automation*, vRA-3, n4, pp. 323-344.

[88] **Vendroux, G.** (1990): *Correlation: A Digital Image Correlation Program for Displacement and Displacement Gradient Measurements*. ALCIT Report No.SM90-19, California Institute of Technology.

[89] **Vendroux, G.; Knauss, W.G.** (1998): submicron deformation field measurements: Part 1. Developing a digital scanning tunneling microscope. *Experimental Mechanics*, v38, pp. 18-23.

[90] **Vendroux, G.; Knauss, W.G.** (1998): submicron deformation field measurements: Part 2. Improved digital image correlation. *Experimental Mechanics*, v38, pp. 86-91.

[91] **Vendroux, G.; Knauss, W.G.** (1998): submicron deformation field measurements: Part 3. Demonstration of deformation determinations. *Experimental Mechanics*, v38, pp. 154-160.

[92] **Wang, B.; Lu, H.; Kim, G.** (2002): A damage model for the fatigue life of elastomeric materials. *Journal of Mechanics of Materials*, v34, n8, pp. 475-483.

[93] **Wei, Tong** (2004): Plastic Surface Strain Mapping of Bent Sheets by Image Correlation. *Experimental Mechanics*, v44, n5, pp. 502-511.

[94] **Williams, M.L.; Landel, R.F.; Ferry, J.D.** (1955): The temperature dependence of relaxation mechanisms in Amorphous Polymers and other

Glass-Forming Liquids. *Journal of American Chemical Society*, v77, pp. 3701-3707.

[95] **Yu, Haowen** (2003): *Three-dimensional viscoelastic winding models for the analysis of baggy lanes formation*. Preliminary Exam Report for PhD. Oklahoma State University, Stillwater, Oklahoma.

[96] **Yu, Haowen; Poh, Jo-Ong E.; Wang, Bo; Lu, Hongbing** (2004): *Buckling analysis of a web under tension*. Web Handling Research Center, Oklahoma State University, Semiannual Meeting & Technical Review and Industry Advisory Board Meeting (Report).

[97] **Zhang, Zhengyou** (1999): Flexible Camera Calibration By Viewing a Plane from Unknown Orientations. *International Conference on Computer Vision*, Corfu, Greece, pp. 666-673.

APPENDIX A

A.1 Image Preparation

Depending on the camera model, resolution and format used to capture experimental images, the images might need to be converted for several reasons, mainly ease of handling and to reduce computational memory. Although the Camera Calibration Toolbox can handle images from most common formats (i.e. jpeg, gif and tiff) and resolution, memory problems were encountered at the later stages of the calibration process such as stereo calibration stage and image rectification stage. Similarly, the current WinDIC versions can only handle grayscale images in *tiff* (tagged image file format) format so images of other formats have to be converted to tiff images first.

Therefore, to standardize all images used in the study, all the images were either converted to 640 × 480 or 800 × 600 resolutions in grayscale. The software called *GNU Image Manipulation Program*, or commonly known as *GIMP* version 2.2.11 (freeware), was used to resize the image resolution if needed, whereas the program called *Pic2Pic* version 1.2 (freeware) was used to convert the images into grayscale tiff format.

The calibration images consist of a set of sequential images captured with chessboard pattern, similar to the one shown in Figure A.1. If more than one camera is used, the sequence of images for both cameras must be of the same

pair else the stereo calibration process in the later part will fail. Object images used by WinDIC have to be of the same pair, to ensure accurate measurement of the deformation; and most importantly, good convergence of the software.

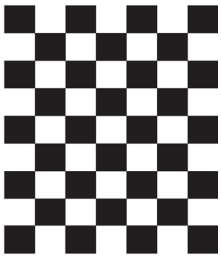

Figure A.1 : Example of a chessboard pattern used for calibration.

The chessboard patterns can be made using any computer software; in this study, they are made using *AutoCAD* and printed to scale using a laser printer. Depending on the area of interest of the target object, the size of the grid, number of grid in the horizontal and vertical direction need to be taken into consideration. For smaller area of interest, the size of the grid needs to be reduced to smaller scale for better accuracy. It is also recommended to have the number of the vertical grids more than that of the horizontal grids, in situation where error will occur during calibration.

A.2 Single Camera Calibration

In preparation for the calibration process, the MatLab files related to the *Camera Calibration Toolbox for MatLab* should be stored into a separate folder to avoid any confusion with the original MatLab software files. After loading the MatLab software, the location of the separate folder needs to be added into the main MatLab path, hence enabling access to all functions from the camera

calibration toolbox. These steps should be taken when running the camera calibration toolbox for the first time.

Using Figure 5.4 as a reference to the entire process, we will focus on the main steps that perform the actual image calibration process for each camera, as shown in Figure A.2. Additional information and instructions on this section can be obtained from Dr. Bouguet's website [4] where the toolbox was downloaded.

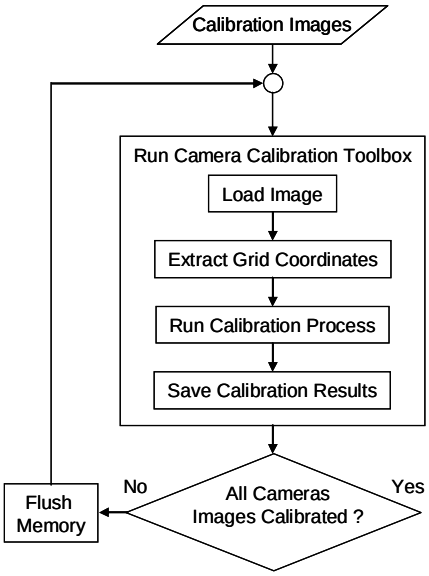

Figure A.2 : The Image Calibration Section of the entire procedure used to obtain the three-dimensional surface profile of baggy lanes.

To initiate the Camera Calibration Toolbox in MatLab, the script needs to be loaded by typing the command ***calib_gui*** in the command window of MatLab that will produce a selection window similar to Figure A.3.

Figure A.3 : The Camera Calibration Toolbox Mode selection window.

The *'Standard'* option will load all the images into memory, hence avoiding the need to reread the images from the disk again [4]. Although it saves time by speeding up the entire process, there is a possibility of *'Out of Memory'* error message appearing when loading too many high resolution images. The alternative is the *'Memory efficient'* option where it reduces the memory usage since the images are never kept in memory but it requires the user to load the images individually [4].

The selection of either option will produce a new user-friendly selection window that is identical to Figure A.4. In this study, the standard option is commonly used and at this point we are inside the *Run Camera Calibration Toolbox* module in Figure A.4.

The prepared calibrate images that have been converted can now be loaded using the *'Image names'* button from Figure A.4. The MatLab command window will then request the user to enter the base-name for the images and the format. Once all the images have been loaded properly, a separate window will appear containing a complete set of images to be calibrated. If the *'Out of Memory'* error message appears at this point, it means that the computer does not have sufficient RAM memory hence the *'Memory efficient'* mode will need to be used instead [4].

Figure A.4 : The main Camera Calibration Toolbox window.

Once all images are loaded, it is time to extract the grid coordinates of each image by clicking on the button called *'Extract grid corners'*, as shown in Figure A.4. The instructions and questions that appear on the MatLab command window are self-explanatory, however one should pay attention to several key features.

One of the features is the size of the corner finder; this parameter defines the area of which the algorithm will search for the corner of the grid or calibration pattern on the image [4]. Depending on pre-defined size, the projection error and uncertainties on the calibration parameters may vary [4]. For this feature, it is advisable to initially use the default value during the initial stages of calibration then later refine it through trial and error if required. Procedure to refine the corner finder size can be referred to via Dr. Bouguet's website [4].

The program has a built-in corner extraction algorithm where it automatically counts the number of squares in the grid thus speeding up the calibration process [4]. However, for some extreme cases; the algorithm may not count the right number of squares due to lens distortions. Information on the steps to correct these rare cases can also be obtained from Dr. Bouguet's website [4].

Care should be taken when clicking for the corners grid, otherwise the algorithm might not detect the calibration grid properly; normally, no more than 5 pixels away from the corner should be sufficient [4]. It should be noted that the first clicked corner will represent the origin of the reference frame for that image. Hence, it's crucial that the sequence of corner selection should be maintained

consistent throughout the calibration process, especially when calibrating multiple cameras. The recommended sequence by Dr. Bouguet can be observed in Figure A.5.

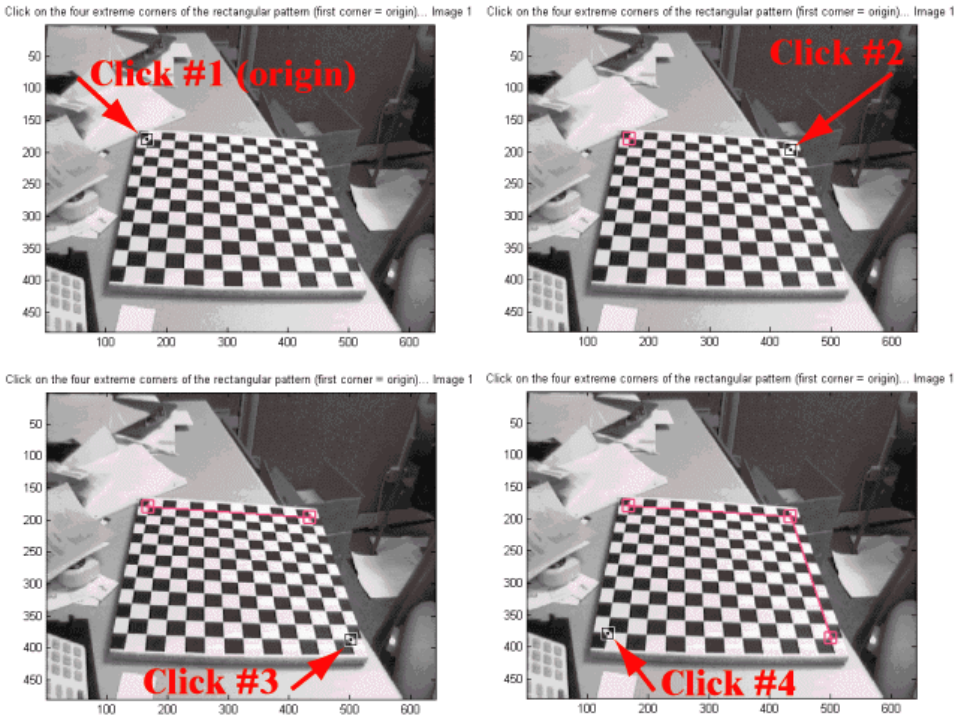

Figure A.5 : Recommended corner selection sequence by Dr. Bouguet [4].

During the corner extraction procedure, there will be a pair of parameter called ***dX*** and ***dY*** that need to be specified. These parameters represent the actual size of a square, as observed in units of millimeters (mm), hence when making the chessboard pattern, it is recommended to have a known standard size [4].

Once the corners are automatically extracted from the image, the resulting image will look similar to Figure A.6. Typically, the corners extracted by the algorithm has an accuracy of approximately 0.1 pixels [4] but occasionally, the

predicted corners does not fall close to the real image corners, hence additional refinement needs to be made to account for lens distortion. There is an exhaustive list of suggestions that can be used and are available on Dr. Bouguet's website [4].

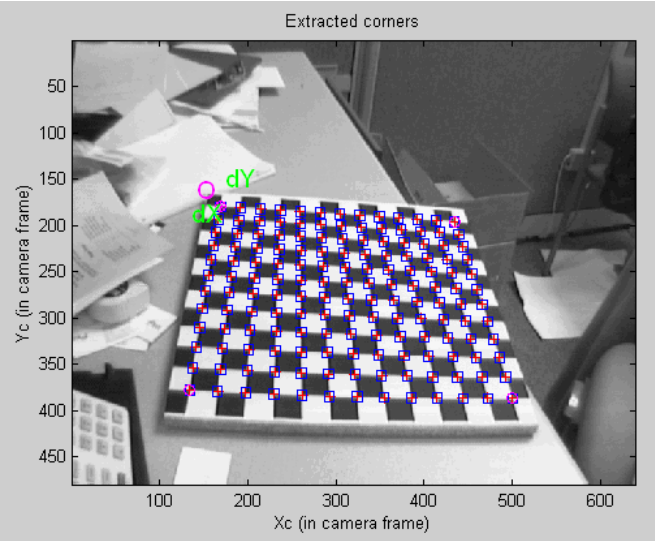

Figure A.6 : An example of a resulting image that has it's corners extracted automatically [4].

When the corner extractions have been completed for all images, a file will be generated called ***calib_data.m*** that contains image coordinates, corresponding three-dimensional coordinates and grid parameters [4]. At this point, commence the calibration process by clicking on the button called *'Calibration'* as shown in Figure A.4. The calibration process consists of two steps; the first is the initialization stage while the second is the nonlinear optimization stage. In the first stage, the close-form solution for the calibration parameters is obtained while in the second stage the non-linear optimization is performed by iterating the gradient decent with an explicit computation of the

Jacobian matrix that minimizes the total reprojection error among all the calibration parameters [4]. Details of the calibration process are readily available on the website hosted by Dr. Bouguet [4].

After the calibration process has been completed, the calibrated data should be saved and properly renamed (i.e. ***Calib_Results_right*** and ***Calib_Results_left***) for later use. At this point, if there are additional cameras that need to be calibrated, it is recommended to flush the MatLab memory clean prior to starting a new set of calibration images from another camera to avoid any confusion and possible errors that might occur later. If all sets of images have been already calibrated, then it's time to move on to the next phase which is *stereo camera calibration*.

In addition to the fundamental steps used to perform the actual image calibration process for each camera, as shown in Figure A.2, there are several other features that should be addressed on the main Camera Calibration Toolbox window, in Figure A.4.

The *'Show Extrinsic'* button on the main Camera Calibration Toolbox window will plot in camera reference frame the positions of the grid with respect to the sequence of calibration images used in the calibration process [4]. This plot can also be viewed in the world coordinates system allowing the user to get a better picture of the calibration images used and for troubleshooting purposes. Figure A.7 is an example of such plots taken from Dr. Bouguet's website [4].

'Analyze error' button displays the distribution of errors occurring due to distortion effects and improper extraction of points [4]. The plot allows the user to

decide how much refinement is needed in the calibration process and which image needs to be refined further.

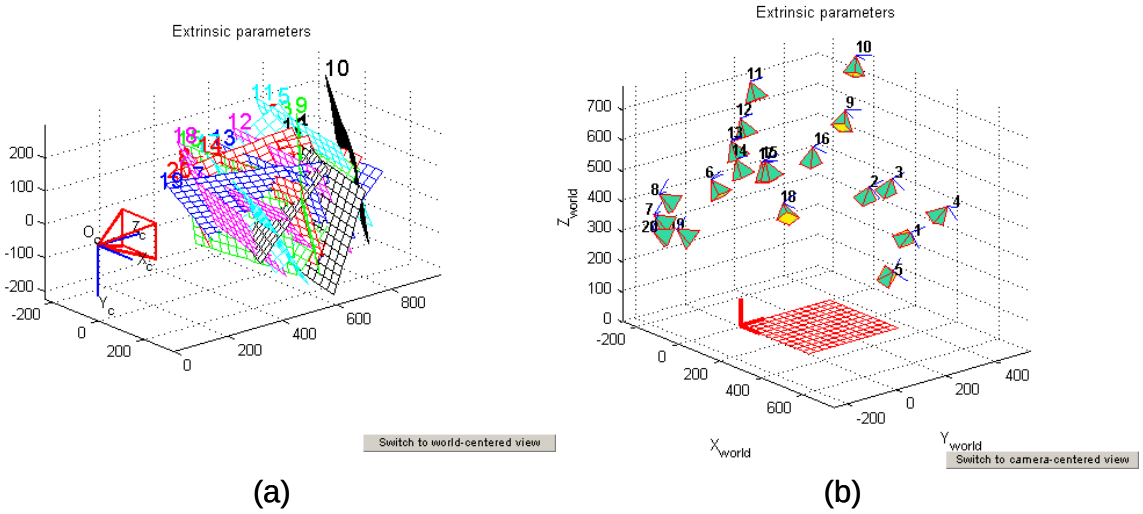

(a) (b)

Figure A.7 : Example of possible plots that can be obtained from the *'Show Extrinsic'* function taken from Dr. Bouguet's website [4] where (a) positions of the calibration grid plotted in camera reference frame, (b) world coordinates system.

Most of the other buttons and features that were not addressed by this discussion are used to assist in the refinement process of the calibration procedure and are not commonly used. The description for each of them will not be addressed here due to the complexities of each feature, however, further reading material regarding these features can be obtained from Dr. Bouguet's website [4].

A.3 Stereo Camera Calibration

From Figure 5.4, we will now describe the toolbox that calibrates both cameras to gather information about their position in three-dimensional space with respect to each other. This sub-section can be observed from Figure A.8.

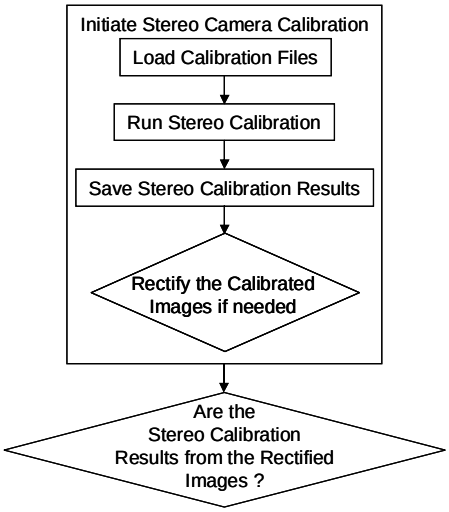

Figure A.8 : The sequence of procedure that occurs within the Stereo Camera Calibration Toolbox.

At this point, all calibration images from each camera should have been calibrated using Camera Calibration Toolbox. Before loading the Stereo Camera Calibration Toolbox, the MatLab memory should be cleared. Then, all the calibration data generated from the Camera Calibration Toolbox should be loaded into MatLab by typing the load command in the MatLab command window (i.e. ***load calib_data_left*** and ***load calib_data_right***).

To begin Stereo Camera Calibration in MatLab, the script needs to be invoked by typing the command ***stereo_gui*** in the MatLab command window. A

new graphic user-interface window will appear with a list of options that looks similar to Figure A.9.

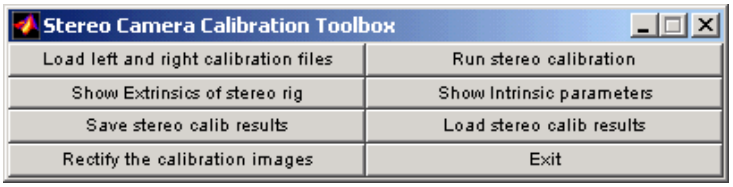

Figure A.9 : The Stereo Camera Calibration Toolbox window.

Click the *'Load left and right calibration files'* button to load the calibration files for each camera created by the Camera Calibration Toolbox earlier; the instructions in this loading step are relatively simple and easy to follow.

Once all required files are loaded, the program is ready to start the global stereo optimization and can be initiated by clicking the *'Run stereo calibration'* button. The program will automatically recompute the intrinsic and extrinsic parameters including all the uncertainties that come together from each camera to minimize the projection error [4]. On occasions, the uncertainties of the intrinsic parameters may be reduced after this process because the global stereo optimization is performed over a minimal set of unknown parameters [4]. When the stereo calibration is completed, the results will be displayed on the screen. The stereo calibration results can be saved by clicking the button called *'Save stereo calib results'*.

If this is the initial stereo calibration round then it can be concluded that the calibration images used in the camera calibration process to be in an refine form or commonly known as *unrectified images*. This means that the extracted corner points of the calibration images have not been corrected to compensate

for any distortions, thus the entire calibration process that has been completed till now may still contain some errors. This process is important because it ensures that both left and right cameras are 'looking' at the same point by having their epi-polar lines stay along the same unit normal [4]. To resolve this problem, simply click on the *'Rectify the calibration images'* button and the algorithm will automatically correct the calibration images by taking into account all the distortion values hence repairing the extracted corner points.

In most cases, the difference between an unrectified image and a rectified image can be significant, as indicated by Figure A.10. Therefore, once all calibration images have been newly rectified; the entire calibration procedure will have to be repeated from the very beginning, as indicated by Figure A.8; except this time, the rectified calibration images will be used instead. Although the initial uncorrected calibration images may no longer be needed at this point, it is recommended to keep the images as a reference and backup; similar case applies to all calibration results and data.

Lastly, the other features available within this toolbox will be briefly discussed. *'Show Extrinsics of stereo rig'* button functions the same way as *'Show Extrinsic'* button from the main Camera Calibration Toolbox where it will plot the camera reference frame the positions of the grid with respect to the sequence of calibration images used in the calibration process [4]. The only difference is the presence of both left and right cameras in this plot since this is the stereo camera calibration toolbox. Figure A.11 is an example of such plot taken from Dr. Bouguet's website [4] for comparison.

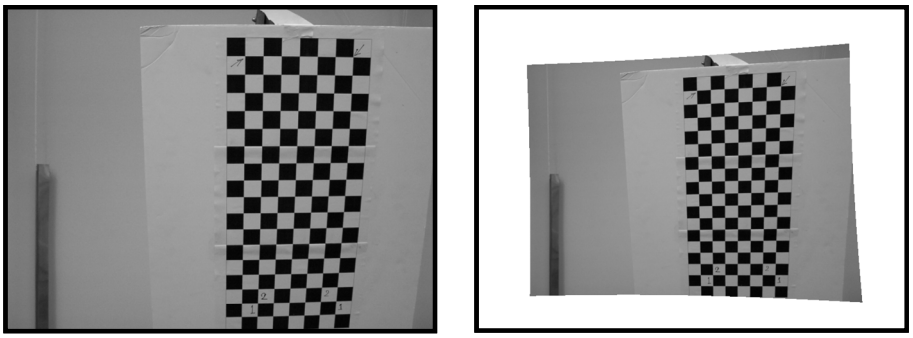

(a) (b)

Figure A.10 : A comparison between (a) an unrectified (uncorrected) image with (b) a rectified (corrected) image. Note that both images in fact originally came from the same calibration image file (a) and the rectified image (b) no longer has a straight square side borders attributed from the distortion correction.

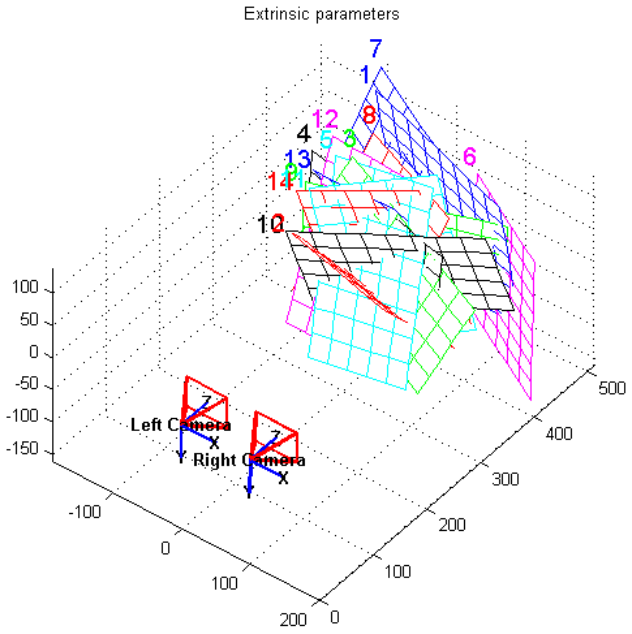

Figure A.11 : An example of plot created from the *'Show Extrinsics of stereo rig'* function where it illustrates the positions of the calibration grid plotted in camera reference frame including both left and right camera. This example was taken from Dr. Bouguet's website [4].

The *'Show Intrinsic parameters'* button simply redisplays the intrinsic parameters of the individual cameras, before and after stereo calibration results whereas the *'Load stereo calib results'* button basically reload the stereo calibration results into the MatLab session [4].

As a precautionary reminder, when extracting grid points during camera calibration, proper care should be taken for each pair of images (left and right camera) to have the same set of points selected and in the same sequence. Thus, the same grid of points and the same origin point should be selected to maintain uniformity else, the stereo calibration process will either fail or produce unusable results.

Also, while acquiring the images during experiment, both cameras should not be disturbed with any unnecessary vibrations throughout the image acquisition process. Similarly, the grid pattern used should be kept in the same position when image acquisition is taking place for both cameras. The grid should only be moved once the image pairs have been acquired else possible failure might occur in the program during the stereo calibration phase.

When obtaining surface profiles of smaller area hence higher accuracy, it is recommended to have a rigid and robust mount for the cameras and the calibration grid pattern. If not, it will incur additional distortion errors and could possibly terminate the program while the stereo calibration process is in progress with the following message; '*Disabling view kk – Reason: the left and right images are found inconsistent'*.

A.4 Digital Image Correlation

In the past, the pixel coordinates of the target object; captured by both the left and right camera, were obtained manually using *GIMP* software [61]. This method was very tedious and time consuming hence impractical; especially when there are large numbers of data points to be extracted for both left and right camera image.

This section will address an alternative method that expedites this task significantly with the use of WinDIC in acquiring the pixel coordinates of the target object [67]. The images containing the object captured by both left and right camera shall henceforth be referred to as *object image* for convenience. Figure A.12 gives an overview of the area that will be discussed in this section.

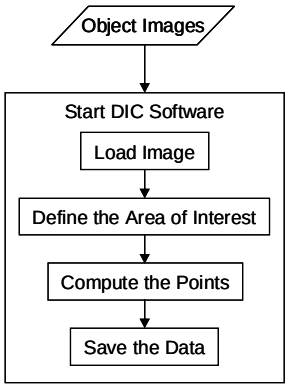

Figure A.12 : Progression of WinDIC in acquiring image coordinates of target object.

WinDIC can easily be launched since it is an executable file. Once launched, to load the object images simply go to the File tab displayed in Figure A.13 and click on the *'Add'* button to select the files. Note that object images with

corresponding patterns for both left and right camera must be loaded in pairs, else the DIC algorithm will not converge hence rendering the process worthless. Also, the image pairs should be captured by left and right cameras at the same sequence and preferably simultaneously with the only difference in perspective, to avoid any physical errors that may occur, for better accuracy.

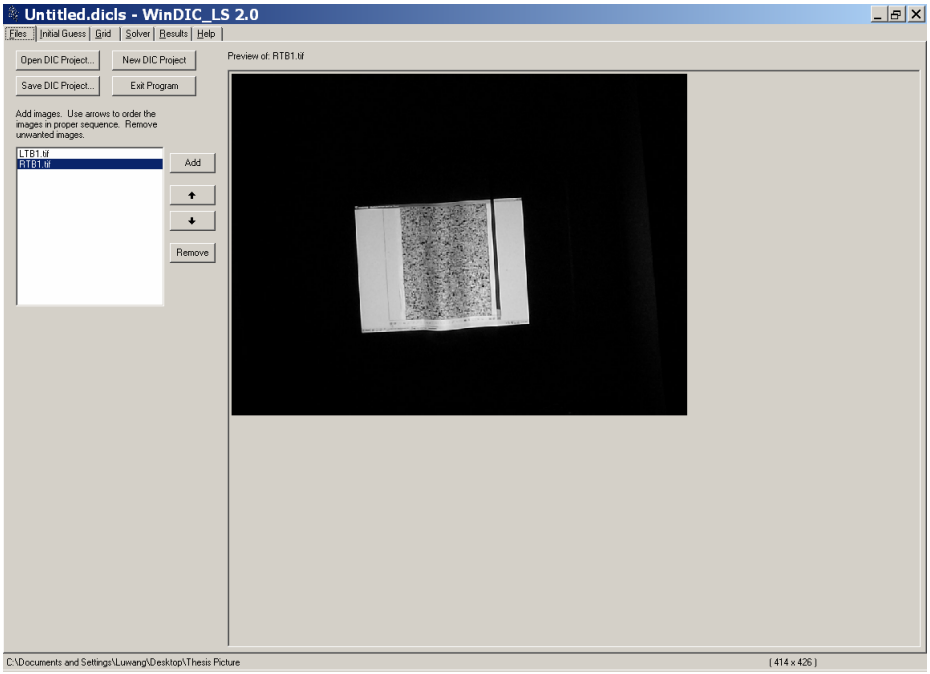

Figure A.13 : The starting tab of WinDIC software.

Once the object images are loaded, proceed to the *Initial Guess* tab to pick a distinctive point on the left image. That point will be the reference point on the reference image; in this study, left camera object image will be used as the reference image. The next task is to find that same point on the right side which represents the right camera object image as indicated by Figure A.14. Notice the features where object images can be blown up to full scale, fitted to scale and

zoomed accordingly; these features however will not influence the algorithm in determining the image coordinates. In fact, for some images that may be too large, they can be moved for a better view within their assigned area by holding the right-mouse button and dragging the mouse around.

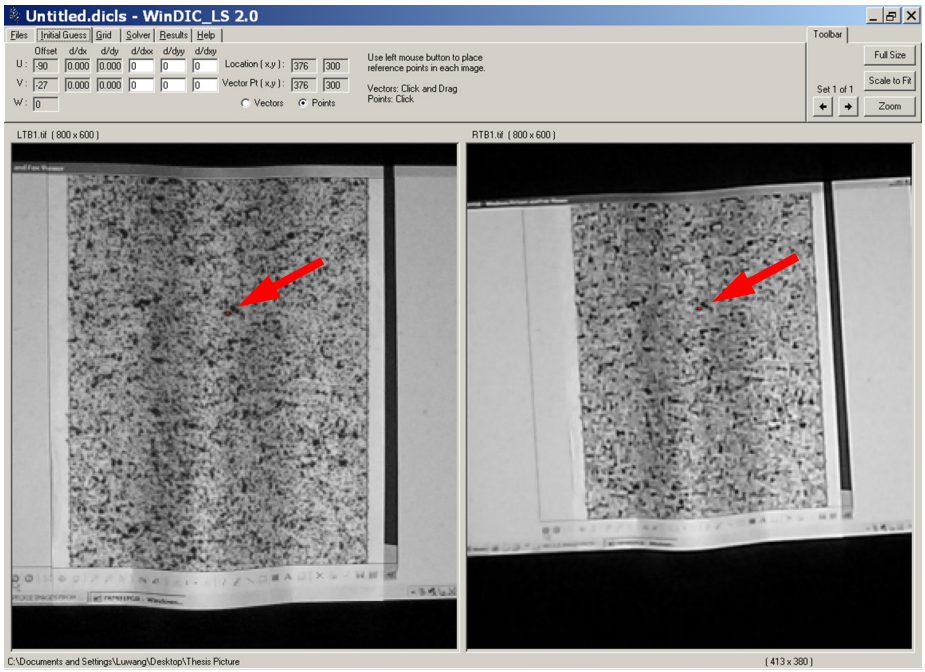

Figure A.14 : The tab in which the initial point will be picked. Note the similarities in terms of point distribution for both images. The initial point picked on both the images must be the same for WinDIC. As a result, on the left image notice the arrow pointing to a specific location on the image; and on the right it also corresponds to the same location.

After defining the initial point, the number of nodes and spacing of the nodes are set to cover the area of interest. Concurrently on the left side of the window, a mesh will emerge on the top-left corner of the left object image and

should be moved to cover the area of interest. This mesh will represent the area of which the DIC algorithm will map to find the coordinates of the nodes as shown in Figure A.15. On the right side of the window, a faint border will appear automatically to indicate the corresponding area to be mapped on the right object image. Also, note that there is a variety of mapping sequence available in WinDIC; to make it consistent with the Camera Calibration Toolbox for MatLab algorithm, the *'Left-Right'* mapping sequence is used for this entire study.

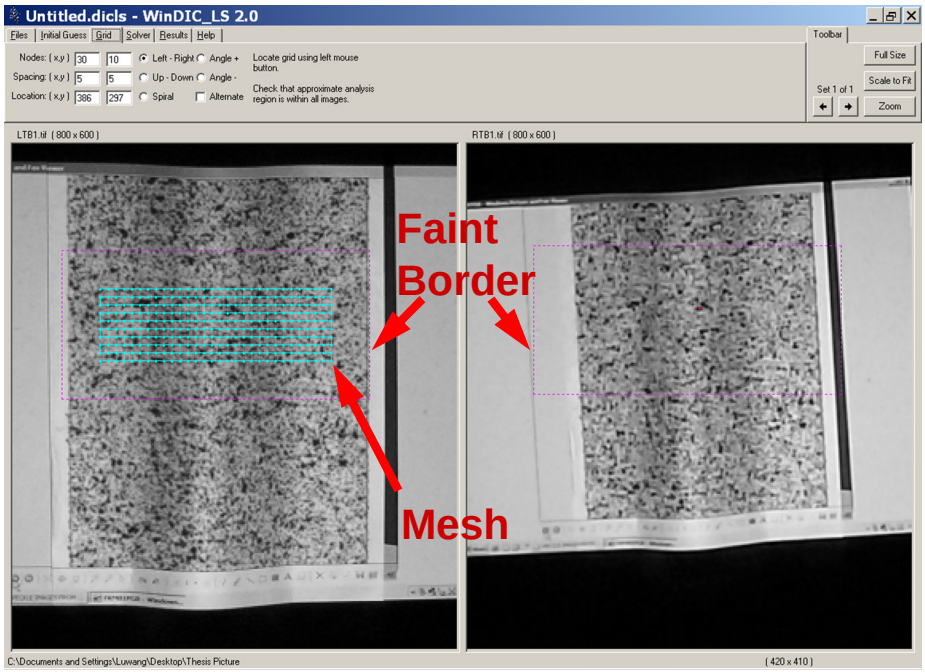

Figure A.15 : The *'Grid'* tab that sets the boundary conditions (i.e. number of nodes, node spacing, boundary of computation) used for mapping the image coordinates. The mesh on the left image indicates the area of interest while both images have a faint border outlined by square dashes to define the computational boundary.

Finally, the number of computational iterations and computational tolerances can be defined in the *'solver'* tab. Once all WinDIC parameters have been entered, the program can begin the solving process by clicking on the *'Start Solver'* button. The progress of the computation and the number of iterations used for convergence in each node can be monitored real-time while the program is running as indicated in Figure A.16.

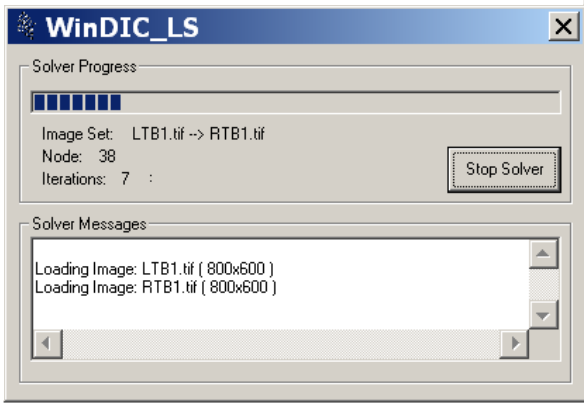

Figure A.16 : Progress window when WinDIC is computing the image coordinates.

After the computation has been completed, the computed mesh will be generated on the right object image for comparison as demonstrated in Figure A.17 with the mesh defined by the user on the left object image. Detailed results can be viewed on-screen on the next tab called *'Results'*; results for individual nodes can also be viewed by clicking on that node. For convenience, the data should be saved for post-analysis.

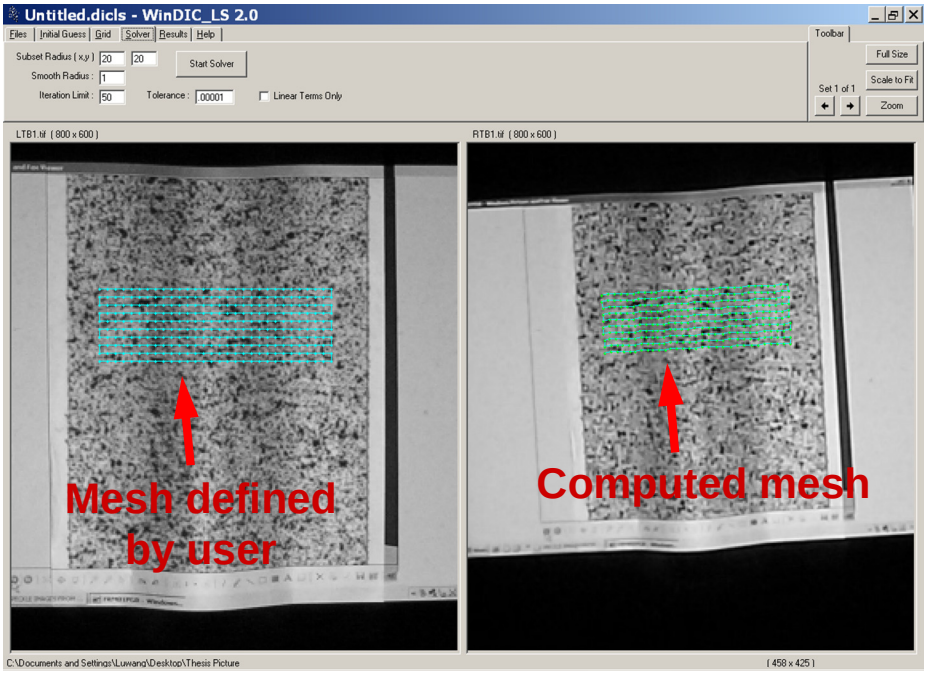

Figure A.17 : Computed mesh after the computational process is indicated on the right object image. The details of the results can be viewed and saved in the next tab called *'Results'*.

A.5 Post Digital Image Correlation Analysis

The output data obtained from DIC cannot be applied to the camera calibration data to produce the surface plot yet, so we will now discuss the post-data processing of DIC and the flowchart of this section is given in Figure A.18. The WinDIC output data consist of many parameters such as pixel coordinates, displacement components, strain values and others; nevertheless the only data of interest in this study is the image coordinates for both left and right camera defined as ***Ref X***, ***Ref Y***, ***Def X*** and ***Def Y*** in the output file.

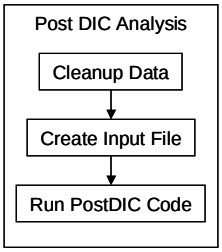

Figure A.18 : Procedure used in the post-DIC data processing.

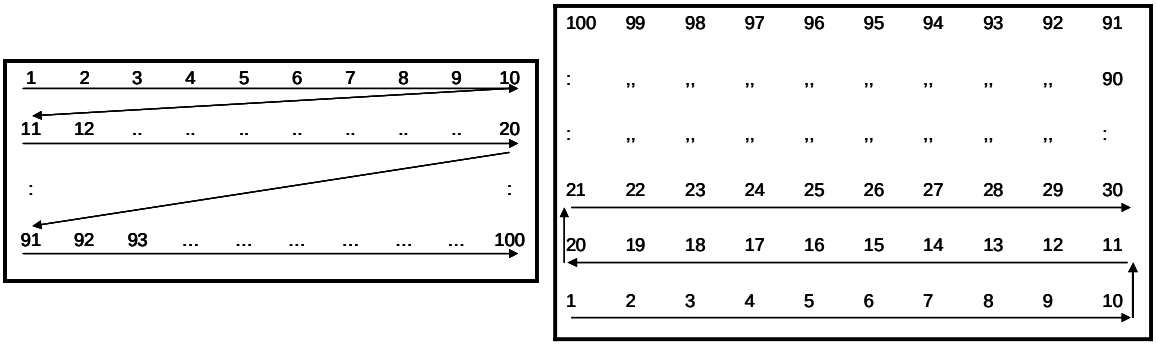

(a) (b)

Figure A.19 : A comparison between (a) sequence of data points stored by Stereo Camera Calibration Toolbox and, (b) the sequence of data points stored in DIC output file. Note that the arrows indicate the pattern of sequence while the numbers represent the *n*-th number of data.

To maintain consistency, let's use Figure A.10 as one of the calibration images used for the entire calibration process. Now, let us assume 100 corner points were extracted from the calibration yielding a 10 × 10 data array. The origin of the reference frame is defined to be on the top left corner of the chessboard pattern as indicated by that figure, thus when the entire calibration process is complete, the sequence of data points stored in the data array will have a format as shown in Figure A.19(a). In contrast, the sequence of data

points stored in the DIC output file is given in Figure A.19(b). For this reason the output data from DIC will need to be rearranged and cleaned, keeping only the data of interest; this can be easily done by importing the data into *Microsoft Excel* to resolve it.

Once Excel has exported the corrected pixel coordinates into a text file; then the script called ***postdic***, written for the purpose of this study, in MatLab will yield an output file that is needed for the final stage of surface profile plot.

A.6 Surface Plotting

Assume that rectified calibration images for both left and right cameras have completed all the calibration procedures. Similarly, the DIC post-data analysis for the object images has also been completed. Thus, all components are established to proceed to the next step, which is plotting the actual surface profile of a baggy web. The summary of the final steps is given in Figure A.20.

After the stereo camera calibration procedure has been completed for the rectified calibration images, the calibration data should be left in the memory and then reload the results from the stereo camera calibration GUI. The output results from the DIC post-data analysis should be loaded into MatLab at this point.

Once completed, run the *stereo triangulation* script by typing the command ***final_phase*** in the command window of MatLab. This script is similar to Dr. Bouguet's example discussed in his website [4]. *Stereo triangulation* function basically finds the location of the points in three-dimensional space, from a set of points given by the left and right image projections which we already

have [4]. The function takes the pixel coordinates of the left and right object image, rotation and translation matrices from the calibration results and the intrinsic parameters from both cameras into the computation as inputs [4]. The output from this script will be the three-dimensional coordinates of the points in the left and right camera reference frames; and it is defined in MatLab as *Xc_1_left* and *Xc_1_right* variable respectively.

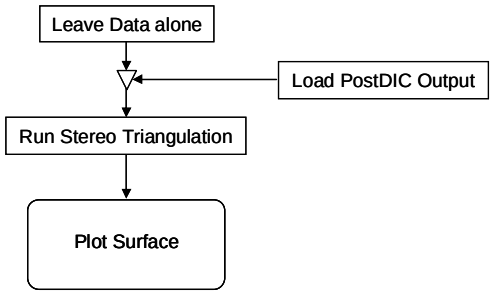

Figure A.20 : The final phase in plotting the actual surface profile of a baggy web.

The final step is to plot the three-dimensional surface profile in MatLab by invoking the command ***plot_surface_left*** or ***plot_surface_right*** depending on the desired perspective either from the left camera or the right camera.

For further details on the camera calibration process and the stereo triangulation computation, please refer to Dr.Bouguet's website [4] whereas for digital image correlation (DIC); it will be in Cary [11,45], Ganesan [24] and Periasamy's thesis [62].

VITA

Jo-Ong Edmond Poh

Candidate for the Degree of

Master of Science

Thesis: CAMBERED AND NON-FLAT POLYETHYLENE WEBS INDUCED BY THICKNESS VARIATION

Major Field: Mechanical Engineering

Biographical:

Personal Data:

Born in Georgetown, Penang, Malaysia on January 21, 1978, the son of Mr. & Mrs. S.L. Poh.

Education:

- Received Bachelor's Degree in Aerospace Engineering from Oklahoma State University, Stillwater, Oklahoma in Dec. 2001.
- Completed the requirements for Master of Science Degree in Mechanical Engineering from Oklahoma State University, Stillwater, Oklahoma in May, 2007.

Experience:

- Teaching Assistant in Department of Mechanical and Aerospace Engineering, Oklahoma State University, Stillwater, Oklahoma, Jan. 2001 – May 2002.
- Graduate Research Assistant in Department of Mechanical and Aerospace Engineering, Oklahoma State University, Stillwater, Oklahoma, May. 2002 – Dec. 2006.

Name: Jo-Ong Edmond Poh Date of Degree: May, 2007

Institution: Oklahoma State University Location: Stillwater, Oklahoma

Title of Study: CAMBERED AND NON-FLAT POLYETHYLENE WEBS INDUCED BY THICKNESS VARIATION

Pages in Study: 174 Candidate for the Degree of Master of Science

Major Field: Mechanical Engineering

Scope and Method of Study: One of the most common web defects is web bagginess. Although it appears in most web materials, it is very difficult to categorize since its appearance changes from one case to the other; hence it has been given different definitions by different people. The most general way to define a baggy web is a web that does not lie flat/straight and has an intrinsic length difference across the width of the web. In this study, polyethylene webs were used as the main material to develop an understanding on some of the web bagginess cases through experimentation. Viscoelastic material properties behavior of polyethylene web was also characterized using time-temperature superposition. Digital image acquisition was used to detect web bagginess. With these results, it is now possible to correctly model this defect using a numerical simulation under development by the Web Handling Research Center.

Findings and Conclusions: Both in-plane and out-of-plane viscoelastic properties have been characterized for 2.5 mil polyethylene web. With this information, it is now possible to evaluate the pseudo-three-dimensional winding code that is currently under development at the Web Handling Research Center; to predict long-term viscoelastic characteristics of wound roll stress, strain distribution for a wide range of winding and storage conditions. This approach of measuring long-term properties of polymers using time-temperature superposition can also be applied to other web materials.

The formation of several web bagginess cases such as cambered web, baggy edges due to slitting process, baggy lane and localized baggy patches have been observed. In each case, analysis of web bagginess has been conducted. These will provide information to evaluate models for the web bagginess. However, it should be noted that there are still other web bagginess cases which have not been investigated yet; and will be addressed in the following section related to future work and recommendations.

Experimental results from non-contact digital surface imaging of baggy lane have confirmed that the proposed image analysis method has the potential to be developed into a method to detect certain types of web bagginess in web handling. Furthermore, this approach can be developed further to couple camera calibration method with two-dimensional digital image correlation to create a three-dimensional digital image correlation method to allow measurements of deformations on curved surfaces.

ADVISER'S APPROVAL: Dr. Hongbing Lu